

DESIGN OF A FIBER-BUNDLE BASED MULTISPECTRAL CONFOCAL
ENDOMICROSCOPE FOR TISSUE VISUALIZATION DURING LUNG BIOPSY
PROCEDURES

by

Zhenye Li

Copyright © Zhenye Li 2022

A Dissertation Submitted to the Faculty of the

WYANT COLLEGE OF OPTICAL SCIENCES

In Partial Fulfillment of the Requirements

For the Degree of

DOCTOR OF PHILOSOPHY

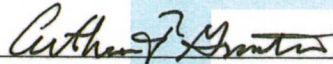
In the Graduate College

THE UNIVERSITY OF ARIZONA

2022

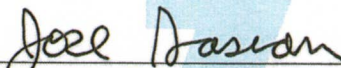
THE UNIVERSITY OF ARIZONA
GRADUATE COLLEGE

As members of the Dissertation Committee, we certify that we have read the dissertation prepared by **Zhenye Li**, titled ***Design of a Fiber-Bundle Based Multispectral Confocal Microendoscope for Tissue Visualization During Lung Biopsy Procedures*** and recommend that it be accepted as fulfilling the dissertation requirement for the Degree of Doctor of Philosophy.



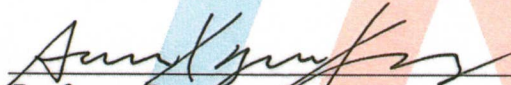
Professor Arthur F. Gmitro

Date: 7/11/2022



Professor José M. Sasián

Date: 07/11/2022

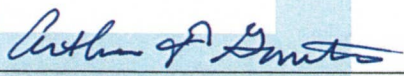


Professor Dongkyun Kang

Date: 7/11/2022

Final approval and acceptance of this dissertation is contingent upon the candidate's submission of the final copies of the dissertation to the Graduate College.

I hereby certify that I have read this dissertation prepared under my direction and recommend that it be accepted as fulfilling the dissertation requirement.



Professor Arthur F. Gmitro
Dissertation Committee Chair
Wyant College of Optical Sciences

Date: 7/12/2022

ARIZONA

ACKNOWLEDGEMENTS

If I had told myself six years ago that I would become a PhD in the future, I would have thought I was joking. At that time, I thought that a PhD was unrealistic for me because I was never a patient student or a good learner. Until the moment I shook hands with Art after the defense, I still felt that everything was so unreal. My defense was just like my school journey, stumbling and full of twists and turns, but I finally finished it. This imperfection tells me that it is all true.

Here, I would like to express my sincere gratitude to all my family, teachers and friends who have helped and supported me.

Thank you, mom and dad, grandparents, for your unreserved love and support. The distance of 10,000 kilometers prevented us from seeing each other easily, and the fifteen-hour time difference even prevented us from talking in time, but it didn't change my missing you in any way. Thanks for everything you did for me.

During years of overseas study, I have been away from my family, but I have met many valuable friends and teachers, each of whom is excellent. They have influenced and changed me and made me know myself better.

Thanks to Yi, I'm so glad I met you. Without your support and encouragement, I am afraid I would not have been able to complete this study. I am really lucky to be in love with you.

Thanks to my mentor, Art, your wisdom and experience always impressed me, and your perspective on issues was often spot-on. Although you occasionally joked that you were getting old, I felt that you were still young and vibrant at heart. Thank you for being there for me and

teaching me. Although you had a heavy schedule as department head, you were always the first to lend a helping hand when I needed it. Thank you for accommodating and guiding me. You are the best.

Thanks DK for your guidance and help. Although I am not your student, I think you are a great mentor. Your perceptiveness and intelligence have made a profound impact on me, and I always benefit from your advice and ideas. Thank you and the group members of the translational optical imaging lab for allowing me to attend your group meetings. The atmosphere in your group is always so relaxed and lovely, and your summer meetings are always so fun and exciting to look forward to. I'm glad to have the opportunity to discuss and share ideas with you and it's been a pleasure to spend time with you.

To Dr. Sasian, thanks for guiding me when I was a master student. I have benefited from your extensive experience and knowledge of geometric optics and the optical design skills you have taught me. One of the reasons I applied for a PhD is because I want to be as good an optical designer as you are.

Thanks to Cheng, my bro and coach for training me and helping me build a healthy body to survive my PhD studies. Thanks to Cheng, Richard and Shuang for helping me when I was in accident. Thanks to Cheng and Richard, for spending that difficult night with me in the hospital when I was sick.

Thank you to all my dear friends for your tolerance and support over the years. Your company has made me experience the warmth of home. Thank you for being there for me when I was in trouble, for sharing with me when you were happy, and for listening to me when I was sad. I am very lucky to have met you and wish you all the best in the future.

Thanks to Huhu and Juju, you are the cutest cats.

These six years of living in Tucson will be one of the most important parts of my life. No matter what the future holds, this experience, these people, will be deeply engraved in my heart.

Dedication

To my Mom and Dad

you are my spiritual support, thanks for everything

Table of Contents

ACKNOWLEDGEMENTS	1
List of Figures.....	8
List of Tables	13
Abstract.....	14
1 Introduction	15
1.1 Lung Cancer	15
1.2 Early Detection of lung cancer.....	15
1.3 Guidance for Lung Needle Biopsy.....	17
1.4 Confocal Microscopy	18
1.5 In-vivo Endomicroscopy with a Fiber Bundle Probe.....	19
1.6 Multispectral Fluorescence Imaging	20
1.7 Overview of Dissertation	21
2 Multispectral Confocal Endomicroscopy in Lung Needle Biopsy Guidance	23
2.1 Introduction	23
2.2 Optical Design and Aberration Correction.....	24
2.2.1 First-order and Image Quality Requirement	24
2.2.2 Design with Custom Optical Elements	26
2.2.3 Design with Off-Shelf Microscope Lenses	28
2.3 Dye Selection and Combination.....	29
2.4 System Components and Setup	30
2.5 Linear Spectral Unmixing with Multiple Dyes	33
2.6 System Interfaces	36
2.7 Tools in Lung Needle Biopsy with MSCE.....	38
2.8 Summary	40
3 MSCE LabVIEW Manual	42
3.1 Program Overview	42
3.2 Program Front Panel.....	42
3.2.1 Display Windows.....	42
3.2.2 Sensor and display parameter controls.....	44
3.2.3 Function Generator Control	47
3.2.4 Color Display Control.....	48

3.3	Program Logic Flow.....	49
3.3.1.	Default Live Mode.....	49
3.3.2.	Spectrum Mode.....	50
3.4	Synchronization of Sensor and Scanning Mirror.....	51
3.4.1.	Ramped Function with Paused Sensor.....	51
3.4.2.	Triangle Signal with Paused Sensor.....	55
3.4.3.	Ramped Function with Free-Run Sensor.....	58
3.5	Image Processing Algorithms.....	61
3.5.1.	From Subframes to Grayscale.....	61
3.5.2.	From Spectrum to Color Display.....	62
3.5.3.	RGB Weight Matrix for RGB Filter-style System.....	64
3.5.4.	RGB Weight Matrix for CIE Mapping Function.....	65
3.5.5.	From Spectrum to Spectral Unmixing Color Display.....	68
3.5.6.	How to Obtain the Spectrum.....	69
3.6	Remaining Problems and Future Improvements.....	70
4	Axial Resolution Test for Fiber-Bundle Based Fluorescence Endomicroscopy	72
4.1	Introduction.....	72
4.2	Theoretical Evaluation of Axial Resolution.....	73
4.3	Axial Resolution Test with Thick Fluorescent Plate.....	73
4.4	Axial Resolution Calculation.....	75
4.5	Experiment Setup and Test on a Benchtop Confocal Microscope.....	76
4.6	Axial Edge Test in the MSCE System.....	77
4.7	Summary.....	80
5	Non-mechanical Beam Steering for Fiber Bundle Depixelization in MSCE	82
5.1	Introduction.....	82
5.2	Previous Work.....	84
5.3	Cross-correlation Method.....	85
5.4	Non-mechanical beam steering method.....	88
5.4.1.	Liquid Crystal Prism.....	90
5.4.2.	Disperse Prism with Known Spectrum.....	91
5.5	Performance.....	92
5.6	Summary.....	93
6	Results from MSCE.....	94
6.1	MSCE test with Paper Tissue.....	95

6.2	Mouse Ex-vivo Lung Tissue Imaging and Dye Combination Testing.....	98
6.2.1.	Fluorescein and Methylene Blue.....	98
6.2.2.	Phloxine B and Mitoxantrone	100
6.2.3.	Fluorescein and Mitoxantrone	103
6.2.4.	Fluorescein and Daunorubicin	104
6.2.5.	Phloxine B and Proflavine	106
6.2.6.	Proflavine and Rose Bengal.....	108
6.3	Rat Open Biopsy Simulation.....	109
6.3.1.	Image from Surface of the Rats' Lung.....	110
6.3.2.	Image from Inside of the Rats' Lung	112
6.3.3.	Videos	114
6.4	Ex-vivo Human Lung Tissue	114
6.4.1.	Necrotic Lung Tissue	116
6.4.2.	Inflammatory Tissue	118
6.4.3.	Cancerous tissue.....	120
6.4.4.	Videos	121
6.5	Summary	122
7	Conclusion and Future Work.....	125
	Appendix A: Zemax Design	129
	Appendix B: System Setup.....	132
	Reference	134

List of Figures

Fig. 1-1. Different depth in a lesion may have different abnormalities..... 17

Fig. 1-2. Imaging with a traditional microscope (upper figure) and a confocal microscope (lower figure)..... 18

Fig. 1-3. Jablonski diagram showing excitation and emission of fluorescent light¹⁰. 20

Fig. 1-4. Candidate DNA/nucleus dye combined with candidate protein/cytoplasm drug-dyes applied to image ovine lung tissue with a standard benchtop confocal microscope²⁶ 21

Fig. 2-1. Cross-section of the design. 0: the proximal end of the fiber bundle; 1: objective (EFL=18mm); 2: lens to image the object to the slit (EFL=76 mm); 3: 15um wide slit; 4: lens with same focal length as lens 2; 5: dispersion element; 6: image lens (EFL=50mm); 7: sensor. 25

Fig. 2-2. RMS spot size vs wavelength and chromatic focal shift (Maximum =167um). 26

Fig. 2-3. Cross-section of the design. 0: the proximal end of the fiber bundle; 1: objective (EFL=18mm); 2: lens to image the object to the slit 3: 15um wide slit; 4: lens with same focal length as lens 2; 5: dispersion element; 6: image lens (EFL=50mm); 7: sensor. *: two flint negative meniscus lenses; the effective focal length in the red box is 90mm. 27

Fig. 2-4. RMS spot size vs wavelength and chromatic focal shift (Maximum =44um). 27

Fig. 2-5. System with off-shelf tube lenses and idealized objective lenses. Another folding mirror is used to make the coordinate system positive, because the black boxes (2 & 4) can be only used in positive coordinate system. 0 the proximal end of the fiber bundle; 1: objective (Olympus 10x Plan Fluor, EFL 18mm, NA 0.3); 2&4: tube lens (Thorlabs TTL-100A, EFL=100mm); 3: 15um wide slit (Thorlabs, S15K); 5: dispersion element (N-BK7, wedged angle 11°); 6: objective (Nikon 4x Plan Fluor, EFL 50mm, NA 0.13); 7: sensor (Basler acA640-750um)..... 28

Fig. 2-6. RMS spot size vs wavelength=750nm and chromatic focal shift.	29
Fig. 2-7. System layout and the method to collect subframe data.	31
Fig. 2-8. Data collection by the MSCE system. As the scan mirror moves the illumination across the fiber, the sensor reads out multiple subframes.....	32
Fig. 2-9. Human ex-vivo tissue and Rat lung tissue with different color mapping function. Imaged with MSCE.....	35
Fig. 2-10. Display windows in LabVIEW front panel. Images were collected from paper marked by fluorescent marker pens. a: this window shows the color image after the program has color mapped the signals of 20 channels; b: a spectral plot, the x-axis is the channel number; the y-axis corresponds to the pixel signal intensity of each channel over the whole image; c: the grayscale image; d: the grayscale image of one channel, changing the number above this window will change the displayed channel.....	37
Fig. 2-11. lung biopsy procedure with MSCE.	39
Fig. 2-12. Real instruments used in this project for implementing the dye delivery, endomicroscopy imaging, and core biopsy tissue collection procedure.....	40
Fig. 3-1. Color image and overall spectral distribution in that image. The color channels from 0 thru 19 cover the wavelength range from 500-750nm.....	42
Fig. 3-2 Image for certain channel.	43
Fig. 3-3 LabVIEW sensor and display control panels.	44
Fig. 3-4. Align button pressed to reset synchronization.	46
Fig. 3-5. Introduction of a Gaussian filter to remove pixelization.....	46
Fig. 3-6. Function generator control.	47
Fig. 3-7. Color display control panel.	48

Fig. 3-8. Logic flow for default live mode.....	49
Fig. 3-9. Logic flow for spectrum mode.....	50
Fig. 3-10. Diagram showing the signal from the function generator and sensor trigger.....	52
Fig. 3-11. Scanning process at distal tip of fiber bundle probe.....	54
Fig. 3-12. Diagram showing the signals for the function generator and sensor triggers.....	56
Fig. 3-13. Scanning process of the fiber bundle probe.....	57
Fig. 3-14. Diagram showing the signals for the function generator and sensor triggers.....	59
Fig. 3-15. Scanning process of the line illumination at the fiber bundle probe.....	60
Fig. 3-16. Process to get a grayscale image.....	62
Fig. 3-17. Process to convert spectral information to RGB information by using an RGB weight matrix.....	63
Fig. 3-18. Diagram of typical RGB filter-style display.....	64
Fig. 3-19. The CIE 1931 RGB color matching functions ⁴⁵	66
Fig. 3-20. The CIE XYZ color mapping functions ⁴⁵	67
Fig. 3-21. Process to convert spectrum information to RGB information by using the spectral unmixing algorithm.....	69
Fig. 3-22. Process to collection of spectral distribution.....	70
Fig 4-1 Point spread function plots for a line-scanning confocal microscope.....	73
Fig. 4-2. Moving the thick fluorescent slide along axis.....	74
Fig. 4-3. System setup for axial edge test.....	76
Fig. 4-4. Diagram of Nikon benchtop confocal microscope's edge response function and its axial point spread function. left: edge response function; right: PSF from axial edge test and microsphere test.....	77

Fig. 4-5. Setup for the axial resolution measurement in the MSCE system.	78
Fig. 4-6. The grayscale images collected by MSCE during this test. Red box: regions of interest that are used to calculate the axial resolution.	79
Fig. 4-7. The MSCE edge response function (left) and axial resolution (right).	80
Fig. 5-1. Image of a USAF bar target with pixelization problem.	83
Fig. 5-2. Geometry of a hexagonally packed array of optical fibers ⁴⁶	83
Fig. 5-3. Images collected before and after probe's movement.	87
Fig. 5-4. Using average method and MIP method to remove pixelization problem.	88
Fig. 5-5. Use of a scanning mirror to steer beam offset.	89
Fig. 5-6. Non-mechanical beam steering with two LC prisms.	90
Fig. 5-7. Non-mechanical beam steering with prism.	91
Fig. 5-8. The original image of a bar target acquired by through the fiber bundle (left image) and the image after depixelization (right image).	92
Fig. 6-1. MSCE images obtained from stained paper samples.	96
Fig. 6-2. Image obtained from a business card.	97
Fig. 6-3. Images collected from the mouse tissue stained by fluorescein and methylene blue. ...	99
Fig. 6-4. Images collected from the mouse tissue stained by phloxine B and mitoxantrone.	101
Fig. 6-5. Solution of mitoxantrone and phloxine B were found to precipitate.	102
Fig. 6-6. Images collected from the mouse tissue stained by fluorescein and mitoxantrone.	103
Fig. 6-7. An image collected from the mouse tissue stained by acridine orange and mitoxantrone (without gaussian blur).	104
Fig. 6-8. Images collected from the mouse tissue stained by fluorescein and Daunorubicin.	105
Fig. 6-9. Images collected from the mouse lung tissue stained by proflavine and phloxine B. .	107

Fig. 6-10. Images collected from the mouse tissue stained by proflavine and rose bengal.....	108
Fig. 6-11. Rat lung biopsy simulation.....	110
Fig. 6-12. Images of rat lung surface from biopsy simulation. Dye combination: proflavine and rose bengal.	111
Fig. 6-13. Images inside rat’s lung from biopsy simulation. Dye: proflavine and rose bengal..	113
Fig. 6-14. Still frames from videos. a: from the surface of the rat lung, and b: from the interior as the probe enters the lung	114
Fig. 6-15. Ex-vivo human necrotic tissue from lung needle biopsy.	117
Fig. 6-16. Ex-vivo human inflammatory tissue from lung needle biopsy.	119
Fig. 6-17. Ex-vivo human cancerous tissue from lung needle biopsy.....	120
Fig. 6-18. Still frame images from a video of a: cancerous ex-vivo human lung tissue; b: inflammatory ex-vivo human lung tissue. Dye applied: proflavine (DNA-binding, green) and rose bengal (connective tissue binding, red).....	121

List of Tables

Table 1. Dye combinations. 29

Table 2 Inner diameters of the introducer needle⁴⁰⁻⁴³**Error! Bookmark not defined.**

Table 3 Outer diameters of the biopsy needle⁴⁰⁻⁴³**Error! Bookmark not defined.**

Abstract

There is a critical need for a technology that can assist doctors in more accurately evaluating lung nodules at the time of biopsy. To address this need, a multispectral fluorescence line-scan confocal endomicroscope was developed that employs a fiber bundle probe to image tissue at the distal tip of the biopsy introducer needle.

For all fiber bundle probe-based fluorescence systems, the axial resolution is challenging to measure, mainly due to the nature of the direct contact of the fiber bundle with the object and the different wavelengths of fluorescence emission and excitation. Therefore, in this dissertation, we find a method to accurately measure this system's axial resolution.

The problem of pixelization of the fiber bundle causes a drop in the sampling frequency of the system. In this dissertation, we provide several different potential solutions to this problem.

The multispectral nature of the instrument allows the simultaneous use of multiple FDA-approved dyes that stain different cellular/tissue compartments in different spectral regions to distinguish between lung cancer and benign conditions of the lung. The imaging system has been used to image normal mouse and rat lung tissue as well as *ex vivo* human core biopsy lung tissue.

1 Introduction

1.1 Lung Cancer

Lung cancer is a type of cancer that starts in the lung, near the lung surface. About 2.1 million new cases and 1.8 million deaths per year makes lung cancer one of the most common cancers in the world¹, including more than 200,000 cases that occur in the US every year². Lung cancer is one of the most dangerous and common cancers for both men and women, about 25 percent of all cancer death are caused by lung cancer 2018³. It has a very high mortality rate compared to other leading cancer sites. The five-year survival rate for lung cancer is 19 percent^{1,3,4}, which is much lower than colorectal, breast, and prostate cancer.

The early diagnosis of lung cancer can significantly improve the five-year survival rate to 56 percent. Unfortunately, 84 percent of lung cancer cases are not detected at an early stage. The five-year survival rate drops to only 5 percent once lung cancer cells spread to other organs. The low early diagnosis ratio and high mortality for distant tumor cases result in more than 50 percent of patients dying within one year when lung cancer is diagnosed⁵.

1.2 Early Detection of lung cancer

The survival rate of lung cancer can be increased dramatically if the cancer is detected at an early stage. Low-dose CT screening⁵, an early screening tool to identify suspicious lung nodules, has been used to decrease lung cancer mortality. Among high-risk populations, such as smokers, the mortality rate can be reduced by at least 14 percent. Many lung cancer-related death cases can be prevented with proper early detection⁵ and effective therapy.

While low-dose CT screening can be utilized to identify suspicious lung nodules, the diagnostic performance in distinguishing between lung cancer and benign cases of lung disease is limited because it does not provide cellular-level imaging. Lung nodules that appear on CT scanning or other imaging tests can vary depending on pathologic conditions, such as primary inflammatory responses to viral, bacterial, or fungal infections, autoimmune diseases including sarcoidosis, scarring, primary lung cancer, and metastatic spread to the lung from other types of cancer.

A lung biopsy^{12-17,20-25} is often necessary for identifying these abnormal conditions. Lung biopsy is a method to extract one or more samples from a targeted nodule for further examination. Most of the time, the examination is for confirming cancer. Depending on the location of the lesions, general health, or other lung problems, different types of lung biopsies are done.

When lesions are located near an accessible bronchial structure, a transbronchial biopsy^{15-17,21,24,25} can be performed. A bronchoscope is placed through the trachea down into the airway of the lung. The samples can be extracted by forceps. When a lesion appears in the peripheral lung, a transthoracic procedure^{12-14,22,23} is employed. A needle is placed through the chest between ribs into the lung to extract a sample. Most times, a CT scan or other tomography imaging technique is utilized to guide the biopsy needle into the targeted nodule. This type of biopsy is also called needle biopsy.

Lung biopsy comes with potential risks. Lung needle biopsy may cause pneumothorax, which occurs when air and fluid leak into the space between the lung and the chest wall. Pneumothorax can cause shortness of breath. Infection and extensive bleeding are also potential risks caused by lung needle biopsy. But to get enough tissue with small gauge biopsy needles, several extractions

are needed, and the probability of potential risks rises with the increasing number of extractions. So, it is very important to select proper tissue and avoid missing it. CT-scan, which does not provide cellular imaging, sometimes is not enough to guide biopsy needles.

1.3 Guidance for Lung Needle Biopsy

Fig. 1-1 illustrates that while the biopsy needle is correctly guided by CT scan and placed in the nodule, the tissue structure from a single biopsy core may have a different abnormalities at different locations within the nodule.

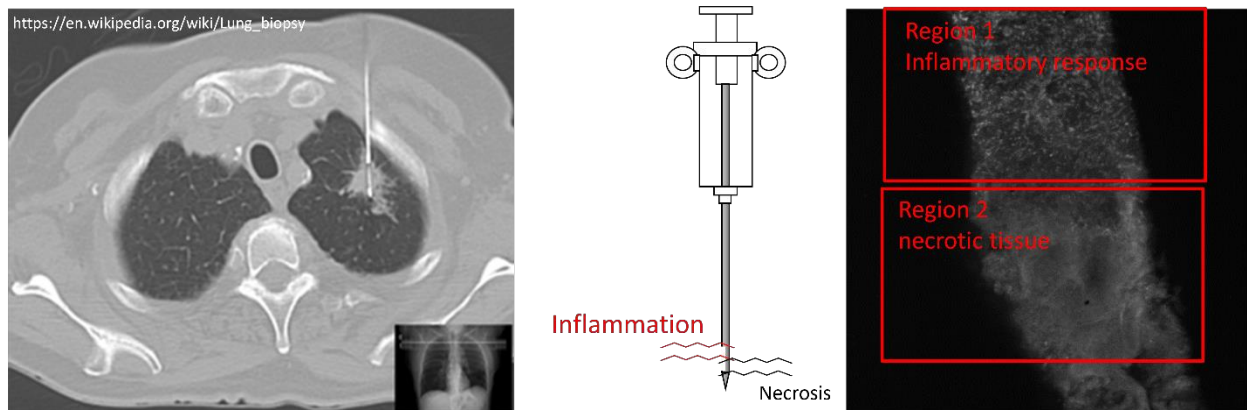


Fig. 1-1. Different depth in a lesion may have different abnormalities. The first image is from Wikipedia.

Region 1 in the tissue has an inflammatory response but region 2 shows that this part of the tissue is necrotic. The reason is that different locations of the same nodule may have a different lesion structure. Similarly, cancer cells may be surrounded by or surround healthy cells or other non-cancer tissues. An incorrect diagnosis may occur if the cancer cells are not found and taken out. So, a cellular level imaging device is helpful to guide the core biopsy procedure, especially when it provides images at different depths along the needle insertion direction, which helps select proper tissue to take out and reduces the number of biopsies taken to decrease the risk of the lung needle biopsy.

1.4 Confocal Microscopy

For most thick biological samples, signals from out of focus planes dramatically reduce the contrast of the image. An optical sectioning ability is necessary to image thin sections without overlapping out of focus planes. The confocal microscope^{7,8} is one type of optical system that has sectioning ability. Different from the conventional microscope, which forms an image directly at the sensor, a confocal microscope illuminates a point (or a line) in the object and then images the emitted light to an intermediate image plane where a pinhole (or a slit) is located (see Fig. 1-2). This pinhole (or slit) significantly removes light from out-of-focus objects. By scanning the illumination point (or line) across the object, a high-resolution in-focus image of a very thin section of tissue can be obtained with reduced contribution from the out-of-focus planes. As a result, confocal microscopy has been widely used for imaging thick biological samples.

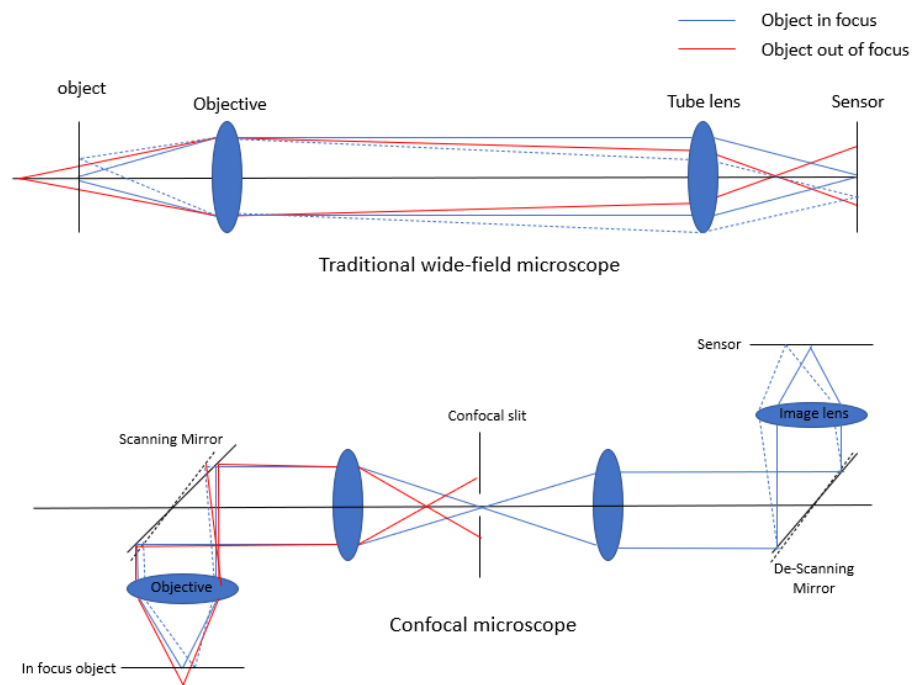


Fig. 1-2. Imaging with a traditional microscope (upper figure) and a confocal microscope (lower figure).

1.5 In-vivo Endomicroscopy with a Fiber Bundle Probe

Benchtop confocal microscopes, which have optical sectioning ability, are used to provide high-resolution images of biological samples. While it is widely applied to in-vivo imaging such as skin, cornea, or teeth, it is not easy to image deeper within the body.

In 1993, Arthur Gmitro and David Aziz first described the concept of using a fiber-optic imaging bundle to relay the image at the distal tip of the fiber bundle to the proximal surface of the fiber bundle coupled with a confocal microscope to image tissue in situ inside the human body³¹. The combination of fiber bundle probe and confocal microscopy allows real-time in-vivo imaging with optical sectioning ability and can be utilized in minimally invasive surgery. This approach provides a clear image of the tissue at the distal tip of the fiber bundle probe and reduces sample misses and potentially increases the accuracy of early detection.

Andrew Rouse and Arthur Gmitro developed the multispectral confocal endomicroscope that provides 26 spectral channels instead of just one spectral channel^{33,34}. A customized spectrometer is introduced to disperse fluorescent signals from the tissue to different rows of a 512X512 CCD sensor, then 256 frames of data are collected after 4.1s to reconstruct a 2-D image with 26 different spectral channels. In this multispectral mode, the cellular structure of the tissue can be collected during optical biopsy processes and diagnostic information can be obtained with the provided spectral information.

In recent years, there has also been work published using endomicroscopes and bronchoscopes to help detect lung disease. In 2017, Zhuquan and his team used needle-based confocal laser endomicroscopy to help physicians diagnose peripheral lung disease²⁰. With CT guidance, their system could reach the target area clearly and successfully observe alveoli and other structures. In 2019, Mathieu and their team used probe-based bronchoscopy²² to observe

fluorescent bronchiolar cells, alveolar cells, and alveolar tissue. This work shows bronchoscopy can be used to observe lung structures. In 2021, Tess used bronchoscopic needle-based confocal laser endomicroscopy to observe and ultimately diagnose peripheral lung cancer in real-time^{23,24}. They compared their results with conventional histology results and show this technique is capable for providing cellular level imaging of malignant cells.

1.6 Multispectral Fluorescence Imaging

Fluorescence imaging⁹ is a very popular method in confocal microscopy. The contrast agent (fluorophore) first absorbs the light within a certain wavelength band (excitation), and then emits fluorescence light with a longer wavelength band, as

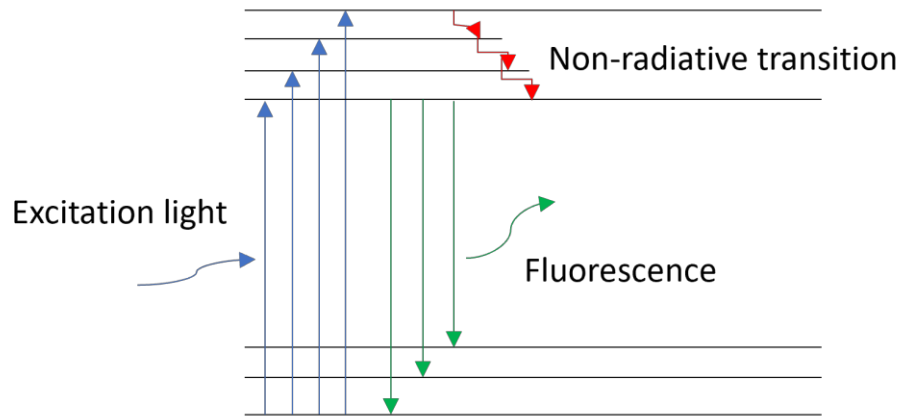


Fig. 1-3¹⁰ shows.

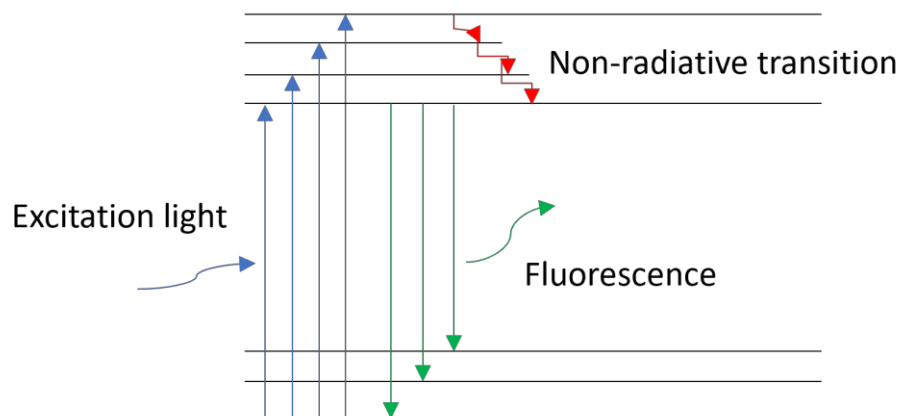


Fig. 1-3. Jablonski diagram showing excitation and emission of fluorescent light¹⁰.

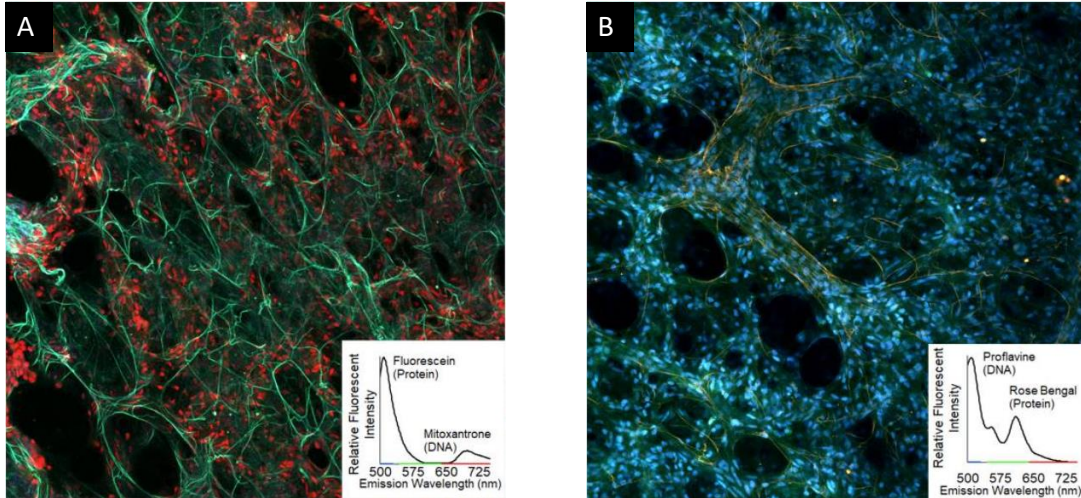


Fig. 1-4. Candidate DNA/nucleus dye combined with candidate protein/cytoplasm drug-dyes applied to image ovine lung tissue with a standard benchtop confocal microscope²⁶.

One of the benefits of fluorescent imaging is that different contrast agents with different fluorescence spectral properties can be used to label different biological features of the tissue. So, if a system has an ability to distinguish different wavelengths, it can be used to distinguish different structures marked by these agents as well. Fig. 1-4 shows two example images captured by a three spectral channel point-scan confocal microscope using two fluorescent stains as indicated in the spectrum box of each image. This is called multi-spectral ability.

1.7 Overview of Dissertation

In this dissertation, we designed a new multispectral confocal endomicroscope (MSCE) system to help physicians observe suspicious nodules and select appropriate biopsy samples in the clinical setting of core biopsy of the human lung.

Chapter 2 elaborates on the principles of this optical system, including its optical design and the choice of optical components. In addition, the chapter will mention how we introduce the dye into the target area and how we use image processing to differentiate between two spectrally similar dyes.

Chapter 3 describes in detail the LabVIEW software that controls the system. The beginning of this chapter describes how to use this software to control the parameters of the MSCE system. Then the chapter describes the logic of the system in its different modes of operation. Finally, this chapter describes the image processing method of the system.

Chapter 4 describes how to measure the axial resolution of the fiber bundle probe-based fluorescence imaging system. At the beginning of the chapter, I describe the principle of this method. Afterward, we apply this method to a Nikon benchtop confocal microscope and compare its results with the conventional method. Finally, we applied this method to the MSCE system and measured its axial resolution.

Chapter 5 describes several approaches to solve the pixelization problem faced by fiber-bundle imaging systems. These include the mechanical motion method, the method using optoelectronic elements and the dispersion method. We have built a prototype of one of these methods, but unfortunately, we have not been able to reduce this prototype to a size that can be applied to biopsies. The chapter will conclude by describing the advantages and disadvantages between several methods and what future improvements are possible.

Chapter 6 will show some of the different results we obtained from imaging mouse, rat, and human lung tissue samples. We have analyzed human samples with different. We analyzed the similarities and differences of human samples with different pathologies under MSCE system and traditional H&E methods.

2 Multispectral Confocal Endomicroscopy in Lung Needle Biopsy Guidance

2.1 Introduction

An approach to image tissue at the distal end of the biopsy needle, before tissue extraction, could improve tissue sampling accuracy. Further, the ability to observe lung tissue in its natural environment before tissue extraction might even obviate the need for tissue extraction altogether and avoid some of the risks associated with transthoracic core needle biopsy (CNB), such as bleeding and pneumothorax.

As one of the thin and flexible waveguides, a coherent fiber bundle is one of the best options to relay the image from the distal end to the proximal end that coupled with microscopes or endoscopes, with high resolution cellular-level imaging. Fiber and fiber bundle imaging has been utilized in several optical systems, such as fluorescent confocal microscopy and epifluorescence microscopy⁷. In the past, various fiber bundle confocal endomicroscopy configurations have been built^{21,22-25}. The advantage of this approach is that it allows placing the mechanical scanner and illumination source outside the patient's body.

A multi-spectral confocal endomicroscope (MSCE) was developed to meet this clinical need^{7,13,14}. The basic system is similar to previous work developing a line-scan confocal endomicroscope but incorporates a dispersive element to enable the collection of multi-spectral data³³. The fundamental capability of the newly developed MSCE instrument is to obtain real-time multi-spectral optically sectioned images of the tissue at the distal tip of a small biopsy needle before the tissue is extracted. This imaging ability could substantially reduce the number

of near misses or errors in tissue collection that occur with standard CT guidance alone. The MSCE instrument collects multi-spectral images, which enables the simultaneous imaging of multiple fluorescent dyes at one time. By utilizing combinations of fluorescent dyes with properly chosen color mapping from spectral data to RGB display, the MSCE can identify various tissue components critical to making a useful diagnosis.

In previous work²⁶, several combinations of FDA-approved fluorescent dye were used to image ex-vivo ovine lung tissue. Two types of dyes were combined: (i) one DNA-binding dye with (ii) one protein-binding dye. Typical DNA-binding dyes, such as proflavine, label cell nuclei and help identify cancer proliferation and metastasis. Typical protein binding dyes, such as rose bengal, label proteinaceous connective tissue and help to identify normal alveolar structure from the abnormal lung.

2.2 Optical Design and Aberration Correction

This section mainly focuses on the design of the optical lens system to allow for adequate aberration correction. A detailed analysis of some device and sensor parameters will be given in section 2.4

2.2.1. First-order and Image Quality Requirement

The optical imaging performance of this system is mainly limited by the fiber bundle. In this system, a fiber bundle (FIGH-30-800G, 0.3 NA) with fiber core diameter of 3 microns, a core-to-core spacing of 4.1 microns, and a field of view (FOV) of 750 microns is utilized. An optical system is required to have a spatial resolution equal to or better than the fiber bundle and a sensor FOV equal to or slightly larger than the fiber bundle in order to have adequate performance. Moreover, the system should have good imaging performance for the wavelength band from 500nm to 750nm without any compensation or adjustments required.

For this imaging system, a sensor with a 4.8-micron pixel size was selected. The magnification between the image and object is 2.78x (10x Olympus objective (EFL 18mm, NA 0.3) on the object side and 4x Nikon objective (EFL 50mm, NA 0.13) on the image side) so that the Nyquist sampling period of the camera (4.8 microns) is less than the core diameter of the fiber bundle ($2.78 \times 3 = 8.34$ microns). And because the core diameter is smaller than the core-to-core distance, this camera has a higher sampling frequency than the fiber bundle. A 15-micron wide slit is selected to closely match the magnification from fiber to slit.

Because the system images the full spectrum simultaneously, it has a high requirement for the correction of longitudinal chromatic aberration. Fig. 2-1 shows a multispectral confocal system that consists of doublets. The symmetric structure of element 2 and 4 corrects for odd aberrations including coma, distortion, and lateral chromatic aberration. However, it doubles even aberrations, such as spherical aberration and longitudinal chromatic aberration.

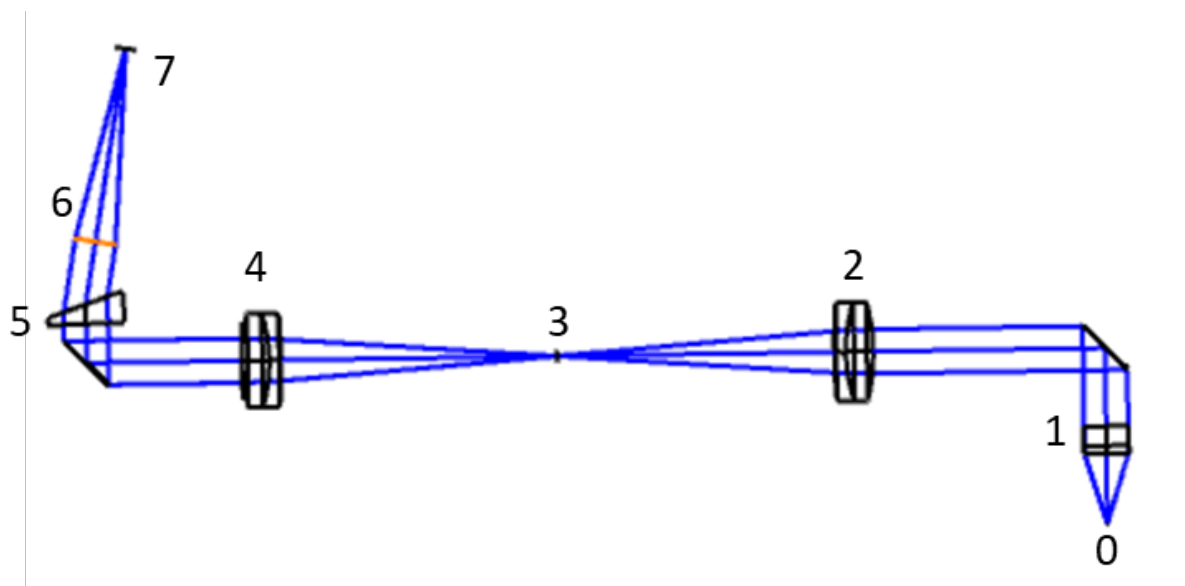


Fig. 2-1. Cross-section of the design. 0: the proximal end of the fiber bundle; 1: objective (EFL=18mm); 2: lens to image the object to the slit (EFL=76 mm); 3: 15um wide slit; 4: lens with same focal length as lens 2; 5: dispersion element; 6: image lens (EFL=50mm); 7: sensor.

Fig. 2-2 indicates the RMS spot size vs wavelength for this system, because of the chromatic aberration, only part of the spectrum can have performance better than the diffraction limit. The focal shift over all wavelengths in the spectral range is 167-microns, while the diffraction limit is 52-microns, which indicates we need more than 0.1mm compensation of defocus to make the wavelength range be in-focus. As a result, we need to have a system with better chromatic aberration correction.

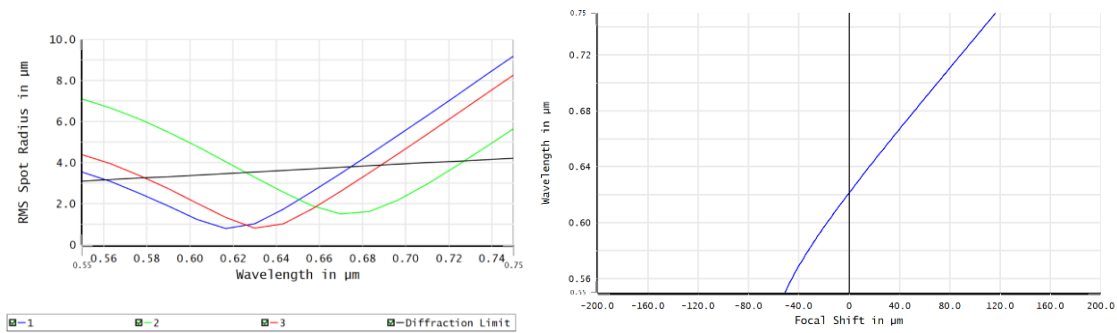


Fig. 2-2. RMS spot size vs wavelength and chromatic focal shift (Maximum =167μm).

2.2.2. Design with Custom Optical Elements

The first solution is to introduce customized lenses to correct even aberrations. To keep the benefit of symmetry, two identical customized lenses are required on both sides of the slit.

Fig. 2-3 shows the design with customized lenses: the meniscus lenses have negative power so that the field curvature can be well-corrected. Furthermore, a flint glass is selected as the material to further balance the longitudinal chromatic aberration. Astigmatism can be corrected by shifting these meniscus lenses.

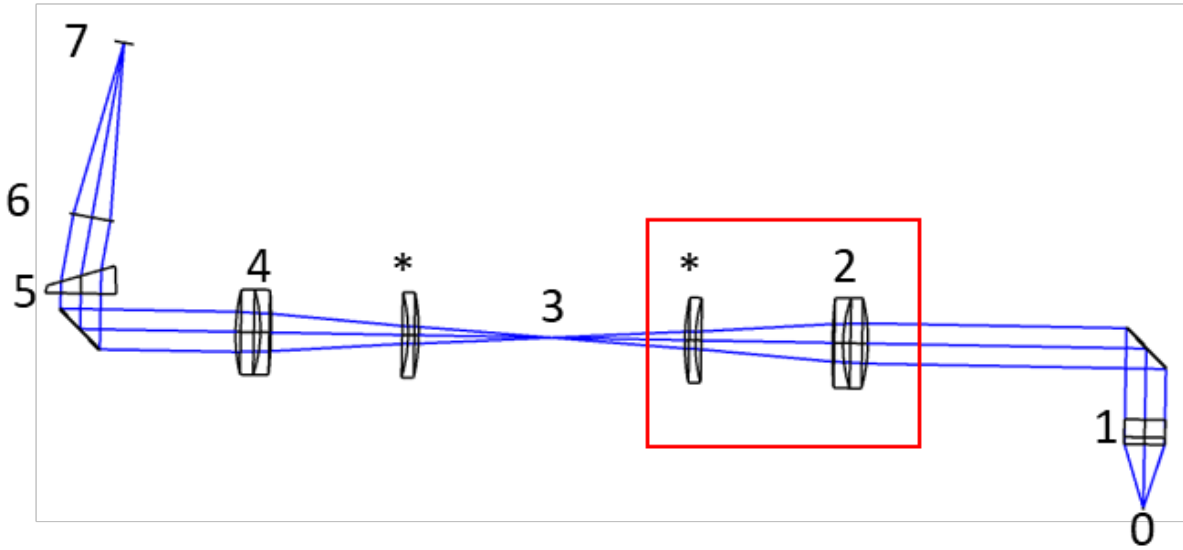


Fig. 2-3. Cross-section of the design. 0: the proximal end of the fiber bundle; 1: objective (EFL=18mm); 2: lens to image the object to the slit 3: 15um wide slit; 4: lens with same focal length as lens 2; 5: dispersion element; 6: image lens (EFL=50mm); 7: sensor. *: two flint negative meniscus lenses; the effective focal length in the red box is 90mm.

The material selected for the new lenses is S-NPH1, which has a relative cost (to BK7 glass) =4.2. This design has a better performance as shown in Fig 8.

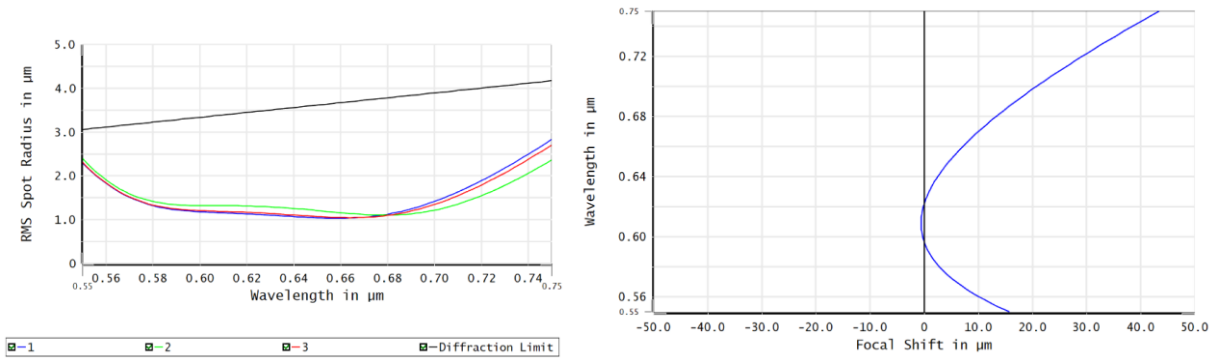


Fig. 2-4. RMS spot size vs wavelength and chromatic focal shift (Maximum =44um).

Fig. 2-4 illustrates a much smaller RMS spot size that is better than the diffraction limit across the field for all wavelengths. The chromatic focal shift is 44-micron which is smaller than the diffraction limit (52-micron). This system is further corrected for longitudinal chromatic

aberration, astigmatism, and field curvature. However, spherical aberration is overbalanced, thus defocus is introduced to improve the image quality.

2.2.3. Design with Off-Shelf Microscope Lenses

Another solution is to use off-the-shelf well-corrected microscope objectives and tube lenses.

Fig. 2-5 shows the design.

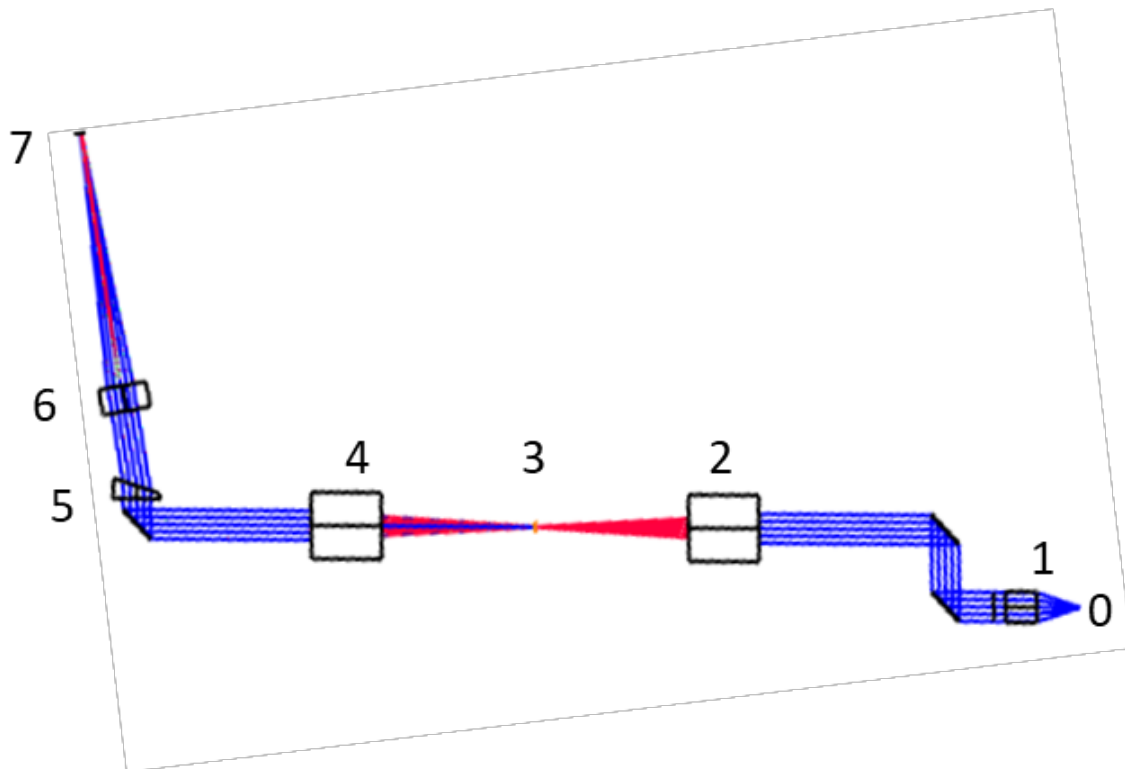


Fig. 2-5. System with off-shelf tube lenses and idealized objective lenses. Another folding mirror is used to make the coordinate system positive, because the black boxes (2 & 4) can be only used in positive coordinate system. 0 the proximal end of the fiber bundle; 1: objective (Olympus 10x Plan Fluor, EFL 18mm, NA 0.3); 2&4: tube lens (Thorlabs TTL-100A, EFL=100mm); 3: 15um wide slit (Thorlabs, S15K); 5: dispersion element (N-BK7, wedged angle 11°); 6: objective (Nikon 4x Plan Fluor, EFL 50mm, NA 0.13); 7: sensor (Basler acA640-750um).

Fig. 2-6 indicates the maximum chromatic focal shift is 74-microns, which is larger but close to the 52-micron diffraction limit. The RMS spot size is diffraction limited in this design. Because of the ease of using off the shelf optical components, the optical system shown in Fig. 2-5 was selected for the MSCE system.

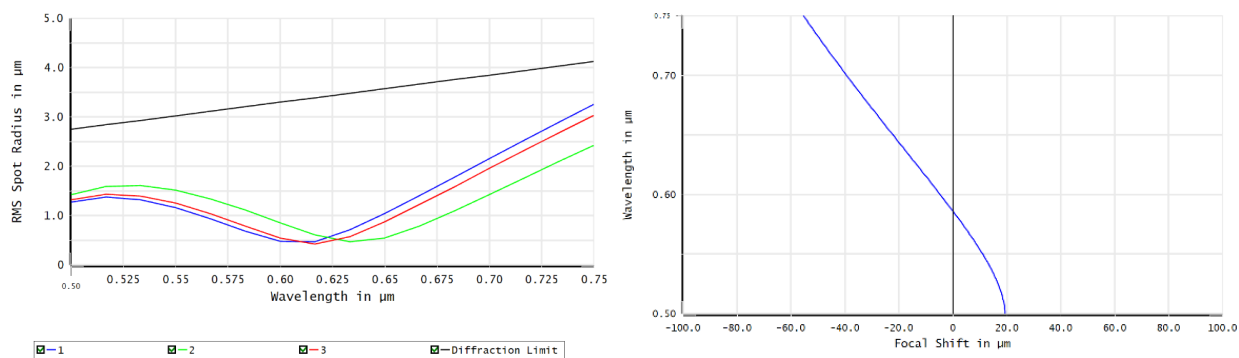


Fig. 2-6. RMS spot size vs wavelength=750nm and chromatic focal shift.

2.3 Dye Selection and Combination

To obtain distinguishable color differences between cell nuclei and proteinaceous connective tissue, we use DNA binding dyes, and protein binding dyes that have different fluorescence emission spectrums. Table 1 illustrates the dye combinations investigated in this work:

Table 1. Dye combinations.

Connective Tissue Dye	Nucleus Dye	Laser(s) Used	Dye Concentrations (1 & 2)
Fluorescein	Mitoxantrone	488 nm / 640 nm	5 μM / 200 μM
Fluorescein	Methylene Blue	488 nm / 640 nm	5 μM / 200 μM
Fluorescein	Daunorubicin	488 nm	5 μM / 200 μM
Phenol Red	Methylene Blue	488 nm / 640 nm	200 μM / 200 μM
Phloxine B	Daunorubicin	488 nm	200 μM / 200 μM
Rose Bengal	Proflavine	488 nm	200 μM / 200 μM

Some combinations need both excitation wavelengths to control the signal level from different fluorescent dyes. The results of different dye combinations used to image mouse lung samples are included in chapter 6.

2.4 System Components and Setup

The layout of the multi-spectral line-scanning confocal microscope is illustrated in Fig. 2-7. The photographs of real MSCE system is attached in Appendix B. Fluorescence excitation light is provided by one or more wavelengths from an iFLEX Viper three-laser system operating at wavelengths of 488nm, 640nm and 780nm. All three lasers, with operator control of laser power, are coupled into a single-mode fiber. The excitation beam exiting the single-mode fiber is collimated by a lens and passes through a cylindrical lens that, together with the objective lens (Olympus 10x Plan Fluor, EFL 18mm, NA 0.3), focuses the light to a line illumination on the proximal face of the fiber bundle probe. The dichroic mirror reflects the excitation light towards the scan mirror, which scans the line illumination across the proximal face of the fiber-bundle probe.

The line illumination beam is relayed from the proximal face to the distal face of the fiber-bundle probe, which is in contact with the tissue. The excitation beam passing through the fiber excites the fluorescent dye that is staining the tissue. The fiber bundle used in this system is a Fujikura imaging fiber bundle (FIGH-30-800G), which has approximately 30,000 fiber cores. The fiber diameter without its protective coating (0.950mm with protective coating present) is about 800 μ m (750 μ m diameter active image area). The fiber bundle with the protective coating can fit through the lumen of a 19-gauge introducer needle that is typically used with a 20-gauge core biopsy needle for tissue extraction (see Appendix C). The core size of the individual fibers in the bundle is approximately 3 microns with an NA of 0.3. The core-to-core distance is 4.1 μ m.

The fluorescence emission from the tissue is relayed back to the proximal end of the fiber-bundle probe, de-scanned by the scan mirror, transmitted through the dichroic mirror, and focused by a tube lens (Thorlabs TTL-100A EFL 100mm) onto the confocal slit aperture. This

creates a confocal system with optical sectioning at the distal tip of the fiber-bundle probe. The magnification from fiber bundle to slit is given by

$$M = \frac{f_{tube}}{f_{objective}}. \quad (2.4.1)$$

In this system, $f_{tube} = 100 \text{ mm}$, $f_{objective} = 18 \text{ mm}$, thus the magnification is $100/18 = 5.6$. The slit width of $15 \mu\text{m}$ is roughly equal to the magnified size of a single fiber core ($3 \mu\text{m} \times 5.6 = 16.8 \mu\text{m}$).

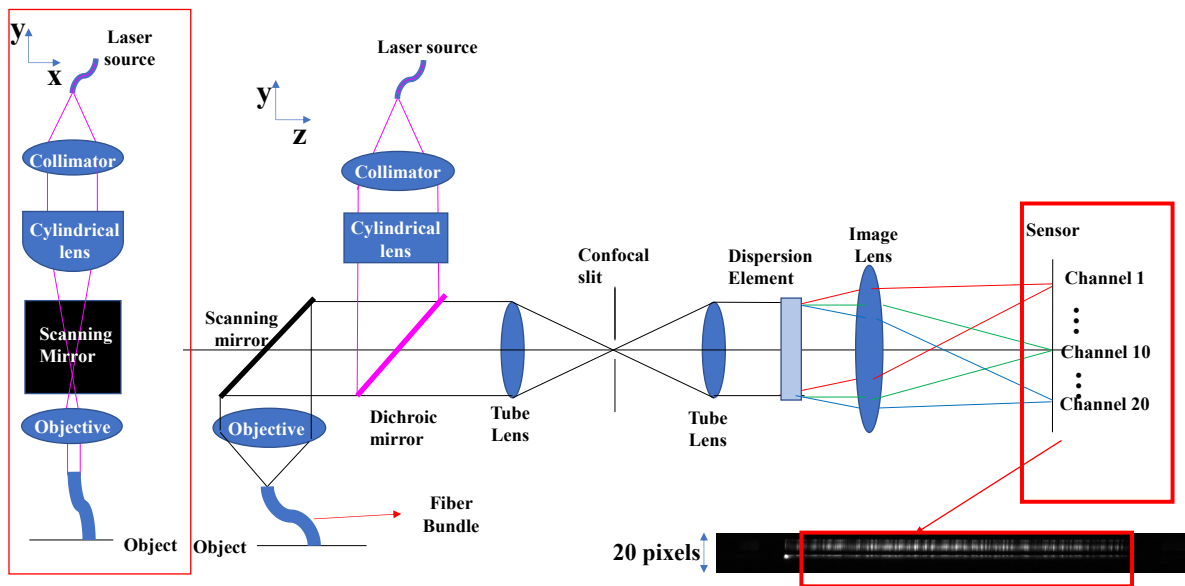


Fig. 2-7. System layout and the method to collect subframe data.

Most out-of-focus light is filtered by the slit. The signal is then collimated by the same type of tube lens. A prism (N-BK7, wedged angle 11°) is inserted in the collimated space before the imaging lens. The Nikon image lens (Nikon 4x Plan Fluor, EFL 50mm, NA 0.13) focuses the fluorescence light onto the sensor. The magnification from slit to sensor is $50/100 = 0.5$. The signal is dispersed over 20 channels and focused on different rows at the sensor (Basler acA640-750um). The image obtained for a single angle of the scan mirror is called subframe.

The spatial resolution of this imaging system is fundamentally limited by the fiber bundle sampling, which depends on the core-to-core distance of fibers in the fiber bundle. The maximum spatial frequency that can be imaged without aliasing has a period of twice the core-to-core distance or $8.2 \mu\text{m}$, giving a maximum spatial frequency of 122 cycles/mm (min $\Delta x = 9.98 \mu\text{m}$). The overall magnification from fiber to sensor is $5.6 \times 0.5 = 2.8$. Therefore, the core-to-core distance measured at the image sensor is $11.5 \mu\text{m}$, and the maximum spatial frequency without aliasing at that location is 43 cycles/mm. The sensor itself has a pixel size of $4.8 \mu\text{m}$, so its maximum unaliased spatial frequency is 104 cycles/mm, well above the maximum spatial frequency of the fiber bundle.

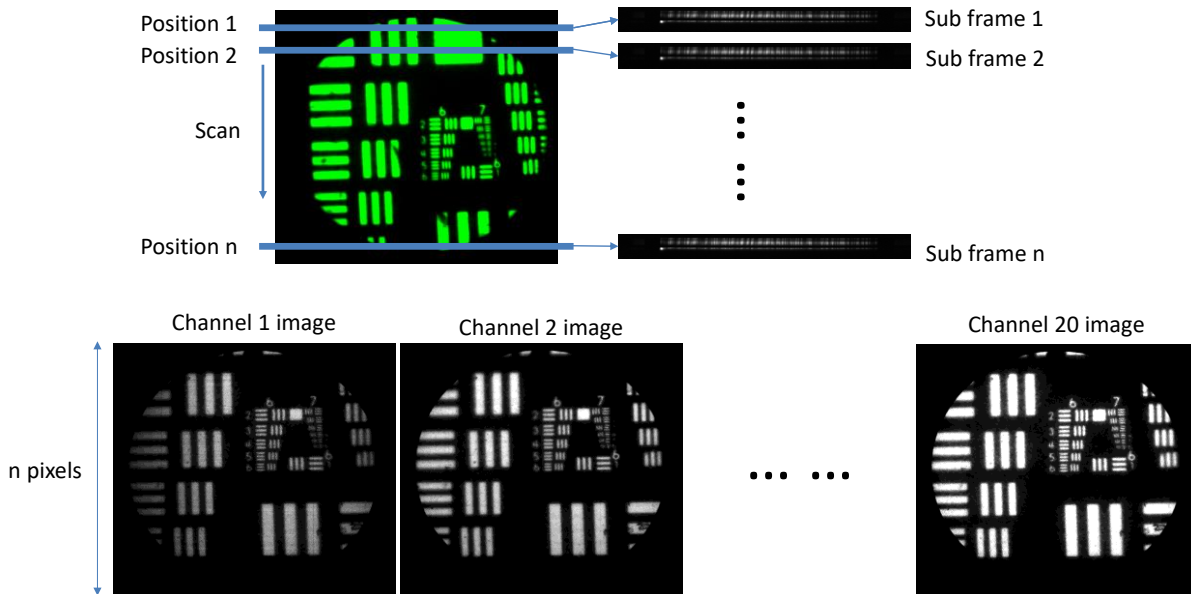


Fig. 2-8. Data collection by the MSCE system. As the scan mirror moves the illumination across the fiber, the sensor reads out multiple subframes.

Fig. 2-8 shows the process of data acquisition in the MSCE system. For a fixed position of the scan mirror, the CMOS image sensor (Basler acA640-750um) collects a 2D data set that consists of one spatial dimension (along the slit direction – 640 pixels) and a spectral dimension

perpendicular to the slit (20 pixels in the spectral dispersion direction). As the scan mirror moves the illumination across the fiber bundle, more and more subframes are collected. Collection of 430 subframes covers slightly more than the full 750-micron field of view of the fiber probe. A full frame of multi-spectral data consists of 20 spectral images with 480 x 430 pixels per spectral image. The 20 different spectral channel images are mapped to a single RGB image. The method is based on the CIE color mapping functions. For some dye combinations with overlapping spectra, a spectral unmixing method can be utilized to better distinguish the color contrast between the two dyes.

The reduction from 640 pixels to 480 pixels in the along-slit direction is done to better match the field of view with some flexibility in positioning of the circular field of view in the multispectral data set. The exposure time of the sensor can be set to 202 μs for each subframe, which correspond to 4950 subframes per second. However, due to the calculation time and display time between each multispectral frame, the system can only collect 4300 subframes per second, which yields a full multispectral frame rate of 10 frames per second. In this dissertation, the exposure time is set to 340 μs for each subframe to have a higher signal-noise ratio, and corresponds to a full multispectral frame rate of 6 frames per second.

2.5 Linear Spectral Unmixing with Multiple Dyes

Some dye combinations have a similar or highly overlapped spectrum, such as a combination of Proflavine (DNA-binding) and Phloxine B (connective tissue binding). With general CIE color mapping functions, the color contrast is not sufficient.

The spectral signal from dye combinations applied here is a linear mixture model, so to improve the color contrast, a linear spectral unmixing algorithm is applied to decompose the mixed fluorescence signal. Assume the normalized spectrum signal for certain contrast agents is

$\hat{s}(\lambda)$, the signal weight for it is f , then the spectrum $\hat{s}_{mix}(\lambda)$ for combination of n different dye is:

$$\hat{s}_{mix}(\lambda) = H \begin{pmatrix} f_1 \\ f_2 \\ \vdots \\ f_n \end{pmatrix}; \quad (2.5.1)$$

where H is the sensitivity function, comprised of a normalized spectrum signal for each dye:

$$H = (\hat{s}_1(\lambda), \hat{s}_2(\lambda), \dots, \hat{s}_n(\lambda)). \quad (2.5.2)$$

The the signal weight for each dye can be obtained by:

$$\begin{pmatrix} f_1 \\ f_2 \\ \vdots \\ f_n \end{pmatrix} = H^\# \hat{s}_{mix}(\lambda), \quad (2.5.3)$$

where $H^\#$ is the pseudoinverse of H :

$$H^\# = (H^t H)^{-1} H^t. \quad (2.5.4)$$

Fig. 2-9 shows 3 groups of images from different tissue samples with different color mapping functions.

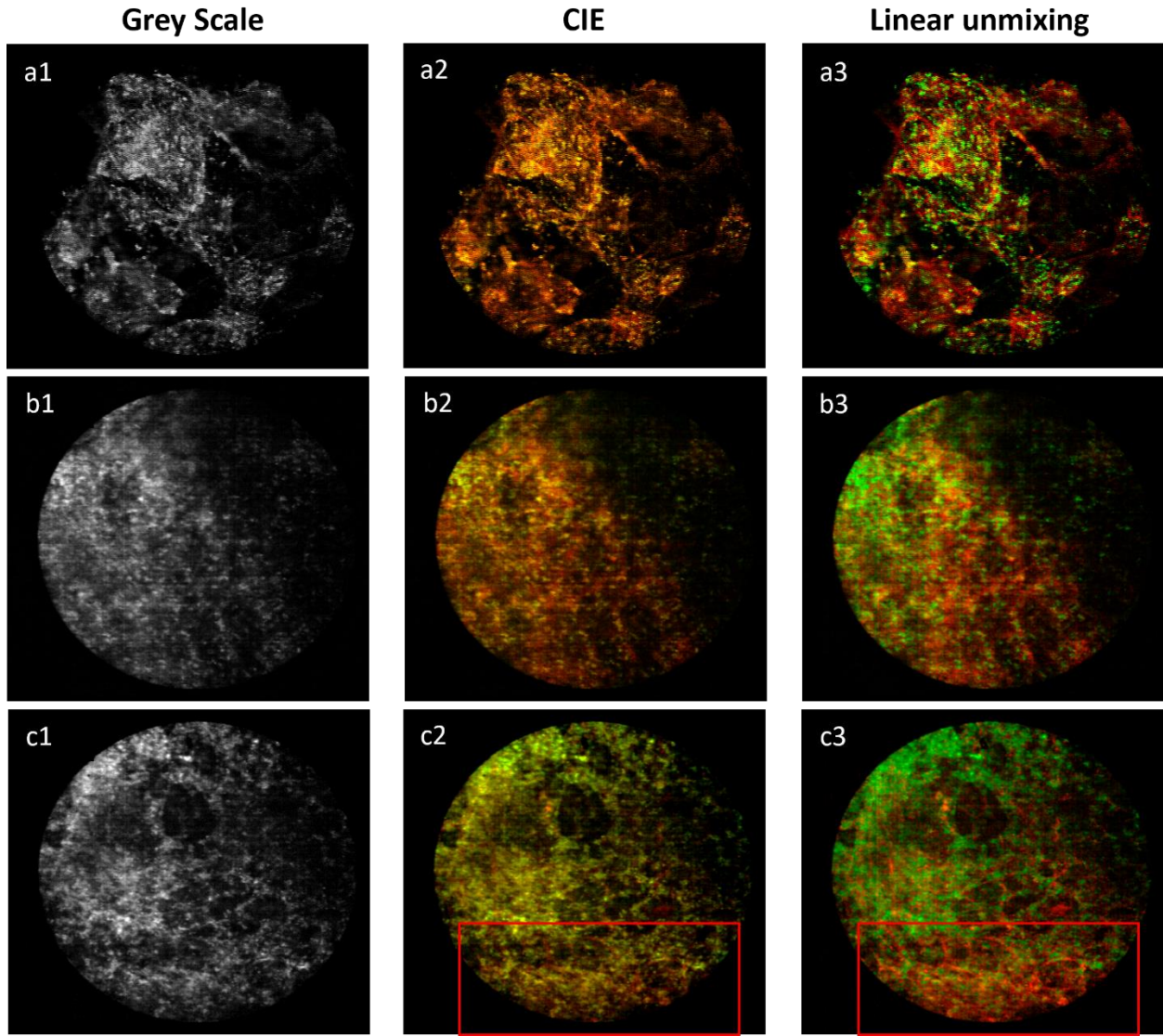


Fig. 2-9. Human ex-vivo tissue and Rat lung tissue with different color mapping function. Imaged with MSCE.

All images are obtained with MSCE with a dye combination of proflavine (DNA-binding, green) and rose bengal (protein tissue-binding, red). The first row of images is obtained from human ex-vivo tissue, which is from core biopsy extraction. In both grayscale (a1) and CIE mode (a2), it is not easy to distinguish connective tissue. But after the application of the spectral unmixing algorithm(a3), the color contrast between the cell nucleus and connective tissue is more pronounced. Similarly, in the second row of images, the linear spectral unmixing algorithm

significantly improves the visibility of connective tissue. The third row of images indicates that spectral unmixing algorithm can not only improve color contrast between different dyes but can also adjust the dye signal weight individually. In the red box region in c2, the connective tissue is hard to resolve because rose bengal has less signal level than proflavine here. However, c3 illustrates that spectral unmixing algorithm can help improve the signal level of rose bengal individually and highlight the connective tissue.

2.6 System Interfaces

To synchronize the scan mirror and image sensor readout, both devices are connected to a function generator. The whole system is connected to a PC and controlled by a LabVIEW program. The sensor sends a trigger signal to the function generator every time it collects a subframe. The function generator sends a ramp-shaped voltage signal that continues to rise linearly for the time it takes to collect an entire data set of 430 subframes. The necessary image processing algorithm is written and applied in LabVIEW, which has sufficient calculation speed to work under real-time imaging conditions.

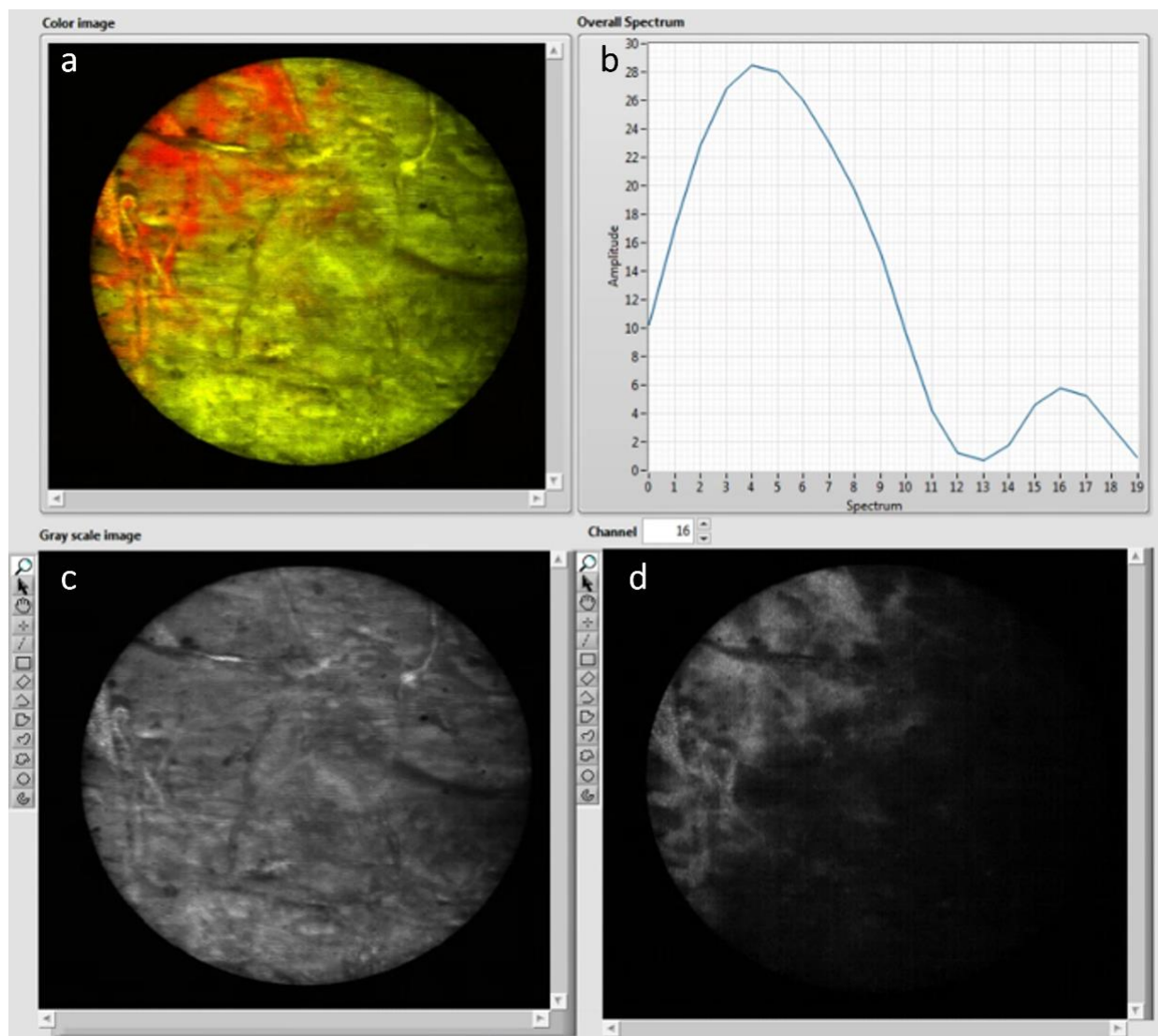


Fig. 2-10. Display windows in LabVIEW front panel. Images were collected from paper marked by fluorescent marker pens. a: this window shows the color image after the program has color mapped the signals of 20 channels; b: a spectral plot, the x-axis is the channel number; the y-axis corresponds to the pixel signal intensity of each channel over the whole image; c: the grayscale image; d: the grayscale image of one channel, changing the number above this window will change the displayed channel.

A Gaussian blur filter was used to reduce the fiber bundle's pixelization problem. The interface program controls the multi-channel laser (488 nm, 640 nm and 780 nm) intensity for use with different dyes, as well as sensor parameters, including exposure time and gain.

Fig. 2-10 shows data from a piece of paper stained with different fluorescence marker pens. The windows displayed are: a) a multi-spectral image window with adjustable color mapping

functions; b) a spectrum of the fluorescence emission over the whole image field of view; c) a grayscale image summed over all 20 spectral channels, and; d) an image at spectral channel 16 in the red end of the spectrum. During operation, the windows can be displayed individually or simultaneously together. The spectral distribution plot can be data at a single spatial pixel or averaged over any selected region of interest in the image sensor space.

A detail program manual can be found in chapter 4.

2.7 Tools in Lung Needle Biopsy with MSCE

Exogenous fluorescent dyes are employed to provide contrast for identifying cell nuclei and connective tissue in the multispectral images. The fluorescent dyes used in this work are FDA approved. Although multiple dye combinations were previously investigated²⁶, the work presented here with excised human and excised rodent lung tissue was all done using a combination of proflavine as a nuclear stain and rose bengal as a proteinaceous connective tissue stain. To minimize risk and limit patient exposure in future validation studies, fluorescent dyes will be delivered topically to the lung tissue. Fig. 3 shows the series of events that will be employed for in vivo dye delivery and imaging. First the introducer needle with stylet in place is inserted into the patient under CT guidance, which is a normal part of the core biopsy procedure. Then the stylet is removed, and the fiber bundle probe is inserted. The fiber bundle probe and dye delivery apparatus will be assembled and sterilized prior to use in the clinical core biopsy procedure. When the fiber bundle probe is in place with its distal end in contact with the tissue at the tip of the introducer needle, a small volume of fluorescent dye (on the order of 25 μ l) will be delivered to the tissue. In real-time the operating physician can evaluate the images on a monitor and make an assessment of whether the tissue being imaged is appropriate for biopsy (i.e., that the needle is in the nodule and at a location where it is giving relevant diagnostic information).

At that point, the fiber probe would be removed, and the standard core-biopsy needle inserted to collect one or more core tissue samples.

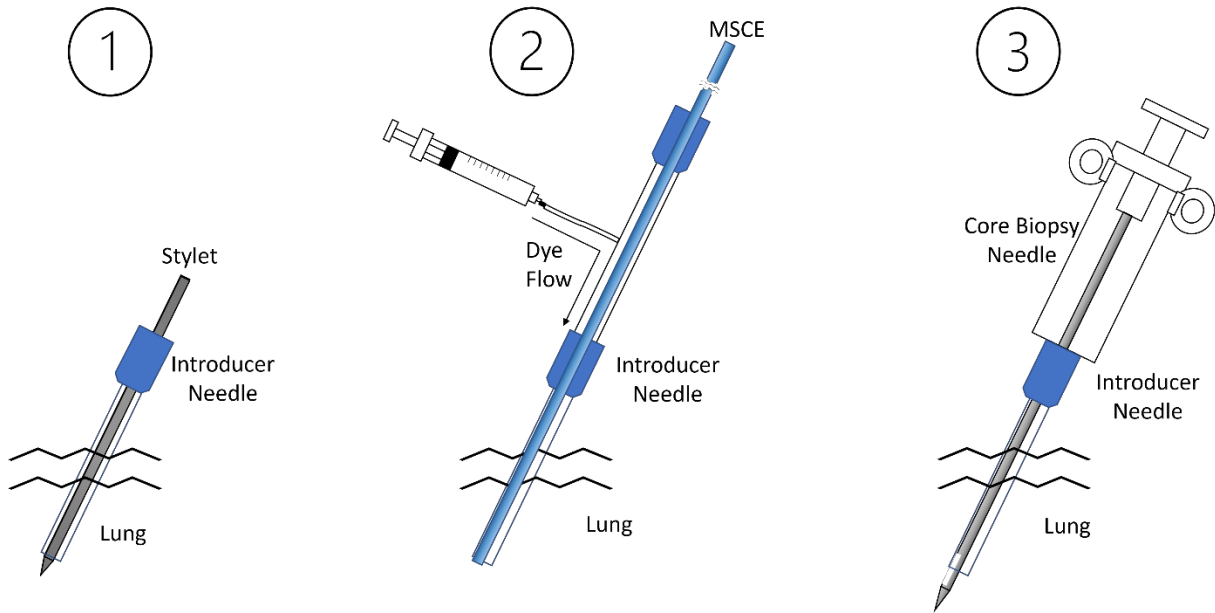


Fig. 2-11. lung biopsy procedure with MSCE.

Steps 1 and 2 have been demonstrated while imaging the normal lung of a euthanized rat. The images obtained from these animal experiments are presented in the results section and in supplementary material. Step 3 is a standard part of the core biopsy procedure in humans but was not tested in the rodent model due to the small size of the organ.

The maximum time-averaged irradiance of 3.5 mW/mm^2 can be delivered to the tissue during the fiber probe endomicroscopy imaging process. Most times, a time-averaged irradiance of 1 mW/mm^2 is sufficient for the lung imaging application.

Fig. 2-12 shows the actual instruments used in this project to perform the fluorescence endomicroscopic imaging and core biopsy procedure.

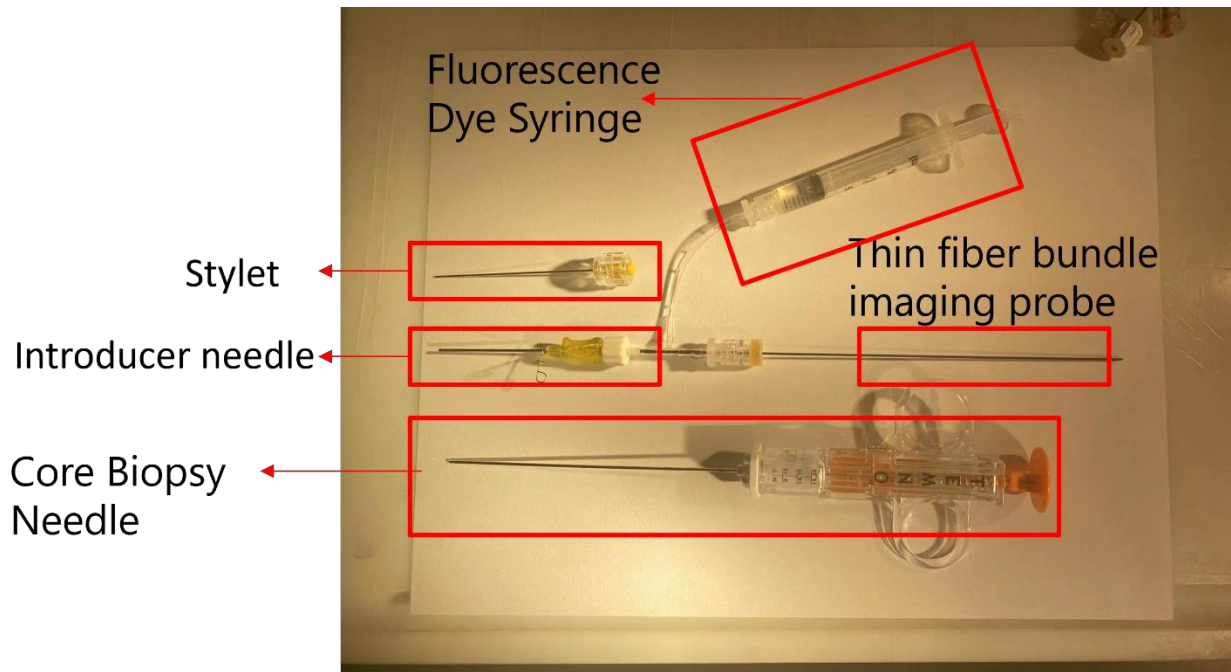


Fig. 2-12. Real instruments used in this project for implementing the dye delivery, endomicroscopy imaging, and core biopsy tissue collection procedure.

2.8 Summary

This chapter describes the principle of the system, the design of the optical system, and its control software.

In order to better help physicians identify tissue structures and select appropriate samples, we inserted dispersive elements into the original monochromatic confocal system design and transformed it into a multispectral confocal endomicroscope, MSCE.

The MSCE system is a multispectral confocal system based on a fiber bundle probe, so its optical components requires high axial chromatic aberration correction , and since the fiber bundle probe is the main factor limiting the resolution, the components in the system need to be selected according to the sampling frequency of the fiber bundle probe. After comparing three different designs, we decided to adopt the last one, which uses off-shelf lenses whose imaging quality is acceptable and easy to purchase. After weighing the signal-to-noise ratio and frame

rate, the system finally used has a 6 fps mode to capture real-time images with high signal-to-noise ratio.

In order to synchronize the various components of the MSCE system and also to process the images in real time, the system is completely controlled by LabVIEW on a PC. In the image processing and display part, this system not only has the usual CIE mapping function, but also for use of a spectral unmixing algorithm to better distinguish the fluorescence signals of the two dyes. The next sections elaborate on the composition of the LabVIEW software and how to use it to control the MSCE system.

3 MSCE LabVIEW Manual

3.1 Program Overview

In the previous chapter, the hardware parameters and system performance parameters were given, including spatial resolution and frame rate. In this chapter, the LabVIEW based MSCE control program is described in detail, including the interface, usage, and the logic behind each module. When designing the program, the biggest problem is how to synchronize the readout frequency of the sensor and the scanning frequency of the scanning mirror, and how to design and optimize the algorithm to make the image processing speed meet the requirements of real-time imaging. At the end of this chapter, some of the program's remaining problems and future improvements are presented.

3.2 Program Front Panel

3.2.1. Display Windows

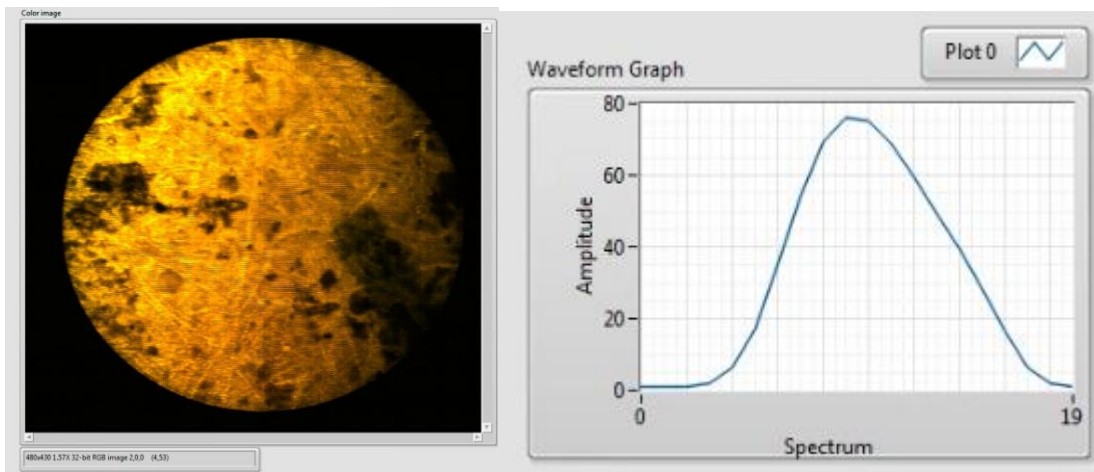


Fig. 3-1. Color image and overall spectral distribution in that image. The color channels from 0 thru 19 cover the wavelength range from 500-750nm.

Fig. 3-1 shows the RGB color image window and the overall spectrum of the object. These are the primary windows that we use to guide the biopsy and see the color difference between structures.

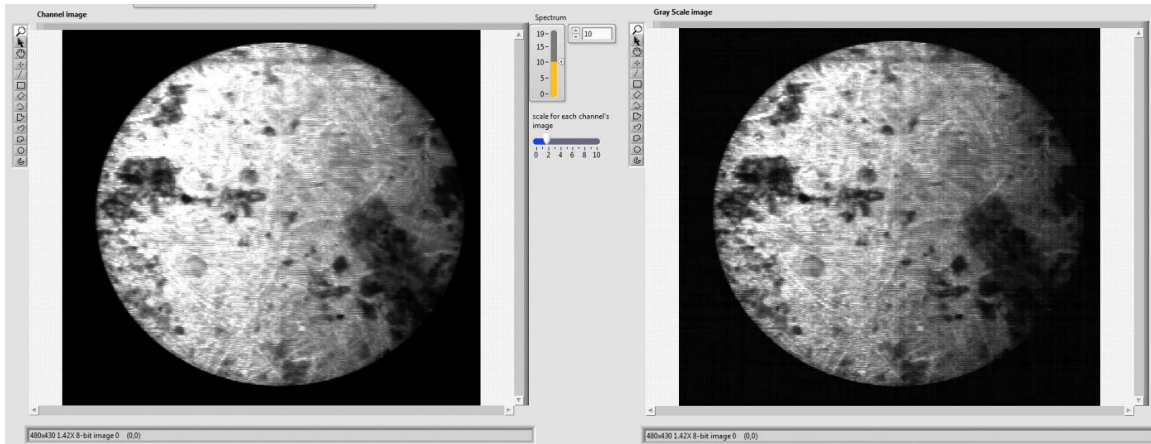


Fig. 3-2 Image for certain channel.

Fig. 3-2 shows the window for the image of one channel and the window for grayscale image, which is the sum of all 20 spectral channels. By scrolling the yellow slider or entering the number in the window, we can select whichever channel we want to see. Most of the time, the signal level for each channel is much lower than either color image or grayscale image. However, by changing the blue slider in Fig. 3-2, we can change the display scale factor to enhance the image. The right window shows the grayscale image of the object.

3.2.2. Sensor and display parameter controls

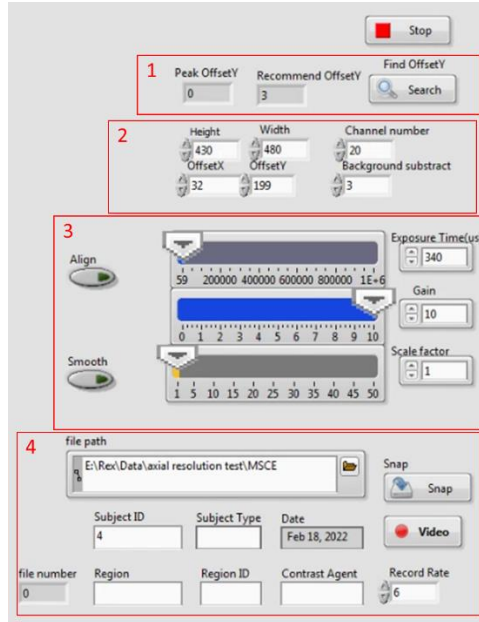


Fig. 3-3 LabVIEW sensor and display control panels.

Fig. 3-3 shows the sensor and display control panels. A “Stop” button at the top ends the program and turns off the laser. Inside the first red box is a tool that helps users select the region of interest to be displayed. This is primarily a tool that helps find where the data are located on the sensor after a system realignment. When it is not known which row the signal is in, by clicking the search button in the red box, this tool displays the row of the current maximum signal intensity and the recommended value of OffsetY.

The second red box indicates the height, width, number of channels, and offset along x and y of the final image. The width and OffsetX determine the horizontal position of the subframe on the sensor. The width and OffsetX have to be an integer multiple of 32. The number of channels and OffsetY determines the vertical position of the subframe on the sensor. The height determines the number of subframes required for the final image.

The controller in the third red box can be used to adjust some sensor parameters and display parameters. The exposure time refers to the exposure time of each subframe grabbed by the sensor rather than the exposure time of the entire image. At an exposure time of 340 ms, 430 subframes can be collected in approximately 167 μ s resulting in a real-time frame rate of 6 frames of multispectral images per second . This exposure time affects the signal-to-noise ratio and signal intensity of the image. However, it is also one of the critical parameters for synchronizing the sensor and the scanning mirror. Every time we adjust the exposure time, we need to find the appropriate timing of the scanning mirror to make the picture stable. "Gain" refers to the gain parameter when the sensor acquires the signal, which primarily affects the signal intensity. Unlike the gain, the scale factor is used to adjust the display intensity of the signal that has already been digitized. It is used mostly for low-level signals to map them into a more visible signal. The Align button is used to reset the synchronization. Sometimes, the sensor and scanning mirror can be synchronized but have some phase difference, as shown in the left image of Fig. 3-4. In this case, we can click the align button to reset the synchronization. This button can turn off the sensor for 0.5 seconds and then turn the sensor back after the scanning period has ended.

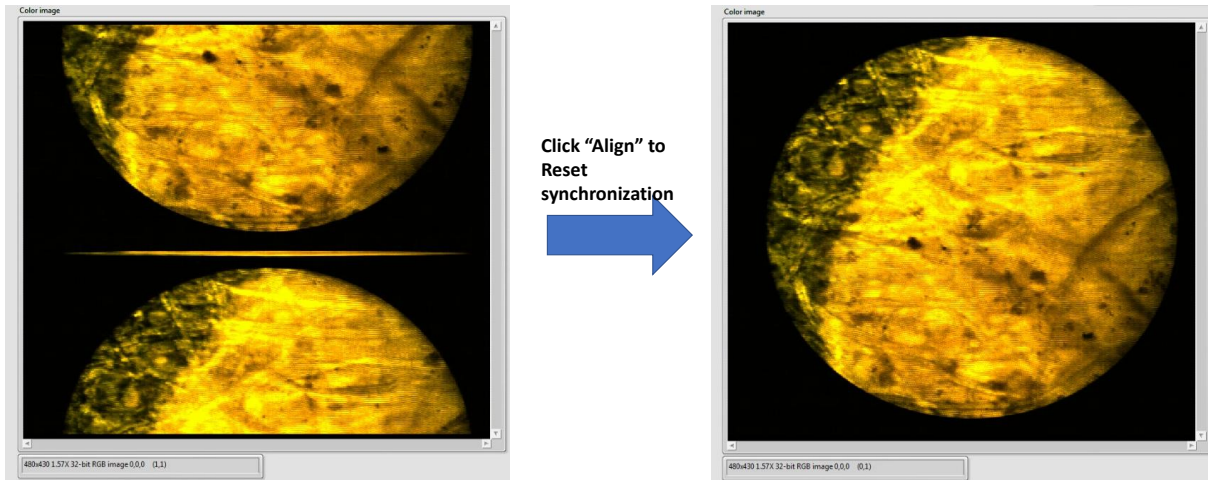


Fig. 3-4. Align button pressed to reset synchronization.

The “smooth” button reduces the pixelization effect of the fiber bundle probe by introducing a gaussian smoothing operation to the original image. It should be noted that this smoothing method will not improve the inherent sampling frequency of the fiber bundle, but it does reduce the structured noise of the fiber bundle pattern. The pixelization effect is discussed in chapter 5.



Fig. 3-5. Introduction of a Gaussian filter to remove pixelization.

Inside the fourth red box is the function to store files. By filling in the file path and file name, users can tap “Snap” to record a single static image or click “Video” to record a continuous dynamic series. It is worth noting that recording a static image or a continuous series when the

CPU is busy may make the system lose synchronization. Users can resynchronize the system by clicking “Align”.

3.2.3. Function Generator Control

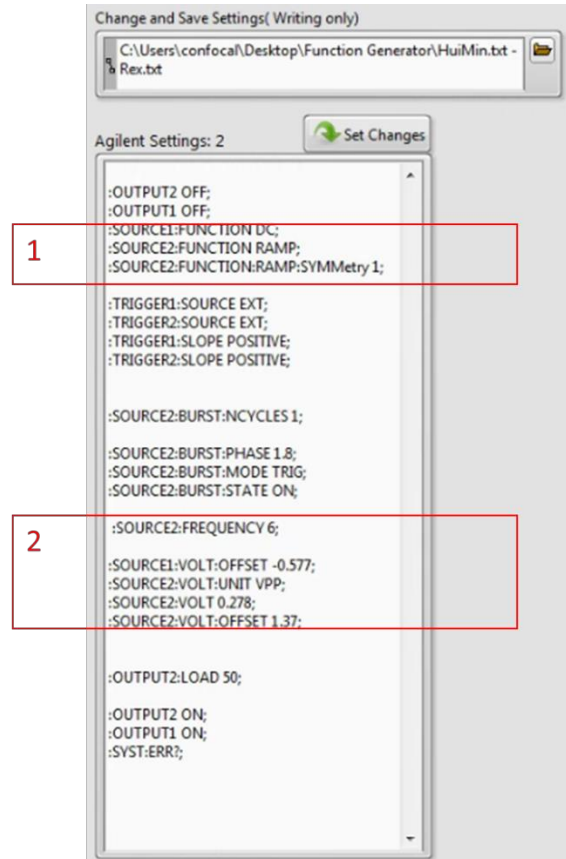


Fig. 3-6. Function generator control.

Fig. 3-6 shows the parameters that controls the scan signal shape, including the offset, period, and amplitude of the function generator waveform. There are two scanning mirrors in the current MSCE setup. The second scanning mirror is set at a fixed angle as a folding mirror. The first scanning mirror is connected to the signal source of the function generator. The red boxes highlight some key parameters. The folding mirror after the second tube lens is controlled by SOURCE 1; the scanning mirror before the objective is controlled by SOURCE 2.

The first red box shows the statements that describe the shapes of the signals. Because the second mirror performs as a folding mirror, SOURCE 1 outputs a DC signal. SOURCE 2 is connected to the scanning mirror, and its scanning mode is to scan the line illumination uniformly over the whole FOV and then reset it quickly, so it uses a RAMP function of 99:1. The "SYMMETRY: 1" value in the red box describes this ratio.

In the second red box, "SOURCE 2: FREQUENCY: 6" describes the period of the scanner, i.e., the ramp function is repeated 6 times per second, which determines the displayed frame rate. "SOURCE1: VOLT: OFFSET" describes the angle of the folding mirror, which determines where the signal is projected on the sensor. "SOURCE2:VOLT" describes the scanning range of the mirror, which determines the FOV range. "SOURCE2:VOLT:OFFSET" describes the starting angle of the scanning mirror, which determines the starting position of the FOV.

3.2.4. Color Display Control

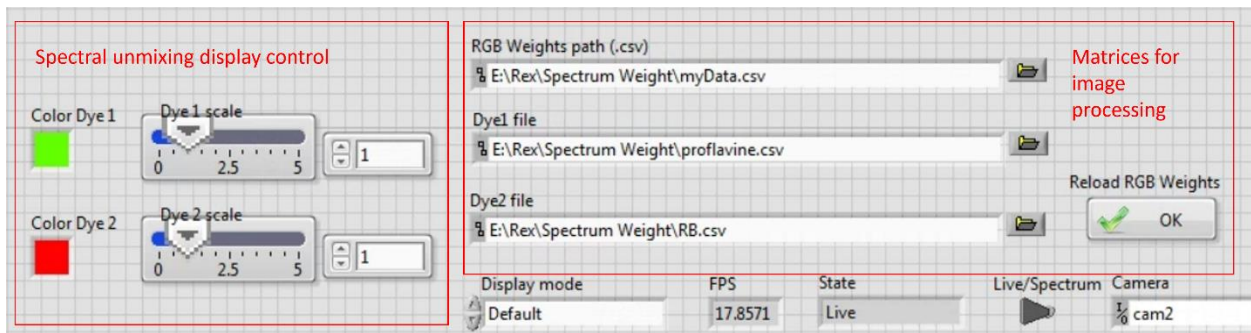


Fig. 3-7. Color display control panel.

Fig. 3-7 shows the color display control interface of the program. The red box on the right are the read paths for the matrices needed for color image processing. At system startup, the last files are automatically read, after which the system will not update the internal cache of these matrices unless the user clicks the Reload RGB weights button. "Dye1 file" and "Dye2 file" correspond to the individual spectrum of the two dyes in the spectral unmixing algorithm, respectively. By

clicking "Display mode", users can switch between "default mode" and "spectral unmixing mode". The default mode uses a file that describes the 3 RGB weights for each spectral channel. The user can define any mapping of spectral channel signal values to RGB values that is desired. These mapping values are stored in an Excel (.csv) file format.

In the red box on the left are the control options in the spectral unmixing mode. "Color dye1" and "Color dye2" indicate which color the user wants to use to display dye 1 and dye 2, while the scale bars indicate the intensity scale factor of each dye.

3.3 Program Logic Flow

3.3.1. Default Live Mode

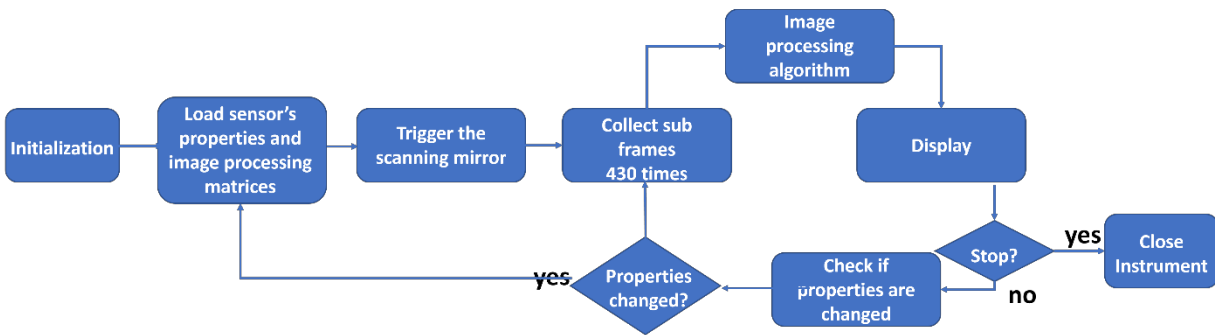


Fig. 3-8. Logic flow for default live mode.

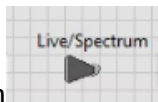
Fig. 3-8 shows the logic of the program in default mode. When the user opens the program and does not perform any operation, it enters the default mode. In the first step, the program initializes all device parameters, ports, and switches. Then the program reads all parameters of the current interface, which include:

1. The intensity of the three laser sources.
2. The parameters of the sensor: exposure time, gain, ROI of the sensor (i.e., width, channel number, offset X, offset Y).

3. Parameters of the function generator: parameters written into the Agilent setting text, the meaning of the critical parameters in the text has been described above.
4. Image processing switches and parameters: display image height, display scale factor, smooth button, display mode (default RGB mode or spectral unmixing mode), mapping function in RGB mode, and the scale factors for the spectral unmixing algorithm.

After reading all the parameters, the program will put the sensor into capture mode, and at the same time, the sensor will trigger the function generator to make it send preset signals to the two mirrors. After that, the sensor will collect 430 subframes in a loop and then process the subframes' images, which is described in the next section. The processed image and its spectral distribution will be displayed in the corresponding window. Finally, the program checks whether the above parameters have been changed and whether the stop button has been pressed and proceeds to the next cycle of data collection and image display.

3.3.2. Spectrum Mode



When this switch is turned to the right, the system enters spectrum mode, in which the program will display the raw subframe data instead of the processed image. The logic flow of this mode is shown in the Fig. 3-9.

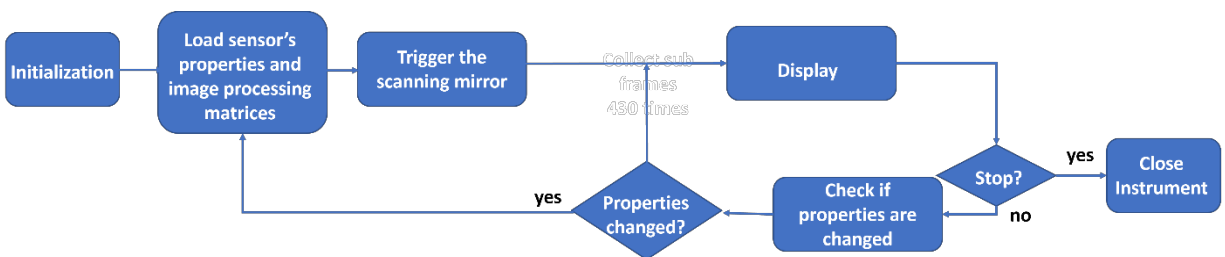


Fig. 3-9. Logic flow for spectrum mode.

Instead of collecting the subframe and performing image processing, this mode simply displays the subframe directly. This mode can help users view the real-time spectrum distribution, and check whether the signal is present within the desired ROI.

3.4 Synchronization of Sensor and Scanning Mirror

As mentioned above, synchronizing the scanning mirror and sensor was a tricky issue we faced in this project. Unlike monochrome systems, which have a second scanning mirror, the MSCE mode of operation does not have an active second scanning mirror. The second scanning process is accomplished by image processing the collected subframes in the LabVIEW program. So we need to make sure that the sensor collects exactly 430 subframes every time the first scanning mirror sweeps the field of view, which is not as simple as it might seem.

In our system, it is the sensor that triggers the function generator. Every time the sensor reads an image, it emits a trigger signal to the function generator. The function generator that receives the trigger signal emits a signal with a preset waveform to the scanning mirror. Then the scanning mirror moves according to the sweep waveform. The sensor's trigger signal does not trigger the function generator again until completion of the scan waveform. According to this, we proposed three different methods to accomplish synchronization.

3.4.1. Ramped Function with Paused Sensor

The first method is the most straightforward. It consists of the following steps: 1) collect the 430 subframes, 2) pause the sensor activity after 430 subframes are acquired, 2) wait for the function generator to finish the waveform, 3) add an idle time to allow the image display to complete its operation, and then 4) proceed to the next acquisition by turning sensor trigger signals back on.

We call the full waiting time (from B to A' in Fig. 3-10) the “dead time”. In this method, the

function generator uses a ramp waveform, and the ramp ratio can be freely adjusted.

Accordingly, the idle time also needs to be adjusted to complete the display operation.

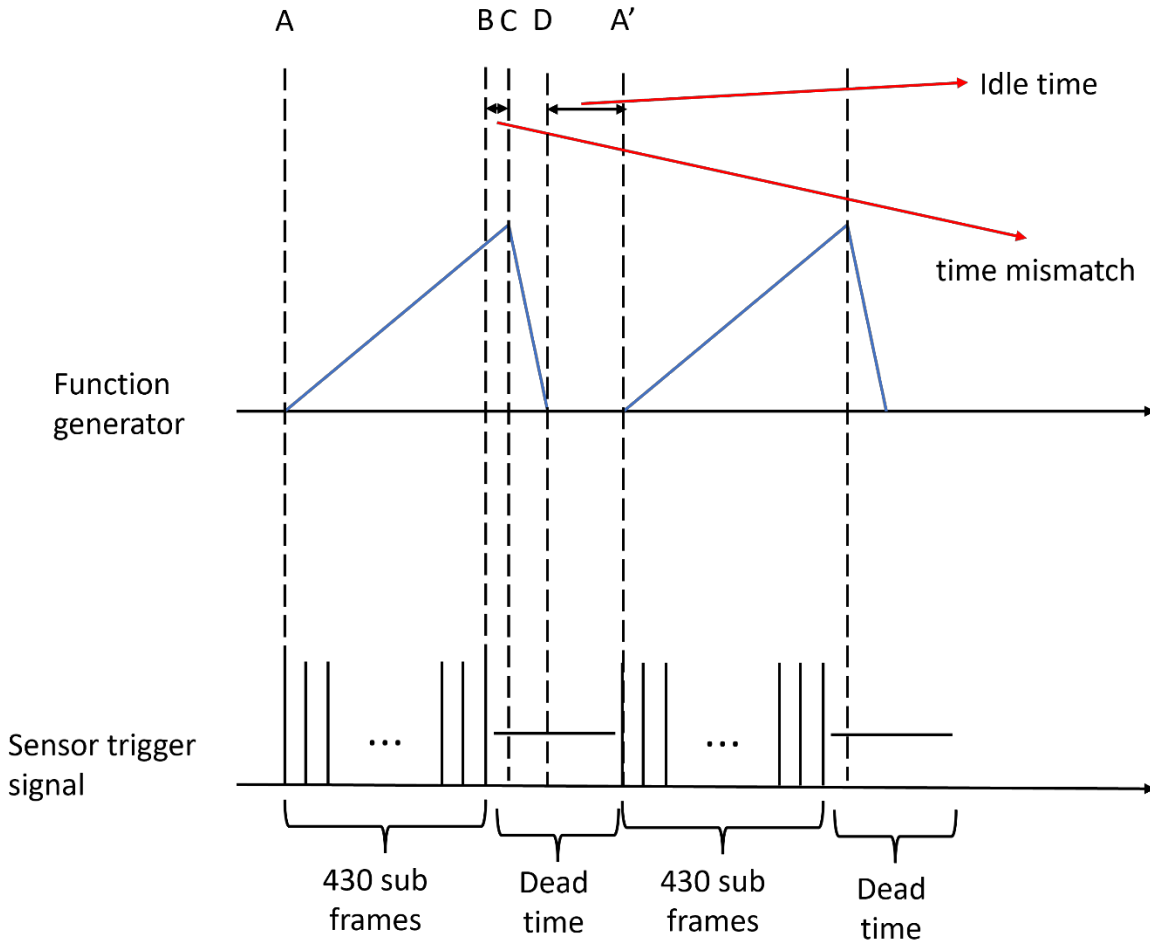


Fig. 3-10. Diagram showing the signal from the function generator and sensor trigger.

Fig. 3-10 describes the process of the sensor trigger signal and the function generator signal when we use this method. At moment A, the sensor starts to read the first subframe and sends a trigger signal to the function generator. The function generator, which receives the trigger signal, emits a preset ramp signal to drive the scanning mirror. At moment B, the sensor has finished reading 430 subframes and pauses its activity. However, the ramp function is still in the process of rising, which means that the scanning mirror still keeps moving in the original direction, but

the sensor is no longer reading subframe data. At moment C, the ramp function starts to fall, which means the scanning mirror starts to move back to the initial position. At moment D, the function generator enters standby mode while the sensor is still in dead time, and there will be no activity in the whole system other than implementing the multispectral image display until the next reading cycle starts (moment A').

We call the time from moment B to moment C the mismatch time and the time from moment D to moment A' the idle time. The total time from B to A' is called the dead time. The readout interval of the sensor is determined by its exposure time, while the waveform of the ramp function is controlled by the settings of the function generator. We want both the mismatch time and idle time to be as short as possible, so that the multispectral image frame rate of the system is maximized.

It is worth pointing out that the operating environment of a PC is complicated, and LabVIEW is a CPU-based software language for all computing operations, which leads to uncertainty of the computation time in LabVIEW. Therefore, all the time intervals above are subject to errors and fluctuations, and we often encounter them in our experiments. A certain network fluctuation or windows update may cause the system to lose synchronization. In order to keep the system synchronized, we need to ensure that the function generator is in a standby state before the first subframe of each cycle is ready to be collected by the sensor. By introducing sufficient dead time (moment B to moment A'), this method reserves enough time for the system to ensure that the function generator is in a standby state before the next cycle of data acquisition occurs. The most significant advantage of this method is its robustness. Due to the sufficient time reserved, the system can finish the synchronization easily even with errors and fluctuations. In addition, even

if a significant fluctuation causes a loss of synchronization, the system can be self-adjusting if a long enough dead time is reserved.

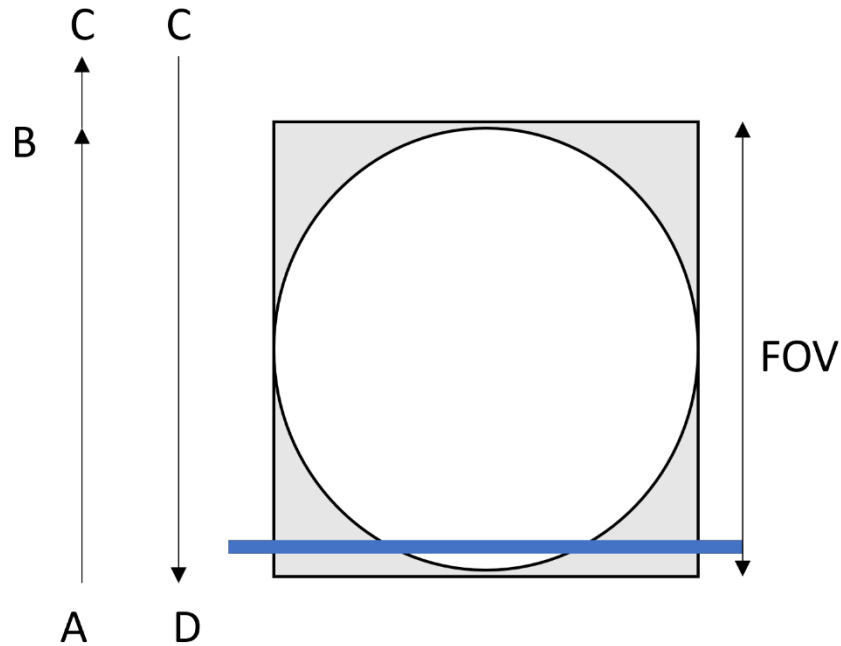


Fig. 3-11. Scanning process at distal tip of fiber bundle probe.

Fig. 3-11 illustrates the scanning of the system when this approach is used. At moment A to moment C, the scanning mirror sweeps the illumination line across the FOV while the sensor is acquiring subframe images. By changing the preset waveform of the function generator and the sensor's exposure time, we can make the interval between B and C as short as possible. At the time from C to D, the scanning mirror quickly returns to its original position.

However, this method has a significant drawback. Due to the introduction of the dead time, although the system is very stable, the overall frame rate is reduced. Theoretically, we can adjust the dead time so that the D and A' moments are very close to each other to reduce the impact of the dead time. However, we find that after suspending the sensor activity, the system needs a fixed period for the sensor to re-activate. This period affects the minimum value for the dead

time. Therefore, a dead time will be unavoidable. Furthermore, the robustness mentioned above can be improved by external means such as removing the software running on the PC as much as possible and blocking windows updates. Nevertheless, the frame rate is what we want to maximize, so we considered the following method.

3.4.2. Triangle Signal with Paused Sensor

The second method improves upon the first method by changing the waveform emitted by the function generator from a ramp function to a triangle function. Meanwhile, we pause the sensor's activity after it acquires two sets of subframes, which makes each dead time correspond to two full frames instead of one in the first method. Although the dead time still exists, this approach reduces its impact by having one dead time for two frames.

It is worth pointing out that the rise and fall of the triangle function represent the sweeping back and forth of the scanner during each cycle. Therefore, the images captured during rise and fall are reversed, and we need to reverse them in the program.

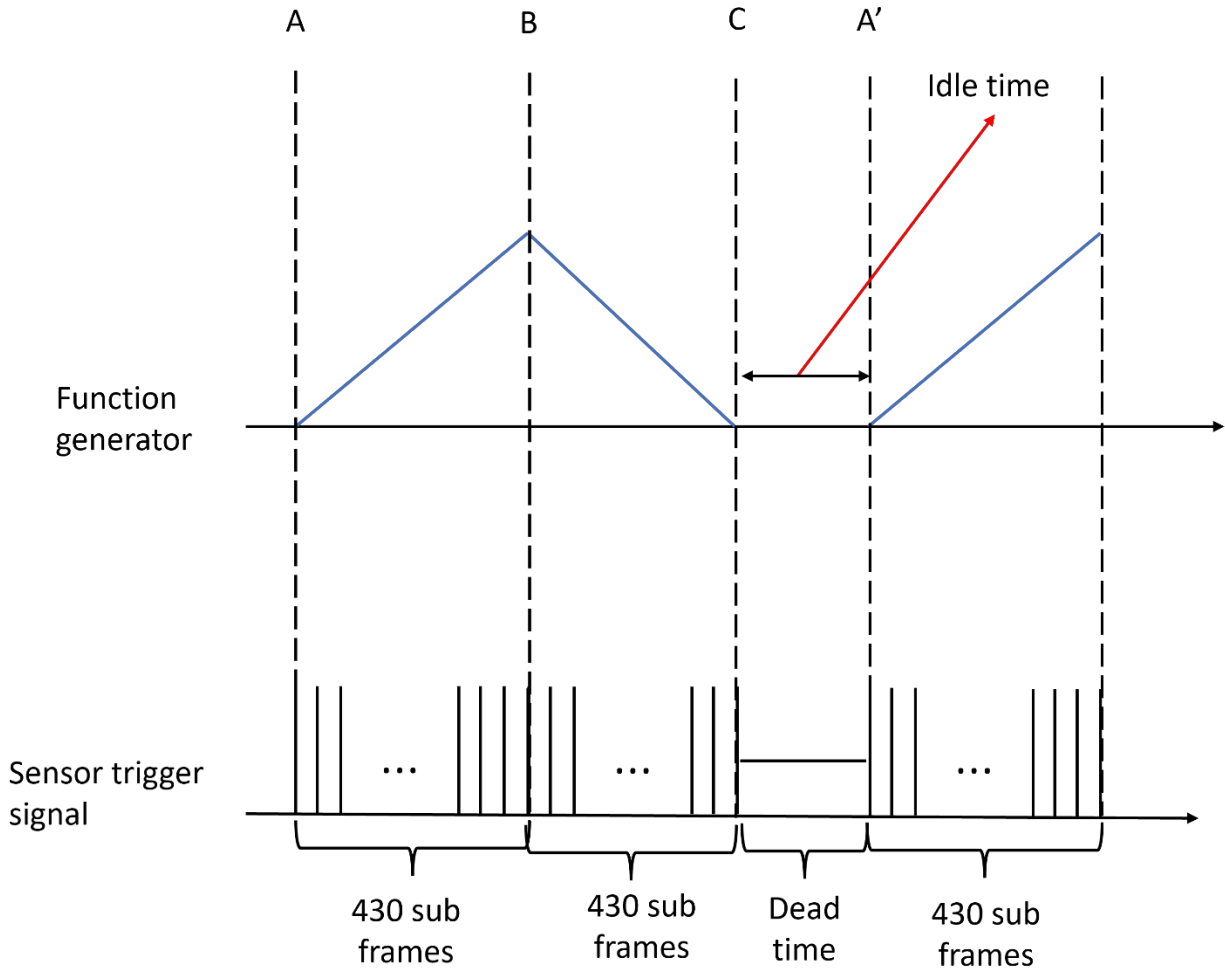


Fig. 3-12. Diagram showing the signals for the function generator and sensor triggers.

Fig. 3-12 depicts the sensor trigger signal and the function generator output signal when using this method. At moment A, the sensor reads the subframe for the first time and sends a trigger signal to the function generator. At this point, the function generator receives the trigger signal and sends out a preset triangular signal to drive the scanning mirror. At moment B, the sensor has completed reading the first 430 subframes. Then the sensor starts the second set of 430 subframe readings, the triangle function begins to descend, and the scanning mirror moves backward to the initial angle. At moment C, the function generator finishes the triangle waveform and enters standby mode, while the sensor also finishes the second read and enters

pause mode. Until the next read starts (moment A'), there will be no activity in the whole system except for the display operations.

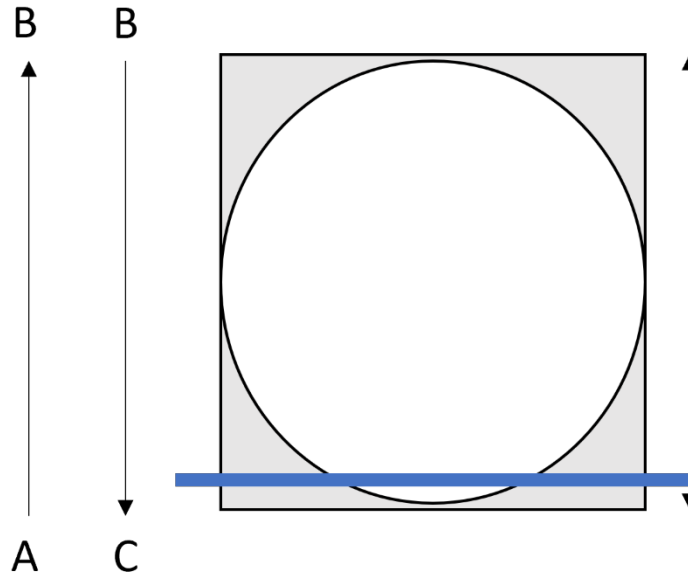


Fig. 3-13. Scanning process of the fiber bundle probe.

Fig. 3-13 illustrates the scanning process of the system when this approach is used. The scanning mirror slowly sweeps up from moment A to moment B while the sensor is acquiring subframe data. The illumination beam sweeps through the fiber bundle distal tip during this time. During the time from the B to C, the illumination beam returns to the original position at the same speed, and the sensor is in the second set of subframe acquisitions.

The advantage of this method is that the effect of the dead time on the frame rate is reduced compared to the first method. This method has a higher frame rate than the first method. However, it is more demanding to write the program because the scanner has two opposite scan paths in the waveform period, so the images obtained twice have opposite scan polarity. We need to correct the reversed images during the image processing. However, this still does not

completely solve the frame rate degradation problem caused by dead time, so we proposed and developed a third method.

3.4.3. Ramped Function with Free-Run Sensor

In the third method, we allow the sensor to operate in free-run mode instead of pausing it. Fig. 3-14 shows the relationship between the sensor trigger signal and the signal sent by the function generator when we use this method. When the sensor is ready to collect the first subframe, it sends a trigger signal to the function generator, the same as in the first method. This trigger signal will cause the function generator to start sending a preset waveform to the scanner. Unlike the first method, when moment B is reached, the scanner starts to return to the initial angle, but the sensor has not yet completed the acquisition of the 430th subframe. At moment C, the function generator completes sending the waveform just after the sensor collects the 430th subframe but has not yet started to collect the 1st subframe of the next round. At this moment, scanner has returned to the starting position. Then at moment A', the sensor starts the next round of subframes acquisition and sends the trigger signal to the function generator. Thus, the system enters the next period.

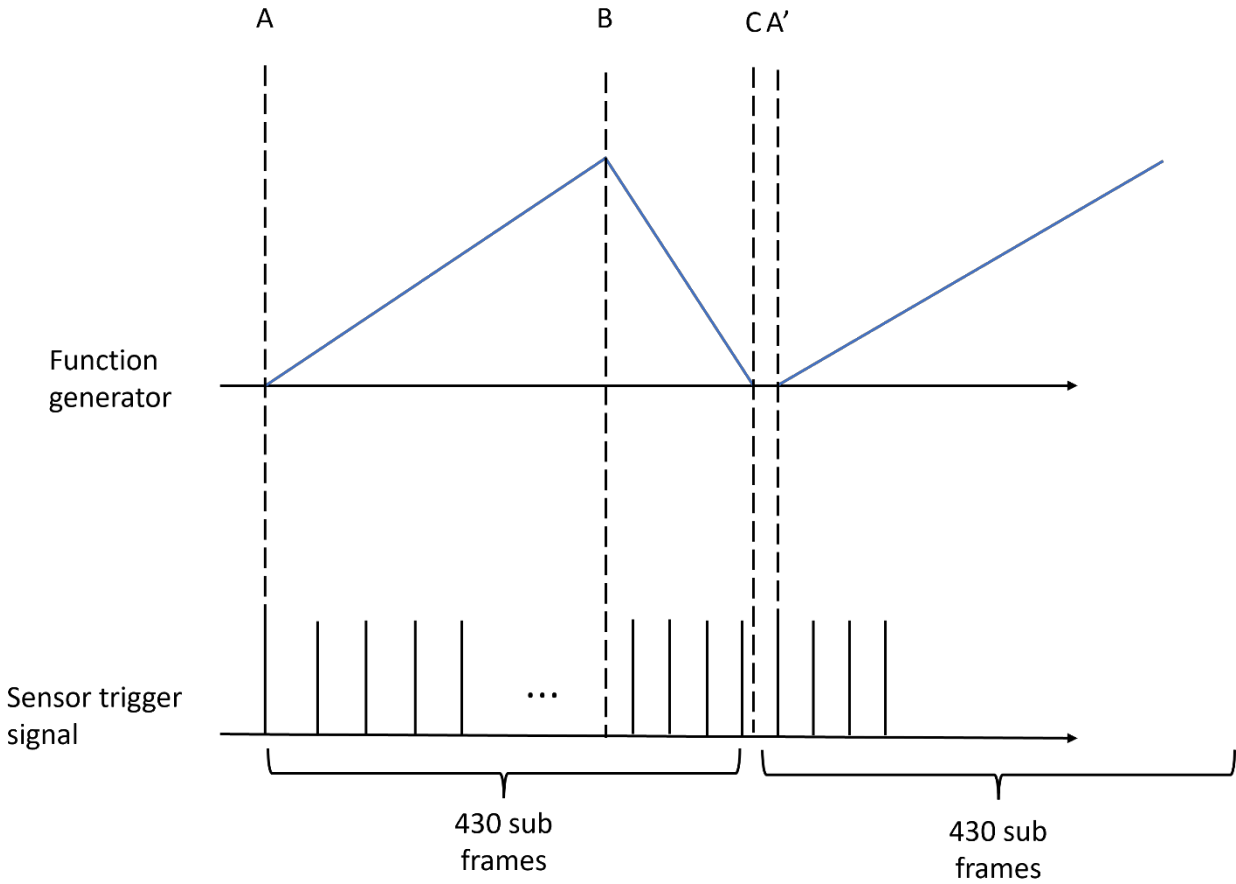


Fig. 3-14. Diagram showing the signals for the function generator and sensor triggers.

We use a ramp function with a ratio of 99:1 (AB: BC), so the last few frames of the subframe will inevitably acquire some images of the BC period. We could circumvent this problem by increasing the ratio of the ramp function to 430:1 or higher, but this will create a very rapid return of the scan mirror, which could damage the scan mirror. As can be seen in the images in the result chapter, the 99:1 ratio has minimal impact on the image quality of the imaging system.

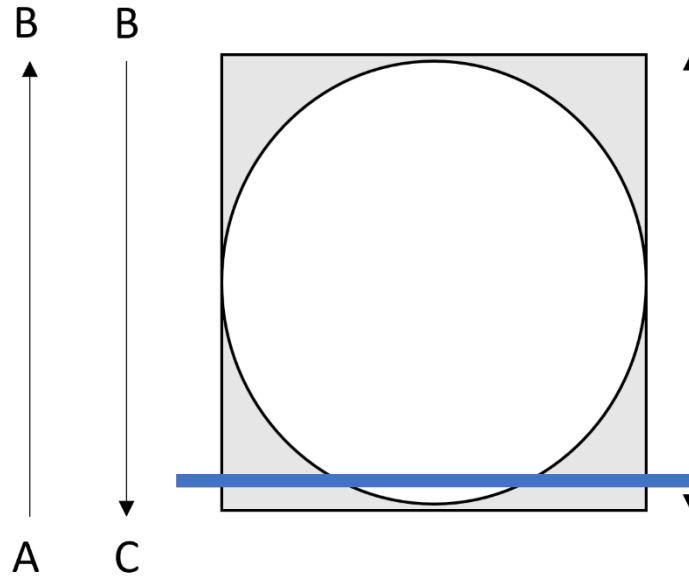


Fig. 3-15. Scanning process of the line illumination at the fiber bundle probe.

Fig. 3-15 illustrates the scanning process of the illumination beam when this method is used. When it is at moment A to moment B, the scanner is sweeping to the top, while the sensor is acquiring subframe image data. From A to B, the system sweeps through the fiber bundle distal tip, and from B to C, the illumination beam returns to its original position very quickly, while the sensor is about to finish acquiring the first set of subframes. By changing the preset waveform of the function generator and the exposure time of the sensor, we can make the sensor complete the first set of acquisitions at time C.

As mentioned above, the potential drawback of this method is that the last few frames of the subframe will capture unwanted information, but we can prevent display of this unwanted information as part of the image processing algorithm. We can also see that this method is more vulnerable to system fluctuations than the previous two methods, and it does not automatically restore synchronization when it is lost. The advantage of this system is also obvious: it has the

highest frame rate of all methods. Since the sensor is in free-run mode, it acquires images without interruption.

In practice, we found that this method can maintain a relatively stable synchronization in most cases. Even if we lose synchronization, we can switch this mode to the first mode to let the system automatically resume synchronization, which we call "Align". After resuming synchronization, we can switch back to the third mode to improve the frame rate. At the beginning of this chapter, we mentioned the "Align" button is used to accomplish this step.

In the end we decided to use the third method for general data acquisition and the first method to restore synchronization if synchronization is lost.

3.5 Image Processing Algorithms

This section describes in detail the image processing methods employed in the system, including how to process the collected subframe groups to obtain grayscale maps, how to use the 20 different wavelength channels in RGB images, and how to obtain the spectrum.

3.5.1. From Subframes to Grayscale

The first and most straightforward step is how do we revert the 430 subframes to a grayscale map with full FOV. We need to find a fast image processing method because a slow image processing method will reduce the frame rate and may cause fluctuations that can cause the system to lose synchronization.

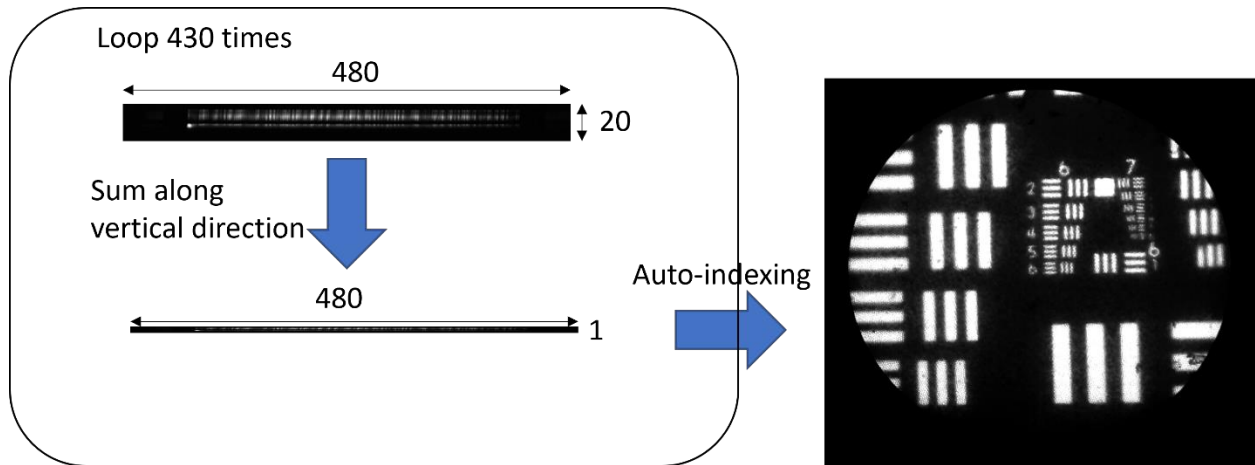


Fig. 3-16. Process to get a grayscale image.

Fig. 3-16 shows the process to get a grayscale image. When the sensor captures a subframe, it stores the subframe in the LabVIEW cache as a two-dimensional (20X480) matrix. At the same time, we add values of the subframe along the first (spectral) dimension to get a 1X480 vector. Then we output this vector in auto-indexing tunnel mode. Auto-indexing means that when using a for-loop, LabVIEW can combine the elements or vectors of each loop and output them. So, after 430 loops, we can get a matrix of 480X430 size and transpose it to get a 430X480 matrix. This matrix is the grayscale map.

We use auto-indexing tunnel mode to output and cache the vectors instead of inserting each subframe into a blank matrix. This reduces redundancy and increases the speed of operations.

3.5.2. From Spectrum to Color Display

The color display is one of the most essential image processing steps in the MSCE system. As mentioned before, there are many ways to convert spectral information into RGB information that can be displayed as a color image. In this step, the most critical thing is finding or setting the RGB weights corresponding to each spectrum channel. Let us start by looking at how the system

converts the information from 20 different channels into RGB information once we have the RGB weight matrix.

Assume the subframe matrix is $(\vec{s}_1, \vec{s}_2, \dots, \vec{s}_{20})$, where each \vec{s} represents the vector composed of 480 elements of the corresponding channel. Our goal is to get the three vectors corresponding to the RGB channels, $(\vec{s}_R, \vec{s}_G, \vec{s}_B)$.

Assume that the RGB weight matrix is $\begin{pmatrix} r_1 & g_1 & b_1 \\ \vdots & \vdots & \vdots \\ r_{20} & g_{20} & b_{20} \end{pmatrix}$. Each element of this matrix

represents the weight of the corresponding spectral channel on the red, green, and blue color channels. These matrices are related as follows:

$$(\vec{s}_R, \vec{s}_G, \vec{s}_B) = (\vec{s}_1, \vec{s}_2, \dots, \vec{s}_{20}) \times \begin{pmatrix} r_1 & g_1 & b_1 \\ \vdots & \vdots & \vdots \\ r_{20} & g_{20} & b_{20} \end{pmatrix} \quad (3.5.1)$$

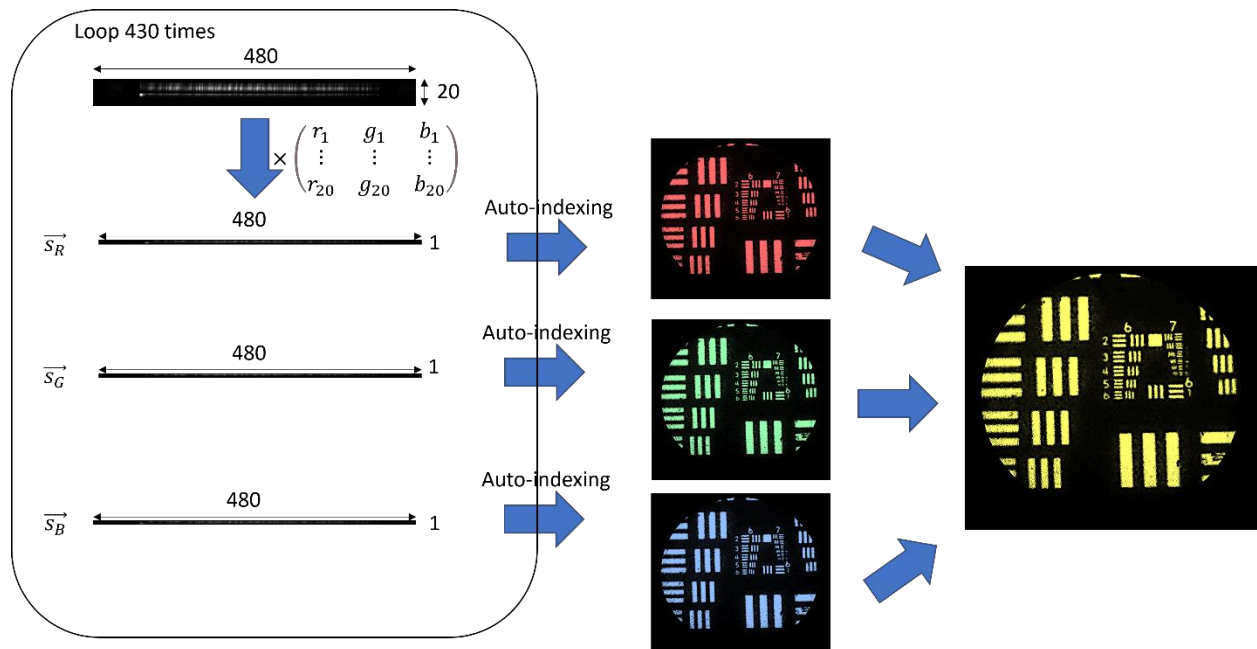


Fig. 3-17. Process to convert spectral information to RGB information by using an RGB weight matrix.

Fig. 3-17 illustrates how the system uses the spectral information and the RGB weight matrix to display an RGB image. First, we need to convert spectral information to RGB information. We multiply the subframe matrix with the RGB weight matrix to get $(\vec{s}_R, \vec{s}_G, \vec{s}_B)$. After that, we output \vec{s}_R, \vec{s}_G and \vec{s}_B separately by auto-indexing for each loop. After 430 loop cycles, we can get the grayscale images of red, green and blue, and then send that data to the LabVIEW RGB display function to get the color image.

3.5.3. RGB Weight Matrix for RGB Filter-style System

So how do we get the RGB weight matrix? It depends on the application. If we want to mimic the performance of an RGB filter-style display, which is used in the benchtop Nikon C1 confocal microscope, then we first need to know how this filter-style system distinguishes colors.

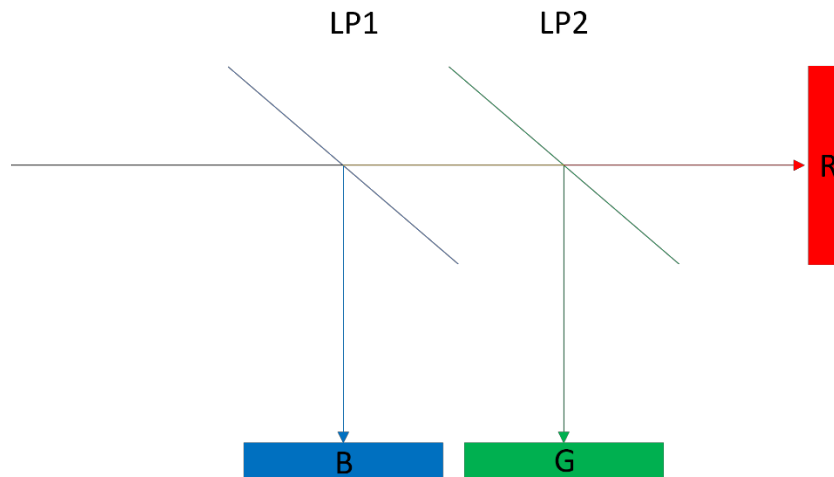


Fig. 3-18. Diagram of typical RGB filter-style display.

Fig. 3-18 shows how an RGB filter-type system differentiates colors. This system consists of two long-pass filters and three grayscale sensors. When light is incident on the first filter, light with wavelengths below the filter threshold is reflected and then detected by the grayscale sensor in the blue channel. Similarly, light with wavelengths below the second filter threshold is

reflected and then detected by the grayscale sensor in the green channel. After that, the rest of the light is detected by the grayscale sensor in the red channel. Afterward, the grayscale image received by the three sensors can be displayed as an RGB image.

The characteristic of this system is that it does not distinguish between the light received by the same sensor, even if they have different wavelengths. For example, if the first filter is a 550nm long pass filter, then this system will not be able to distinguish between two dyes with a spectrum less than 550nm but with different peaks. However, the advantage is that if the filter completely separates the spectrum of the two dyes, this system displays a very high color contrast.

This system has a very straightforward RGB weight matrix, where for wavelengths less than the first filter threshold, they have a blue weight of 1, and the rests are zero. For wavelengths below the second filter threshold, they have a green channel weight of 1, and the blue and red channels are zero. For the remaining wavelengths passing the second filter, they have a red weight of 1, and the rests are zero. For example, if our first filter is between channels 6 and 7, and our second filter is between 13 and 14, then the RGB matrix for these 20 channels is:

$$RGB\ matrix = \begin{cases} r_n = 0; g_n = 0; b_n = 1; n \leq 6 \\ r_n = 0; g_n = 1; b_n = 0; n \leq 13 \\ r_n = 1; g_n = 0; b_n = 0; 20 \geq n \geq 14 \end{cases} \quad (3.5.2)$$

3.5.4. RGB Weight Matrix for CIE Mapping Function

Another way of converting wavelengths to RGB is the CIE mapping method. In chromaticity, CIE 1931 XYZ and RGB color space are the color spaces to be defined mathematically, and it was created by the International Commission on Illumination in 1931.

In RGB mapping, every wavelength has its corresponding chromaticity coordinates, $\bar{r}(\lambda)$, $\bar{g}(\lambda)$ and $\bar{b}(\lambda)$. These three functions were measured in 1920 by W. David Wright and John Guild, and their relationship with wavelength is shown in the Fig. 3-19.

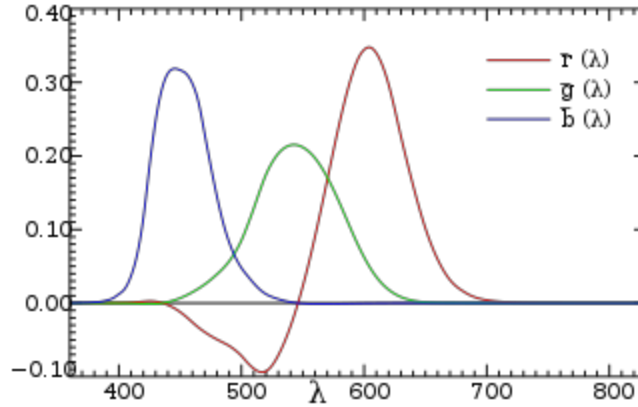


Fig. 3-19. The CIE 1931 RGB color matching functions⁴⁵.

For light consisting of multi wavelengths, its tristimulus values RGB can be expressed by the following equation:

$$\begin{aligned}
 R &= \int_0^{+\infty} L(\lambda) \bar{r}(\lambda) d\lambda = \sum_{i=1}^N L(\lambda_i) \bar{r}(\lambda_i) \Delta\lambda, \\
 G &= \int_0^{+\infty} L(\lambda) \bar{g}(\lambda) d\lambda = \sum_{i=1}^N L(\lambda_i) \bar{g}(\lambda_i) \Delta\lambda, \\
 B &= \int_0^{+\infty} L(\lambda) \bar{b}(\lambda) d\lambda = \sum_{i=1}^N L(\lambda_i) \bar{b}(\lambda_i) \Delta\lambda.
 \end{aligned} \tag{3.5.3}$$

where $L(\lambda)$ is the given spectral input. In the MSCE, $L(\lambda)$ can be represented as the pixel intensity value. For a given subframe matrix, assume $\Delta\lambda = 12.5 \text{ nm}$, its tristimulus values can be calculated:

$$\begin{aligned}
\vec{s}_R &= \sum_{i=1}^{20} \vec{s}_i \bar{r}(\lambda_i) \Delta\lambda, \\
\vec{s}_G &= \sum_{i=1}^{20} \vec{s}_i \bar{g}(\lambda_i) \Delta\lambda, \\
\vec{s}_B &= \sum_{i=1}^{20} \vec{s}_i \bar{b}(\lambda_i) \Delta\lambda.
\end{aligned} \tag{3.5.4}$$

Compared to equation 3.5.1 we find that $(\bar{r}(\lambda_1), \dots, \bar{r}(\lambda_{20})) = (r_1, \dots, r_{20})$, which means the chromaticity coordinates can be directly considered as the RGB weight matrix.

We can also use the CIE XYZ mapping function. It was realized that the RGB mapping method had negative values in the chromaticity coordinates, so another color mapping method was proposed, namely the XYZ method. This method does not have negative chromaticity coordinates (see Fig. 3-20).

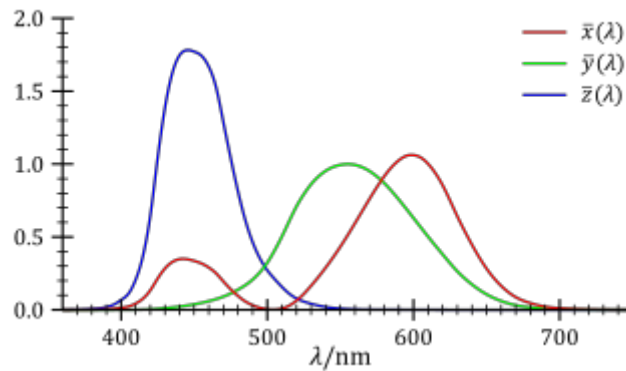


Fig. 3-20. The CIE XYZ color mapping functions⁴⁵.

The XYZ value can also be converted to an RGB value by multiplying it with a constant conversion matrix $T_{XYZ \rightarrow RGB}$. Similarly, the chromaticity coordinates of XYZ can be downloaded

from the CIE website, only we need to change the default display equation in LabVIEW to XYZ display equation when displaying.

I chose to use the RGB mapping function in most cases. It is important to note that although the MSCE system collects the spectrum from 500 nm to 750 nm, this does not mean that we must assign 20 channels to 500 nm to 750 nm. We can adjust the displayed spectrum to allow us to view objects with better color contrast. The advantage of the CIE color mapping method is that it displays the spectrum in a way that more closely matches the human eye's perception, especially for broad-spectrum light sources.

3.5.5. From Spectrum to Spectral Unmixing Color Display

The principle of the spectral unmixing algorithm is described in Chapter 2. The LabVIEW program is not very good at large matrix calculations, so I put the pseudoinverse calculation of sensitivity at the beginning of the program instead of recalculating it in each loop. In this program, the calculation of the spectral unmixing algorithm occurs after each subframe acquisition instead of after 430 subframes to avoid the risk of losing synchronization. The flow of the program is shown in the Fig. 3-21.

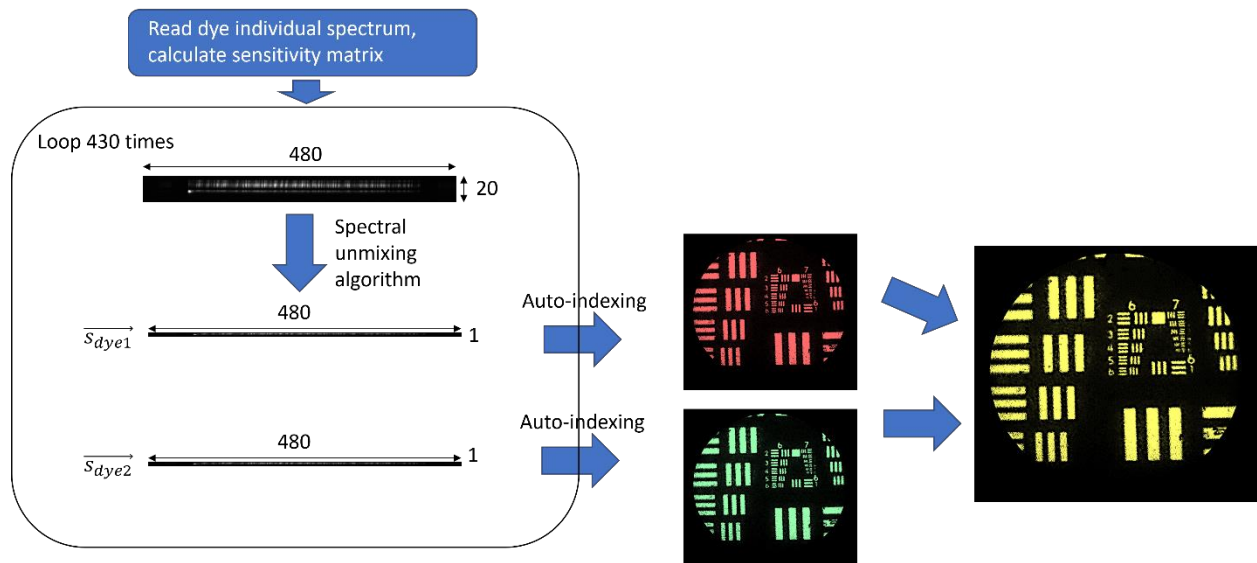


Fig. 3-21. Process to convert spectrum information to RGB information by using the spectral unmixing algorithm.

When the system starts up, the program reads the individual spectrum of each dye from the file filled in by the user and generates the sensitivity matrix. The individual spectrum of the dye will not be updated unless the user clicks the Reload RGB weights button. When the user selects spectral unmixing mode, the program will use the spectral unmixing algorithm on the subframe after each sensor acquisition. Finally, the program will map the signal of each dye to the two pre-selected colors and display them.

Currently the program supports only two colors of spectral unmixing algorithm.

3.5.6. How to Obtain the Spectrum

In the default mode, after each subframe acquisition by the sensor, the program sums the subframe matrix in 430 directions to obtain the spectral distribution of the subframe. After 430 repetitions, the program adds up the spectral distribution obtained each time to obtain the spectral distribution of the entire FOV. The spectral distribution of the entire FOV is obtained and displayed in the second window. The process is illustrated in the Fig. 3-22.

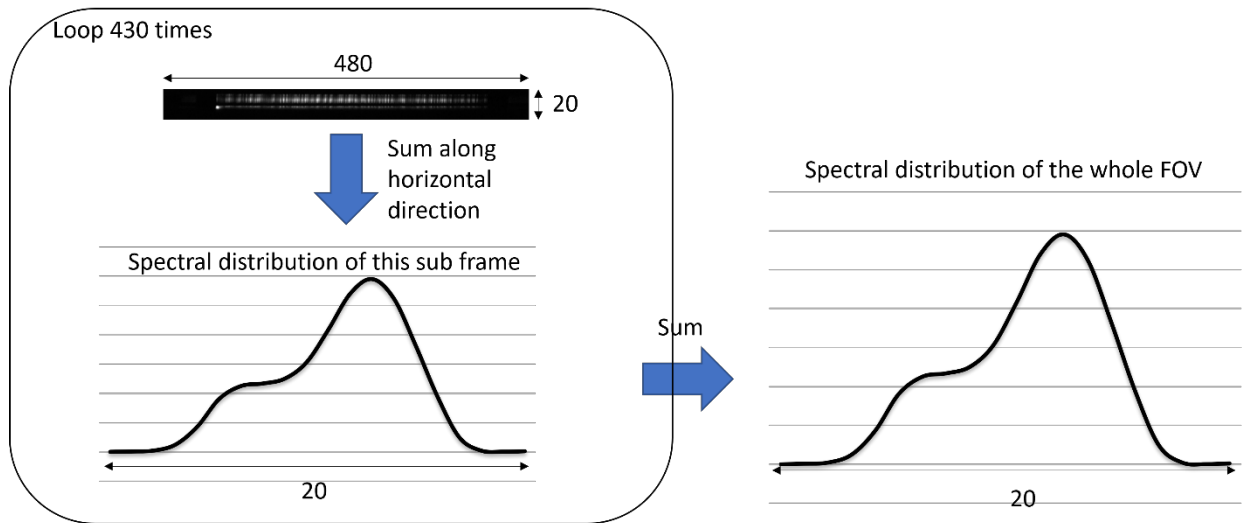


Fig. 3-22. Process to collection of spectral distribution.

We can store the current data by right-clicking on the window of the spectral distribution. By observing an object stained by one dye, we can save its spectral distribution for the spectral unmixing algorithm.

3.6 Remaining Problems and Future Improvements

There are still some potential problems with this program. For example, when a user changes the storage path of a picture or video and starts recording for the first time after starting the program, there is a certain chance that the system will lose synchronization. When the system loses sync, the program does not automatically resume sync unless the user notices and clicks the Align button. In a future update, we may be able to have the Align feature automatically occur when the system loses sync.

The spectral distribution and grayscale windows are deactivated during the recording process to ensure system stability. Only the color window remains active, which makes the system more stable because recording a video can put a lot of computational pressure on the program. It is

hoped that the program will be able to record without suspending the activity of the other windows and maintain the same high robustness in the future.

Also, the system only stores color images when storing images, not raw data of 20 channels. This is also due to the risk of LabVIEW losing synchronization when storing too large a matrix.

Hopefully, this will be solved in the future.

The Spectral unmixing algorithm does not currently consider the effect of noise on the results.

We have not yet found any dye that has a nonlinear spectral distribution, but it is hoped that in the future, the algorithm will be able to cope with the nonlinearity and take the effect of noise into account. In addition, the system currently supports unmixing operations for only two dyes to keep the frame rate high. It is hoped that the system can be modified to support use of more dyes in the future.

Ultimately, a lot of these problems are due to the lack of speed of the LabVIEW software. I hope this system can be written in C or other more efficient language in the future to increase the computing speed and circumvent the above problems.

4 Axial Resolution Test for Fiber-Bundle Based Fluorescence Endomicroscopy

4.1 Introduction

To better understand the actual performance of the endoscope, we need to measure its lateral resolution and axial resolution accurately. The lateral resolution of the MSCE system has been discussed in chapter 2. In this chapter, the methods for measuring axial resolution of the MSCE system will be discussed.

For the benchtop fluorescence microscopes, fluorescent microspheres or fluorescent USAF bar targets can be used for direct measurement. However, different from the general microscope, some endoscopes based on optical fiber probes often need to contact the sample surface. If the microspheres or bar targets are used to measure, the probe will destroy their structure and lead to errors in measurement results. Moreover, many fluorescent USAF bar targets have a minimum working distance, which makes us unable to measure their resolution directly by contacting the bar targets.

In the past, some researchers have used plane mirrors to measure the axial resolution of fiber probe-based endomicroscopy. However, this measurement method has potential problems when it is used in fluorescence imaging. The first is that the excitation source and fluorescence signal of fluorescence imaging have completely different wavelengths, and the wavelength of the excitation source is often much shorter than that of the fluorescence signal, so the results might be inaccurate. The second problem is that the reflection signal from the mirror is not same as the signal scattered from the real object. This will lead to different axial resolutions. So, we need an

appropriate measurement method for fluorescence imaging to measure the axial resolution of MSCE accurately.

4.2 Theoretical Evaluation of Axial Resolution

We simulated the axial resolution as well as the lateral resolution of the MSCE system without a fiber bundle, which is modeled from reference⁵². In the Fig 4-1 we can see the profile of the point spread function and the theoretical axial resolution and lateral resolution of the system.

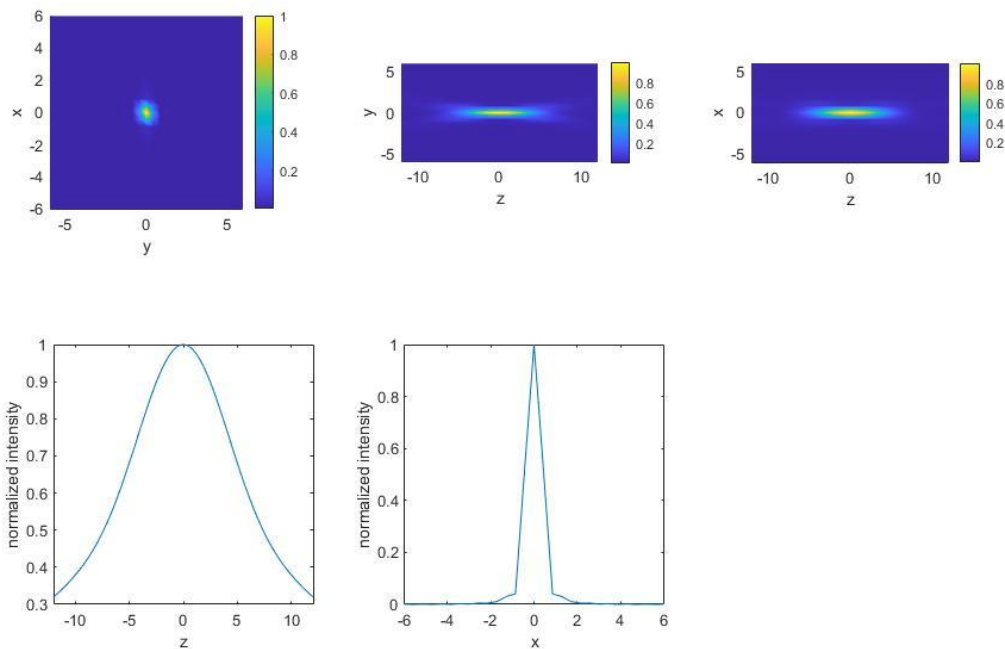


Fig 4-1 Point spread function plots for a line-scanning confocal microscope

In the case of the MSCE system without a fiber bundle, the lateral resolution is 1 to 2 μm . The theoretical axial resolution (FWHM) is 14 μm .

4.3 Axial Resolution Test with Thick Fluorescent Plate

The slanted edge test is widely used in determine lateral resolution in 2D imaging systems. Its main principle is to first measure the image of a slanted edge of a dark to bright transition, then

determine the LSF (line spread function) of the system as the derivative (or model fit) of the slanted edge across the boundary. Finally, if the system is circularly symmetric, the LSF is independent of the angle and is equal to the circularly symmetric PSF (point spread function). By Fourier transformation of the PSF, we can finally obtain the MTF (modulation transfer function) of the system. In this chapter, we use a similar method to measure the axial response of an edge boundary.

The method we have developed is to use a relatively thick fluorescent plate. When we move the plate along the axial (depth) direction, we uniformly collect the overall signal intensity at each depth position to produce the axial edge response, after which a derivative (or model fit) produces a one dimension plane response function. The 1D Fourier transform of the plane response function is the MTF for estimation of the axial resolution.

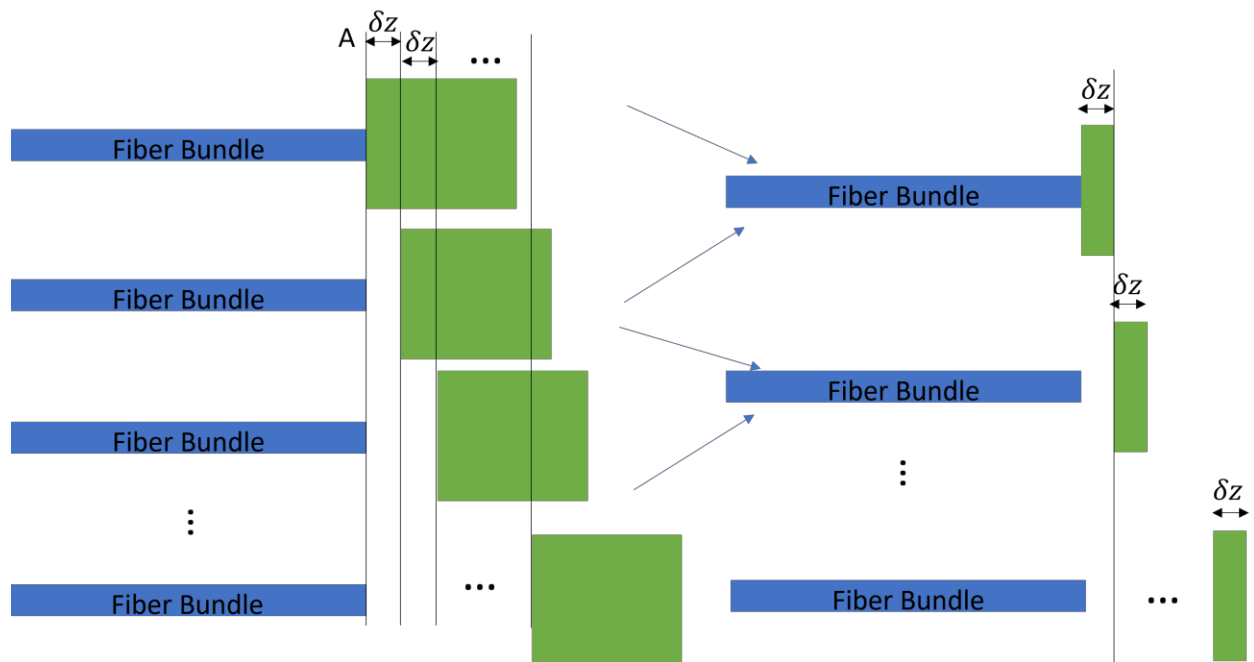


Fig. 4-2. Moving the thick fluorescent slide along axis.

Fig. 4-2 indicates the concept of the axial planer edge test. Suppose we move the fluorescent plate axially at a uniform speed and collect a series of images at equal depth intervals. We can assume the fluorescent plate moves a fixed distance δz backwards each acquisition. Thus, the thick fluorescent plate goes from position A when the fiber is in contact with the fluorescent plate to position $A + \delta z$ for the next measurement. By subtracting the resulting signal, we can get a new signal intensity, δI . By analogy, when this thick fluorescent plate keeps moving backward, and we subtract the signal intensity from each adjacent position, we can get a change in the signal equivalent to what would be obtained with a thin fluorescent plate moving through the volume. The process of moving thin fluorescent plates is the same as the process of measuring axial resolution with a single layer of fluorescent microspheres. However, the minimum thickness of a single layer of microspheres is limited, but by shortening the distance of each movement δz , we can shrink the thickness of this thin fluorescent plate to a very small size, making the result more accurate. When δz is very small, the signal curve collected by the moving thick fluorescent plate is guided, and the result is the axial PSF of the fiber optic probe.

4.4 Axial Resolution Calculation

The overall signal intensity collected by the microscope when the parallel plate is in position z is I . In moving the parallel flat plate within a certain range, we can obtain the relation $I(z)$ with respect to the position. According to the method mentioned before, the derivation of $I(z)$ is the point spread function along axial direction, which is:

$$PSF = \frac{\delta I(z)}{\delta z}$$

If the system is perfect and without consideration of diffraction, $I(z)$ is a step function and the PSF is equal to the delta function.

4.5 Experiment Setup and Test on a Benchtop Confocal Microscope

Fig. 4-3 shows the set up for the test using to a benchtop Nikon confocal microscope. We used both axial edge test and single microsphere test to make sure they produce similar results.

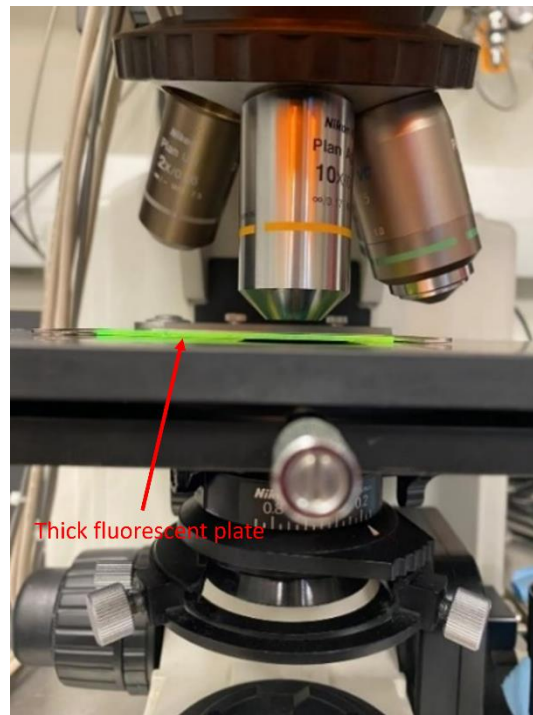


Fig. 4-3. System setup for axial edge test.

A thick (1.27 mm) green fluorescent plastic slide from Chroma was used as the fluorescent edge object. A single $0.5 \mu\text{m}$ diameter green fluorescent microsphere was used for the point spread function measurement. In the single microsphere test, the slide has a movement range of 37 to $87 \mu\text{m}$. In the edge test, the plate has a range of movement from 0 to $180 \mu\text{m}$.

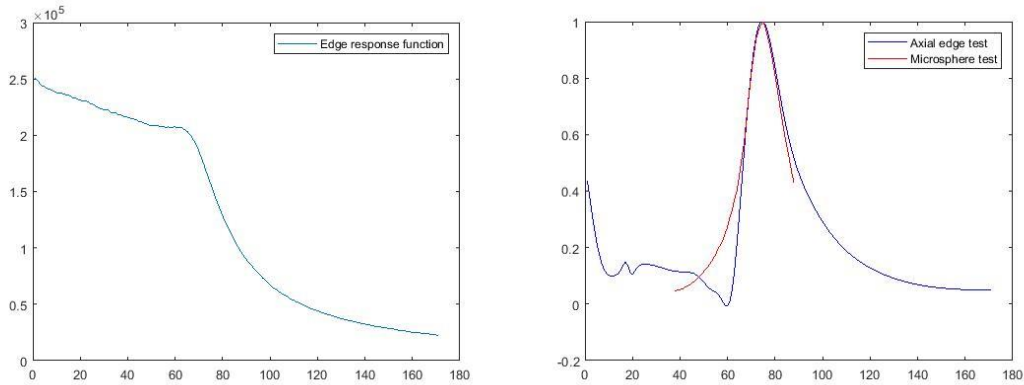


Fig. 4-4. Diagram of Nikon benchtop confocal microscope's edge response function and its axial point spread function. left: edge response function; right: PSF from axial edge test and microsphere test.

Fig. 4-4 shows the measured edge response. By differentiating the fit curve (fit type 'gauss8'), we can get the PSF. In the Fig. on the right, we can see that the PSF obtained by the point test and the PSF obtained in the axial edge test almost coincide, with the PSF of the slide test having an FWHM of 20 microns while the FWHM of the PSF of the edge test is 21 microns. This means that the axial resolution of this microscope is about 20 microns. The results of the two tests are similar.

4.6 Axial Edge Test in the MSCE System

A similar axial edge test is applied in the MSCE system to determine its axial resolution.

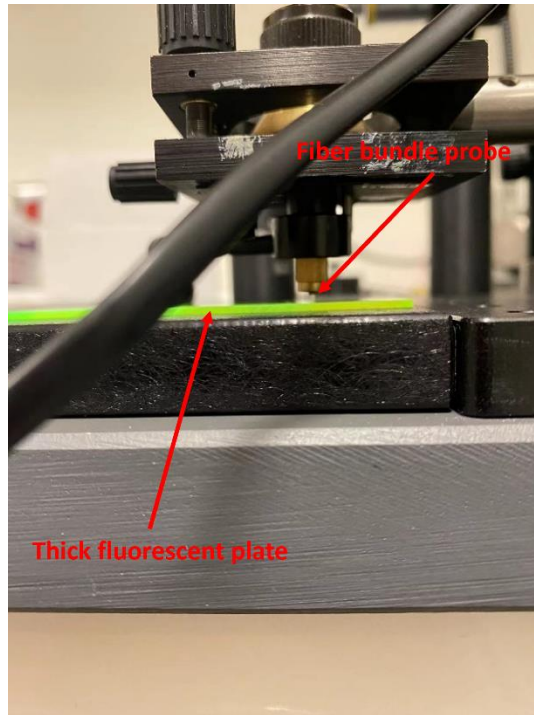


Fig. 4-5. Setup for the axial resolution measurement in the MSCE system.

Fig. 4-5 indicates the setup for axial edge test utilized in the MSCE. The fluorescent slide is the same one used on the Nikon confocal microscope. In this experiment, the piezo control program is also written into the LabVIEW program. When the user starts the video capture, the probe touches the fluorescent plate slightly at the beginning and then is slowly moved away from the fluorescent plate to cover a distance of approximately 150 μm by the piezoelectric translation stage (Newport, 8302). The MSCE system acquires grayscale images sequentially as the fiber bundle moves away from the fluorescent slide. This results in more uniform image acquisition and more accurate measurement accuracy than manual motion control.

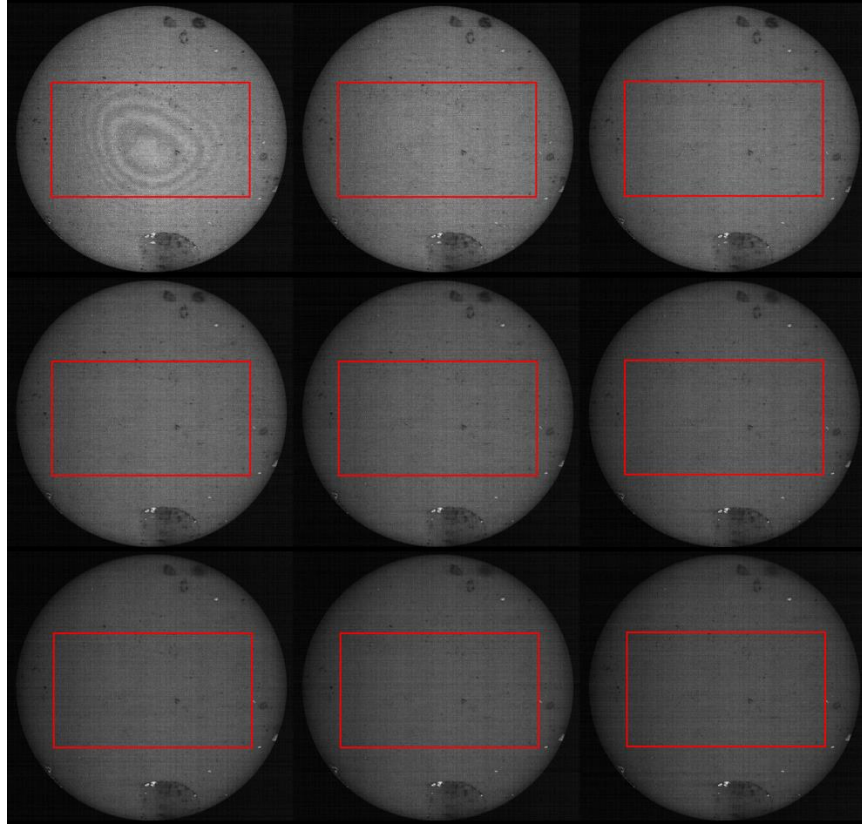


Fig. 4-6. The grayscale images collected by MSCE during this test. Red box: regions of interest that are used to calculate the axial resolution.

Fig. 4-6 shows the initial nine grayscale images collected by the MSCE during the experiment. In the first picture of Fig. 4-6 we can see the interference rings. This fringe pattern is likely due to the fiber bundle polishing, which leaves a slight curved surface on the fiber bundle. There is a specific curvature that leads to interference fringes between the two surfaces. This pattern can actually be useful in helping us adjust the angle between the fiber probe and the fluorescence plate. To ensure the accuracy of the experimental data, we need to keep the fluorescence plate parallel to the fiber bundle, so we need to ensure that the interference circle is in the center of the picture when the plate is in contact with the fiber bundle (i.e., the initial position).

We can see that the first image on the top left with the interference fringes is the brightest. When the probe moves away from contact with the slide there is a gradual reduction in the signal

intensity. As expected, the response peak reaches its maximum when the probe contacts the slide. The interference fringes observed in the first (contact) position show a small gap of a few microns between the fiber and the slide surface.

Fig. 4-7 shows the result obtained from this measurement. For the fit curve, I used a fourth order “polynomial4”. The axial resolution for the fiber bundle based MSCE system is 6 microns, but it is important to note that this only measure the half width outside the fiber.

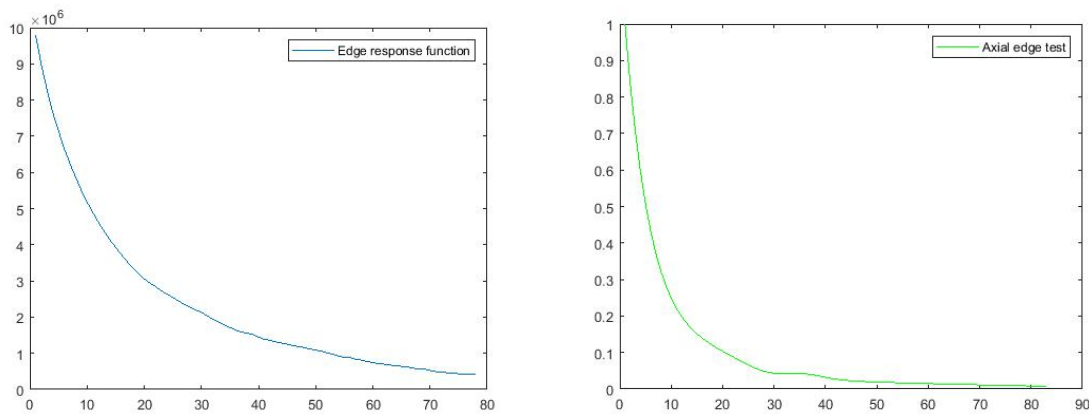


Fig. 4-7. The MSCE edge response function (left) and axial resolution (right).

4.7 Summary

This section presented a method for measuring the axial resolution of fiber optic probe-based fluorescence optical systems. The traditional single fluorescence sphere method for benchtop confocal microscopes has limitations when it is used for fiber-bundle based system. The single fluorescence microsphere method is difficult to use with an in-contact probe system and cannot give accurate reproducible results. So, we adopted the edge method to test the axial resolution of the fluorescence MSCE system.

We first measured the axial resolution of the benchtop confocal microscope using the traditional single fluorescent sphere method and the thick fluorescent plate-based edge test. The

results show that the axial resolutions measured by the two methods are very similar. So we can conclude that the accuracy of the thick fluorescence plate-based edge test method is consistent with the conventional method of measuring the axial resolution of the benchtop confocal microscope. Then we used the thick fluorescence edge method to test the axial resolution (half width half max) of the MSCE system, and we got a result of $7 \mu m$. By comparison, we can see that the axial resolution measured with the fiber bundle is similar to the theoretical axial resolution of system without fiber bundle.

5 Non-mechanical Beam Steering for Fiber

Bundle Depixelization in MSCE

5.1 Introduction

Fiber bundles are widely used as optical relays systems in endoscopic imaging system probes due to their ease of replacement and flexibility. In some endoscopic imaging systems, the distal end of a bare fiber bundle is placed in contact with the surface of the object and collects the light signal emitted from it. It should be noted that fiber bundles cannot transmit the complete phase and polarization information of the entering light to the other end of the fiber. Another limitation is the significant energy loss compared to normal optical imaging devices (i.e. lenses). In addition, for endoscopic systems that use a fiber bundle as a relay, the problem of pixelization caused by the fiber bundle structure has been a drawback.

Pixelization refers to an image sampling problem of fiber bundles. As shown in the Fig. 5-1, when we look at an object with a fiber bundle relay, the image of the object seems to be covered with a honeycomb intensity pattern, and the spatial resolution of the whole image is reduced. Not only that, but smooth straight lines will be distorted. This means that pixelization not only reduces the resolution of the fiber bundle, but also provides the observer with false information by distorting and aliasing the object.

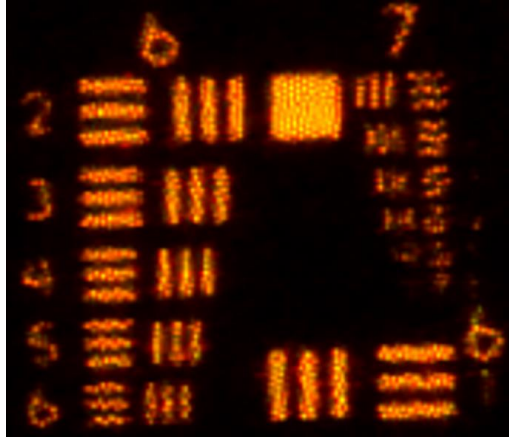


Fig. 5-1. Image of a USAF bar target with pixelization problem.

Pixelization phenomenon originates from the production process of the fiber bundle. Since the fiber bundle does not transmit light in cladding, the overall sampling frequency of the fiber bundle is lower than when the fibers are closely aligned.

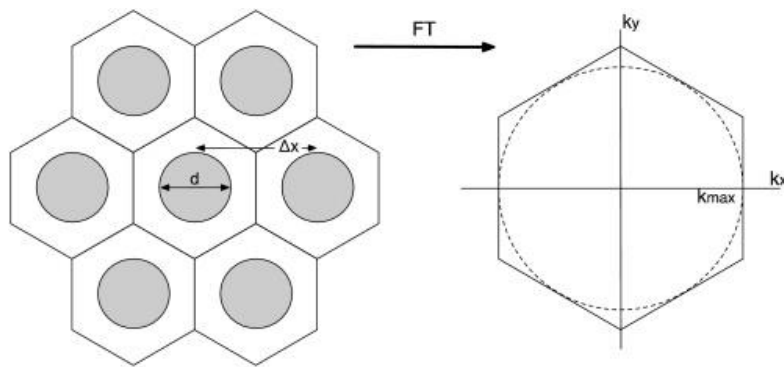


Fig. 5-2. Geometry of a hexagonally packed array of optical fibers⁴⁶.

The left image of Fig. 5-2 shows the idealized hexagonally packed structure of the individualized fibers in a fiber bundle. The individual fiber cores are shown as the gray circles. Assume the distance between two cores is Δx , we have the sampling frequency of this fiber bundle:

$$k = \frac{1}{\Delta x} \quad (5.1.1)$$

And in the horizontal direction, the maximum unaliased spatial frequency is

$$k_{max} = \frac{1}{2\Delta x} \quad (5.1.2)$$

Similarly, we can obtain the sampling frequency in the oblique and vertical directions to obtain the sampling pattern of the fiber bundle in the spatial frequency domain (see right image of Fig. 5-2).

5.2 Previous Work

Some previous work on improving image quality in fiber bundle imaging systems has been done by Carlos's group⁵¹. In this work, instead of moving the ends of the fiber bundle laterally, they rotate the distal end of the fiber bundle and introduce post-image processing algorithms to remove the pixelization.

Another technique to remove pixelization has been described by Dr. Tkaczyk and his team⁴⁷. Instead of using a mechanical method to move or rotate the fiber bundle, a dispersion technique is introduced to increase the sampling frequency. With known spectral distribution, or an object stained by one fluorescent contrast agent, this method can depixelize the image with one snapshot. We built a demo with a similar technique to this work, which will be discussed in the following sections.

Some other previous work on improving image quality in fiber bundle imaging systems has been done in Dr. Gmitro's Lab⁴⁶. In this work, the authors connect both ends of the fiber bundle to piezoelectric devices that can move both ends of the fiber in two dimensions, allowing the probe to collect signals that would otherwise not be collected. In essence this approach increases the inherent sampling frequency and improves the spatial resolution of the fiber bundle imaging system.

This method has the following advantages: 1) since this device is used to increase the sampling frequency by mechanical movement, it does not change the optical characteristics of the signal, and 2) piezoelectric devices are commercially available, making the whole system easier to produce. This method has the following disadvantages: 1) the movement of the two ends of the piezoelectric device is difficult to exactly synchronize, because piezoelectric devices have some variability in the movement they produce for a given applied voltage; 2) the fiber fits through the center of the cylindrical piezoelectric device, which leads to a larger diameter probe head; and 3) when the probe directly contact the object, the piezoelectric device may force undesired movement in the object rather than pure movement of the fiber probe over a static object.

To solve the problem of error due to the differences in physical movement produced by the two piezoelectric devices on either end of the fiber, we decided to replace the proximal end piezoelectric device with a software approach that seeks to estimate the motion difference at the proximal end of the fiber as the distal end of the fiber moves due to the distal end piezoelectric.

5.3 Cross-correlation Method

This software approach uses a 2D cross-correlation to estimate the 2D shift of the image at the proximal end of the fiber bundle. The cross-correlation function is most often used in signal processing, where it describes the degree of similarity between two signals. For two functions $f_1(x, y)$ and $f_2(x, y)$, the cross-correlation function is defined as:

$$R_{12}(x, y) = \int_{-\infty}^{+\infty} dy' \int_{-\infty}^{+\infty} f_1(x', y') f_2(x' + x, y' + y) dx' \quad (5.3.1)$$

it can also be written as:

$$R_{12}(x, y) = f_1(x, y) ** f_2(-x, -y) \quad (5.3.2)$$

where the ** notation indicates a two dimensional convolution operation. When two images are so similar that there is almost only a displacement offset, then their relationship can be written as

$$f_1(x, y) = f_2(x - \Delta x, y - \Delta y) \quad (5.3.3)$$

The relationship between their Fourier transforms are:

$$F_1(u, v) = F_2(u, v)e^{-2\pi i\Delta x}e^{-2\pi i\Delta y} \quad (5.3.4)$$

Then their cross-correlation function is:

$$\begin{aligned} R_{12}(x, y) &= F^{-1}\{[F(R_{12}(x, y))]\} = F^{-1}\{F_2(u, v)F_2(u, v)e^{-2\pi i\Delta x}e^{-2\pi i\Delta y}\} \\ &= A_{12}(x, y) ** \delta(x - \Delta x, y - \Delta y) \end{aligned} \quad (5.5.5)$$

where $A_{12}(x, y)$ is the autocorrelation function of $f_1(x, y)$. And the peak of the autocorrelation function is at the position where the argument of the delta function is zero. By observing the peak position of the cross-correlation function, the displacement offset between the two pictures can be derived. After that we can introduce opposite offsets to shift one of the images, which completes the work of the piezoelectric device at the proximal end that is no longer used and combines the images (with and without lateral shift) to get a new image with a higher sampling frequency. There are two ways to combine the images: one is called max intensity projection (MIP) and the other is to average the signal intensity of the two images. These two methods will be compared in detail later in this section.

To get displacement offset more accurately, we need to introduce a gaussian blur to both images first, then use the cross-correlation function method to estimate the shift in the blurred images.

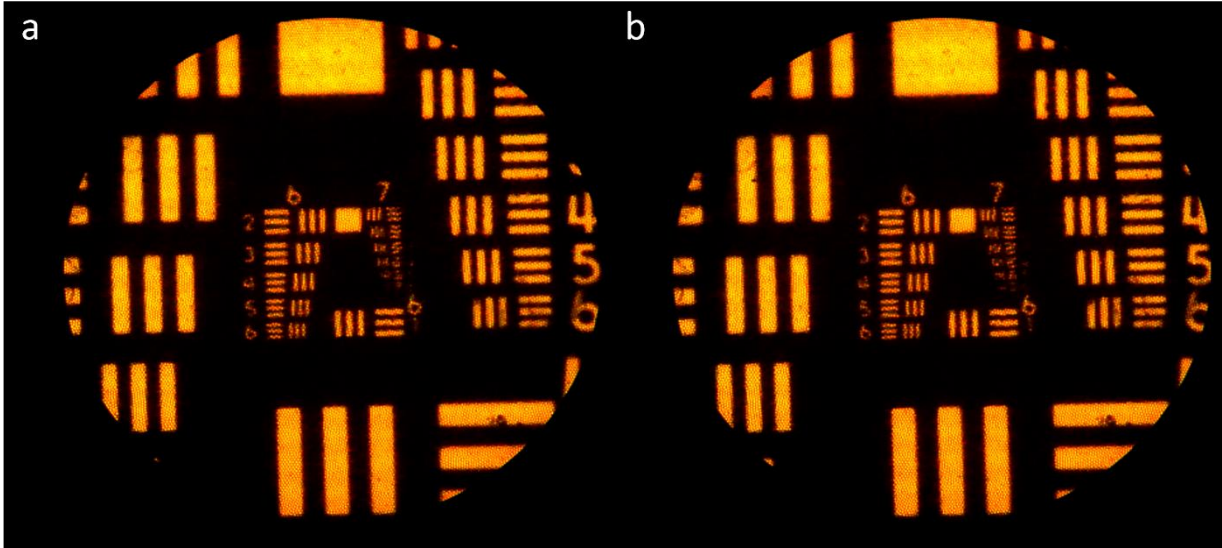


Fig. 5-3. Images collected before and after probe's movement.

As shown in the Fig. 5-3, we can acquire two similar images before and after the distal end probe movement, apply a Gaussian blur to the all images, then use the cross correlation method to calculate the offset distances, and then use the MIP method or average method to process the combination of the images, the results are shown in the Fig. 5-4.

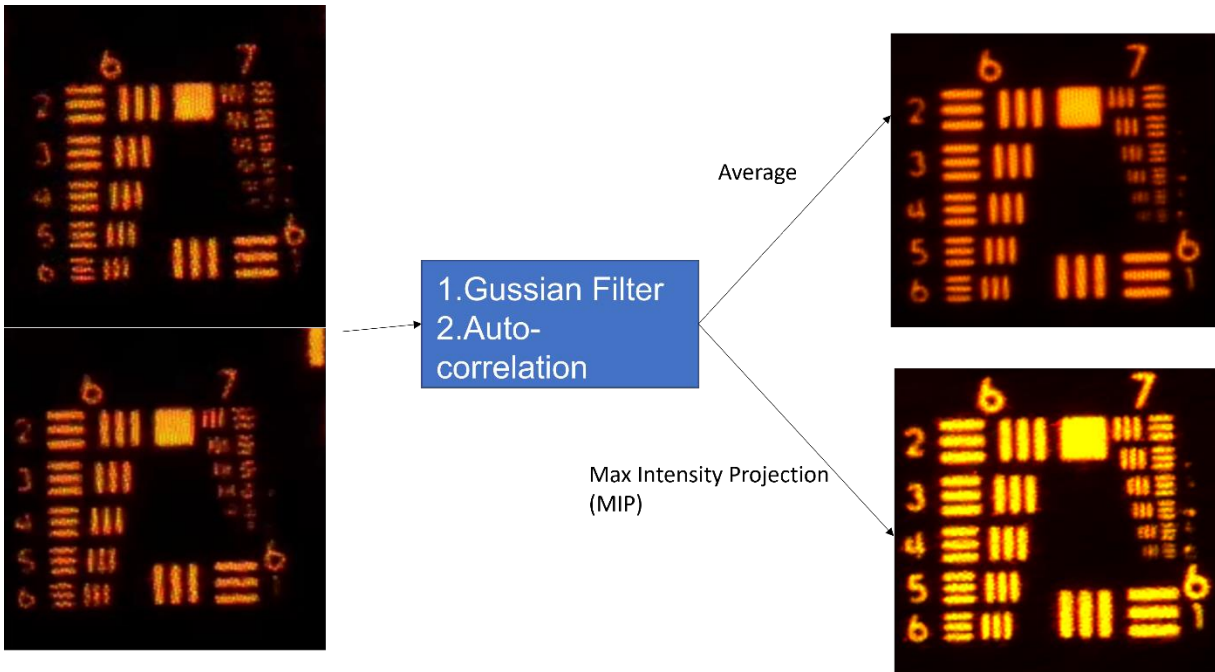


Fig. 5-4. Using average method and MIP method to remove pixelization problem.

We can see that the MIP plot has higher brightness, but each line looks thicker. The average method gives a lower brightness but slightly higher resolution.

5.4 Non-mechanical beam steering method

The above cross-correlation method still has disadvantages because it still uses mechanical movement to increase the sampling frequency. When the probe directly touches the tissue's surface inside the body, it is not a good idea to move the probe. So we have to find a way to increase the sampling frequency without moving the probe. Beam steering is one of the solutions, it can be changed by changing the optical path to make the object appear to have movement with the probe. The most traditional mechanical beam steering is to place a scanning mirror in the collimated space and rotate the beam by the movement of the scanning mirror, as shown in the Fig. 5-5.

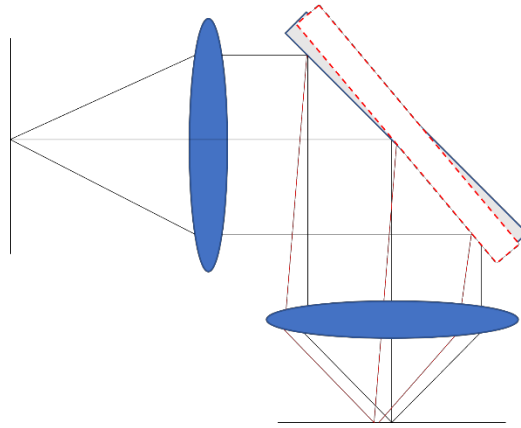


Fig. 5-5. Use of a scanning mirror to steer beam offset.

Although this design avoids the movement of the probe on the object, the probe will not be able to enter the biopsy needle because the head needs to be bent. Moreover, placing a scanning mirror at the end of the fiber bundle may cause the probe to vibrate and not be able to acquire images stably. Therefore, we need to find another non-mechanical beam steering method.

By looking at the scanning beam steering system we can find that as long as the mirror becomes a transmissive optical element and the change element can adjust the optical path without mechanical movement, it can meet our needs. We have identified two methods of beam steering that can achieve non-mechanical motion. One is an electronically controlled LC prism, and the other is a normal dispersive prism.

5.4.1. Liquid Crystal Prism

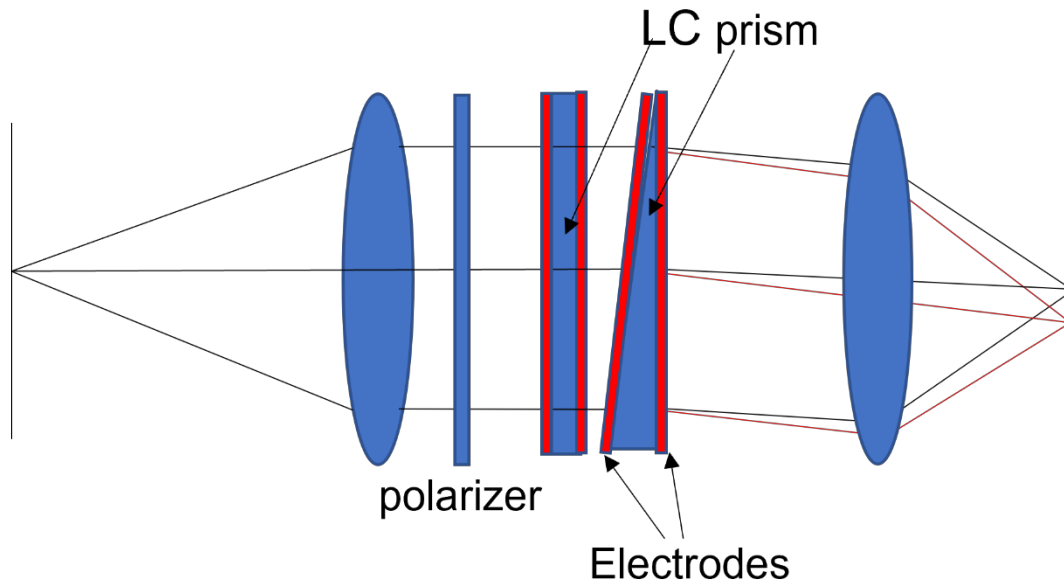


Fig. 5-6. Non-mechanical beam steering with two LC prisms.

Liquid crystal devices are widely used in displays and optical path modulators. We can adjust the refractive index of its eigenpolarization state in this material by changing the voltage at both ends of the liquid crystal to adjust the orientation of the liquid crystal cell. Therefore, we can also use it to replace the scanning mirror in the above section. As shown in Fig. 5-6, we insert a polarizer in the collimated space. Then we add two staggered LC prisms after the polarizer. The first one is used to modulate the deviating angle in the x-direction, and the second one modulates the deviating angle in the y-direction. We can achieve the effect similar to mechanical scanning by adjusting the voltage on the liquid crystal devices.

The advantage of this approach is that the whole process does not require any mechanical movement, and the whole optical system remains rotationally symmetric and can potentially be made small enough fit through a biopsy needle. The disadvantage of this method is that the light intensity will be only half of the original one due to the presence of the polarizer, and the

transmission efficiency and deflection efficiency of the liquid crystal will be different for different wavelengths. In terms of production, the smallest liquid crystal pixel on the market has reached the micron level, so there is a theoretical possibility of producing LC prisms of about one millimeter. However, we did not have the opportunity to demonstrate this device.

5.4.2. Disperse Prism with Known Spectrum

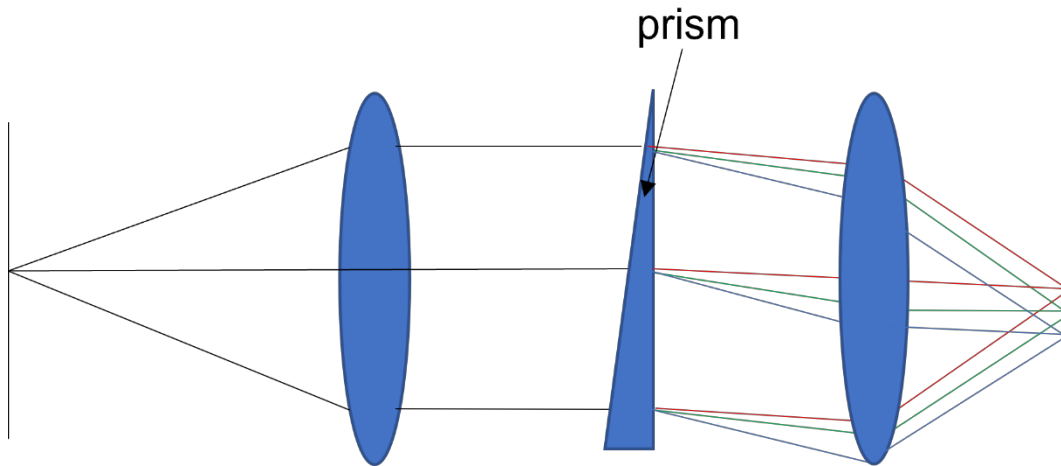


Fig. 5-7. Non-mechanical beam steering with prism.

The second method replaces the LC prism above with a dispersive prism, as shown in the Fig. 5-7, but requires that the spectral range of the object be known. A similar approach has been done with back illumination and one fluorescent dye⁴⁷. In the MSCE, we need to use epi-illumination and multiple dyes. Currently, we only use two fluorescent dyes, so we can quickly know their spectral ranges. In the MSCE, we can project different colors onto different channels, and different spectral now also correspond to different object positions.

The second method replaces the LC prism above with a dispersive prism, as shown in the Fig. 5-7, but requires that the spectral range of the object be known. This project uses only two known fluorescent dyes, and we can easily measure their spectral distributions. Furthermore, in the MSCE, we can project different colors onto different channels, and because of the dispersive

prism here, different colors correspond to different object positions. So at this point, our channels represent the color and the position. We can introduce a displacement offset for each channel with the position information to eliminate pixelization in one direction.

Since we were not in a position to produce lenses and prisms with diameters smaller than 1 mm, and we did not find a suitable commercial provider, we built a large prototype with broadband light illumination to test the effectiveness of this method.

5.5 Performance

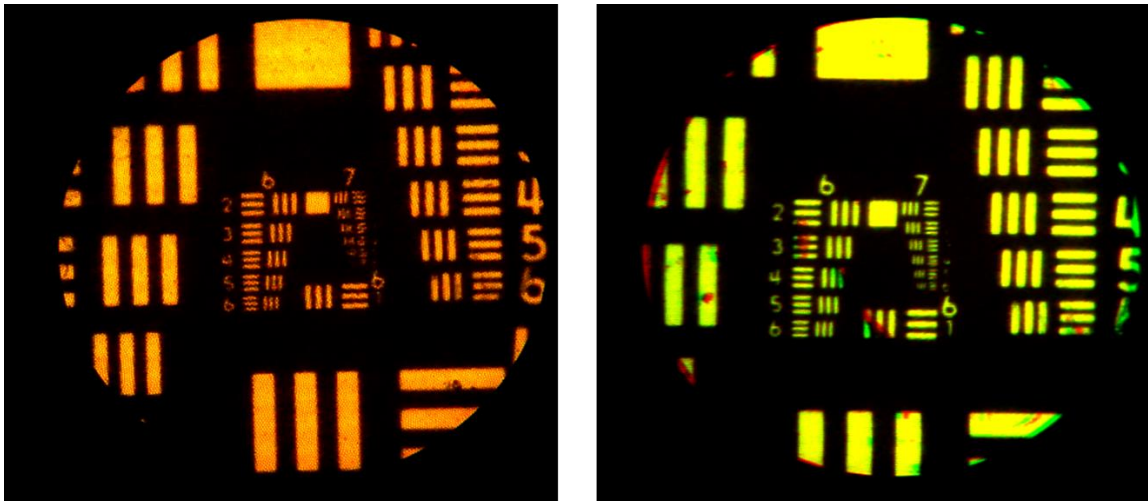


Fig. 5-8. The original image of a bar target acquired by through the fiber bundle (left image) and the image after depixelization (right image).

The Fig. 5-8 shows the original image acquired through the fiber bundle and the image after depixelization. In the original image, the smallest visible element is about group 7 element 2, while in the image after depixelization, the smallest visible element is group 7 element 4, so the resolution is improved. In addition, the image distortion caused by pixelization is well corrected in the right image, which proves that this method is feasible.

Although we succeeded in reducing the pixelization problem, we also found many disadvantages of this method during the experiment. First, this method cannot be used for

imaging objects with an unknown spectrum. Second, the dispersive element will also disperse the excitation light signal when it disperses the fluorescence signal, so if we use this method in both x and y directions, it will make the original linear illumination wider and lead to the degradation of the confocal property. If we use this method only in the direction along with the linear illumination, then the correction of pixelization will be reduced. Third, due to the difference between the excitation light bandwidth and fluorescence bandwidth, the correction effect on the excitation light will be worse than that on the fluorescence signal.

Therefore this method still needs to be improved.

5.6 Summary

This section discusses some methods to eliminate fiber bundle pixelization and concludes with a prototype to demonstrate the feasibility of one of these methods. All methods considered have advantages and disadvantages. Mechanical beam steering can accomplish depixelization without changing the optical properties, but the mechanical motion leads to errors in depixelization and the structure is difficult to place in biopsies or other tiny environments. The LC prism method can achieve depixelization without mechanical motion, but it requires the polarization of the light and will weaken the signal strength. The dispersive prism method can only be applied to a known spectrum but is not as perfect as the first two methods in terms of depixelization performance.

6 Results from MSCE

This section will show some of the image results we obtained during the project. In the first subsection, I show some of the images that we obtained at the beginning of the project. These images were taken from paper, and we used them as samples to test the imaging of the system using different markers and dyes as stains.

In the second subsection, I show some images that we obtained in the middle of the project. During this time, to test the staining effect of different dyes in biological samples, we used rat lung samples, as well as whole intact rat lungs to observe the staining effect of different dyes on the surface of the lungs and inside the lungs.

The third and fourth subsections contain the results obtained later in the project. We show images taken from animal experiments and ex vivo human samples. To simulate a real clinical biopsy, we have used the dye delivery system designed in the previous section for the animal experiments, and the images and video quality will be very close to expect to achieve in the real clinical situation of lung biopsy procedures. We also simulated the process of moving the fiber optic probe to obtain images at different locations and depths during a clinical procedure. In these experiments, all images were obtained from normal healthy mice or rats. Since we do not have access to healthy human lung samples for clinical purposes, lung samples from rats were used as healthy samples for control purposes. Although we did not get healthy human lung samples, we selected human lung samples with different tissue types including necrotic, inflamed, or cancerous tissues. Preliminary results indicate that with our system clinicians can distinguish between the different lesion types.

6.1 MSCE test with Paper Tissue

To test the MSCE imaging system, we first applied fluorescent markers of different colors to paper. The advantage of using paper stained with fluorescent marks is that it is simple and readily available. Paper fibers also provide good visible contrast, making it easy to evaluate image quality.

It should be noted that the color displayed is not the actual color of the markers, we just mapped their spectrum into our preferred RGB color space to make it easier to distinguish. In general, we prefer to display the different color dyes directly in solid colors of blue, green, and red, because the response wavelength peaks of the three types of cone cells in the human eye correspond to these three colors. And the human eyes are more sensitive to green and red. Therefore, in this chapter, we will show the dye as red and green in most cases.

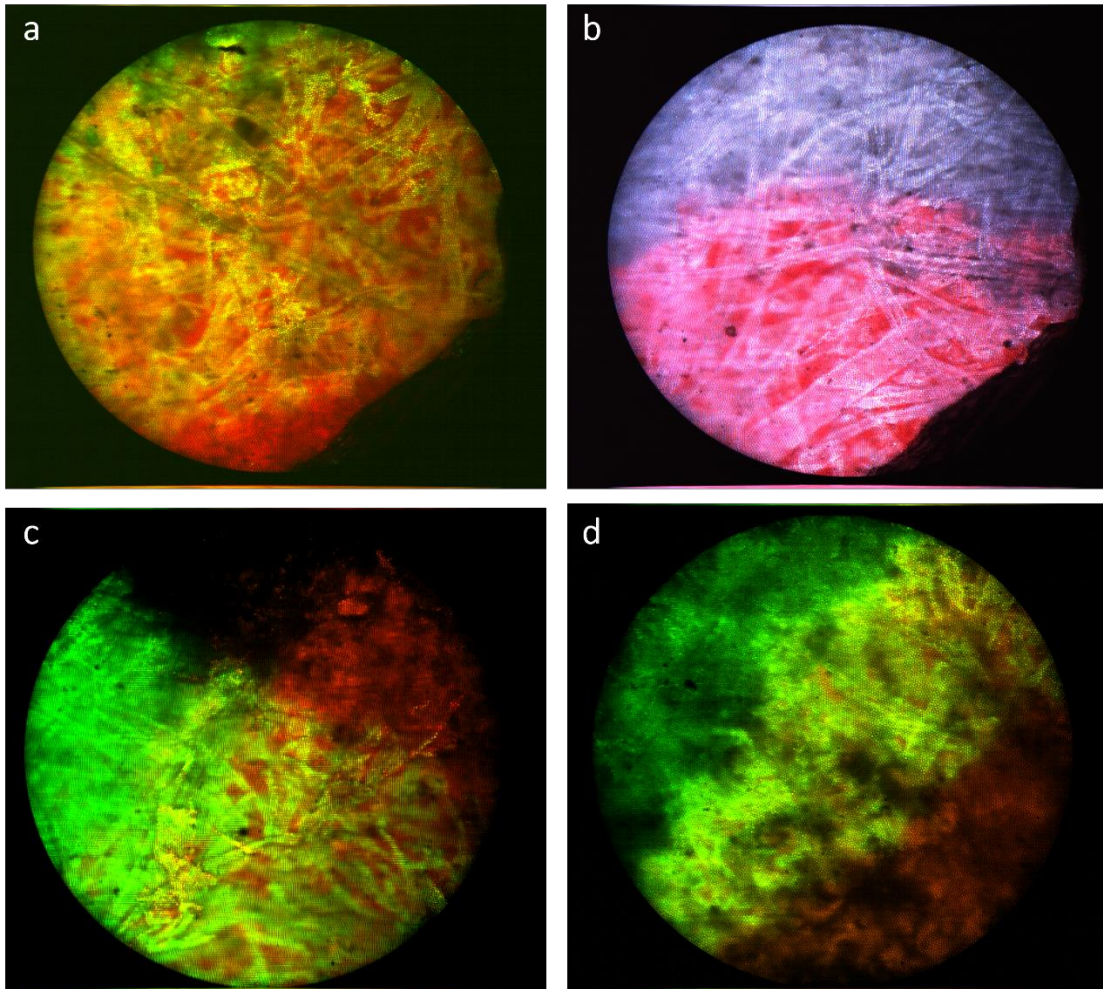


Fig. 6-1. MSCE images obtained from stained paper samples.

Fig. 6-1 shows four images we obtained from stained paper. In Fig. 6-1a, we can see that the two markers have different staining characteristics, with the green color in the Fig. 6-1. marks the fiber's structure, while the red color stains the entire plane more uniformly. In Fig. 6-1b, we moved the probe to the border and tried to change the display colors. We used pink and mauve this time, and the color differentiation is not as pronounced, as the human eye is more sensitive to the difference between red and green. Fig. 6-1c shows the presence of two dyed areas, and an un-dyed area at the top appears black. Fig. 6-1d is also taken from the area where the two stains

meet. Comparing Fig. 6-1c, we can see that the system can work for pure colors and mixed colors properly, and that the system's imaging quality and staining quality are stable.



Fig. 6-2. Image obtained from a business card.

Then we changed the sample from plain paper to a business card. The material of these business cards is fluorescent and therefore does not require application of any dye. Fig. 6-2 is taken from an undyed business card. We moved the probe to an area where the letters were printed in dark ink. This time we used a display color that was determined by the CIE mapping function. The color in the picture is therefore very close to the real color of the business card, with the letters appearing in dark blue and the paper background in yellow. This test proves that the system can display objects close to their true colors.

6.2 Mouse Ex-vivo Lung Tissue Imaging and Dye Combination Testing

Although there are not many FDA-approved dyes, we still need to select the most suitable combination of these options to stain human lung samples. The dyes in this combination need to have different staining properties; for example, one dye tends to stain cell nuclei and the other tends to stain proteinaceous tissue. Even though we have the help of the spectral unmixing algorithm, we still require that the dyes in the combination have different fluorescence emission spectra. Ideally, these dyes should also have different excitation wavelengths, to be able to control the intensity of the light emitted by them using different laser sources.

6.2.1. Fluorescein and Methylene Blue

The first combination of dyes we tested was fluorescein and methylene blue, where fluorescein mainly stains proteinaceous connective tissue and can be used to observe lung structures, such as alveoli, while methylene blue mainly stains DNA and is used to identify the nucleus and cell distribution. The fluorescence emission wavelength peak of Fluorescein is around 525 nm, while methylene blue mainly stains DNA and its fluorescence emission wavelength peak is around 686 nm. Fluorescein is a widely used fluorescent marker that is safe and readily available and has a very high signal intensity and very fast staining. Methylene blue is used in its injectable solution for the treatment of methemoglobinemia because of its reducing properties⁴⁸. The advantage of this combination is that the fluorescence emission wavelengths of the two dyes are very different, basically, there is no overlap, and the excitation wavelengths of the two dyes are different, so the intensity of the excitation light can be used to control the fluorescence emission intensity. The disadvantage is that fluorescein is a very common dye that stains connective tissue and the nucleus. In contrast, methylene blue as a nuclear stain is not particularly fast or efficient compared to other nuclear stains, as will be explained later in this section.

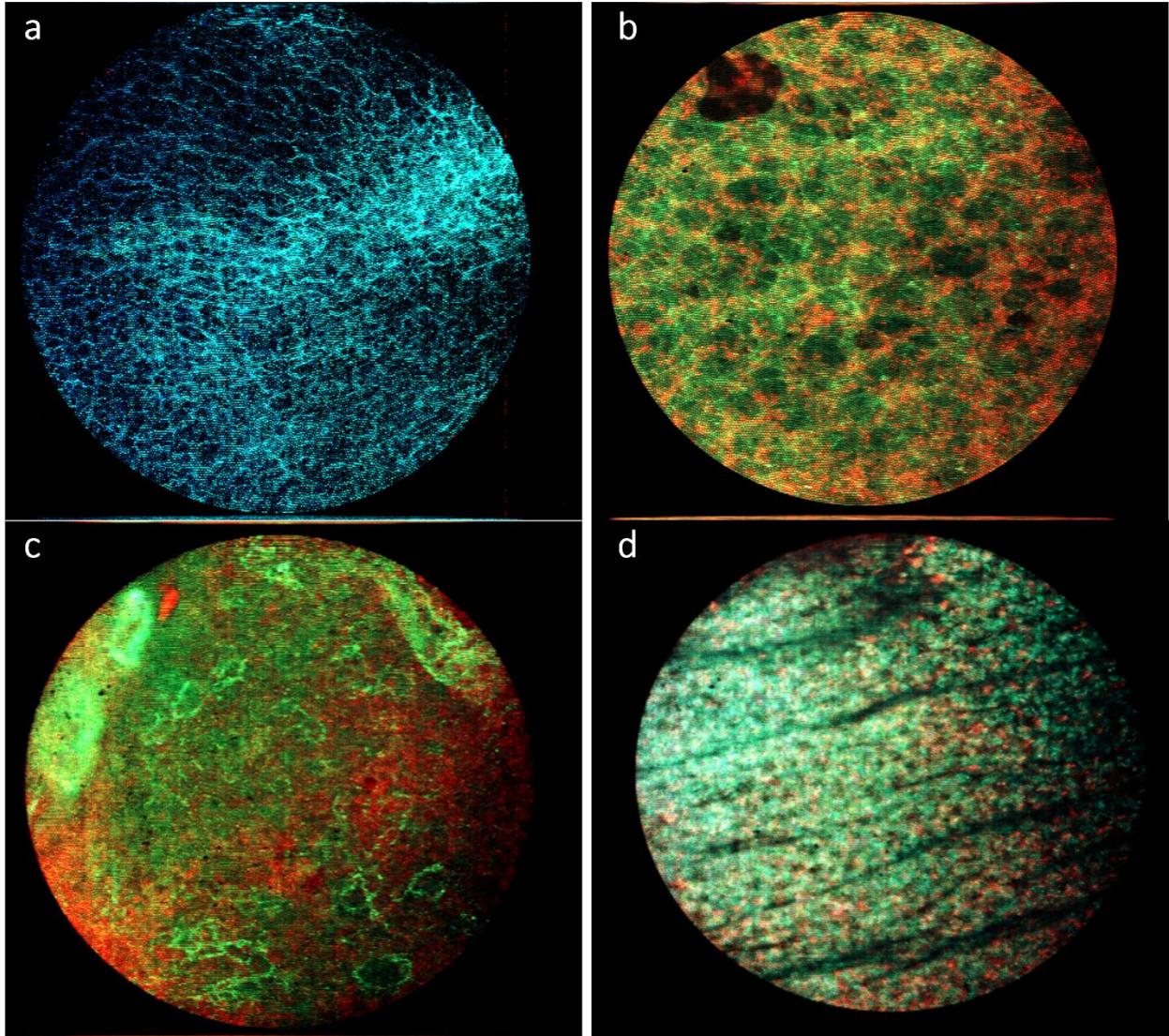


Fig. 6-3. Images collected from the mouse tissue stained by fluorescein and methylene blue.

Fig. 6-3 is taken from a mouse lung tissue sample. Fig. 6-3a uses fluorescein and methylene blue with similar concentrations, and we can see that although fluorescein identifies the lung structure, we can not see any cell nuclei. After adjusting the concentration and laser intensities in Fig. 6-3b we can see that the green connective tissue is obvious, and the alveolar structure of normal tissue is readily observed. We can see the different features of the tissue are marked by methylene blue (red color in Fig. 6-3b). However, the distribution of nuclei is less than we expected from normal mouse tissue sample, and the nuclei do not appear isolated. Similarly, in

Fig. 6-3c and d, the distribution of nuclei marked by methylene blue do not look like isolated nuclei. The fluorescein in Fig. 6-3d is more bluish because we were trying to adjust color mapping function.

6.2.2. Phloxine B and Mitoxantrone

The second combination of dyes we investigated was phloxine B and mitoxantrone. Phloxine B mainly stains connective tissue and its fluorescence emission wavelength peak is around 550 nm, while mitoxantrone mainly stains DNA and its fluorescence emission wavelength peak is around 660 nm. Phloxine B is used commercially as a food coloring⁴⁹, while mitoxantrone is a chemotherapeutic agent used to treat a variety of cancers⁵⁰. Similar to the previous combination, the advantage of this combination is that the fluorescence emission wavelengths of the dyes are very different and the excitation wavelengths are different as well. Unlike the previous combination of fluorescein and methylene blue, the staining speed of phloxine B is slower than that of fluorescein and the signal intensity of phloxine B is considerably weaker than fluorescein for the same concentration. Phloxine B mainly stains proteinaceous connective tissue, whereas fluorescein stains protein more broadly. The staining speed of mitoxantrone is faster than methylene blue and the signal intensity is stronger. The main problem with mitoxantrone is that it is cytotoxic so there is more concern about patient safety.

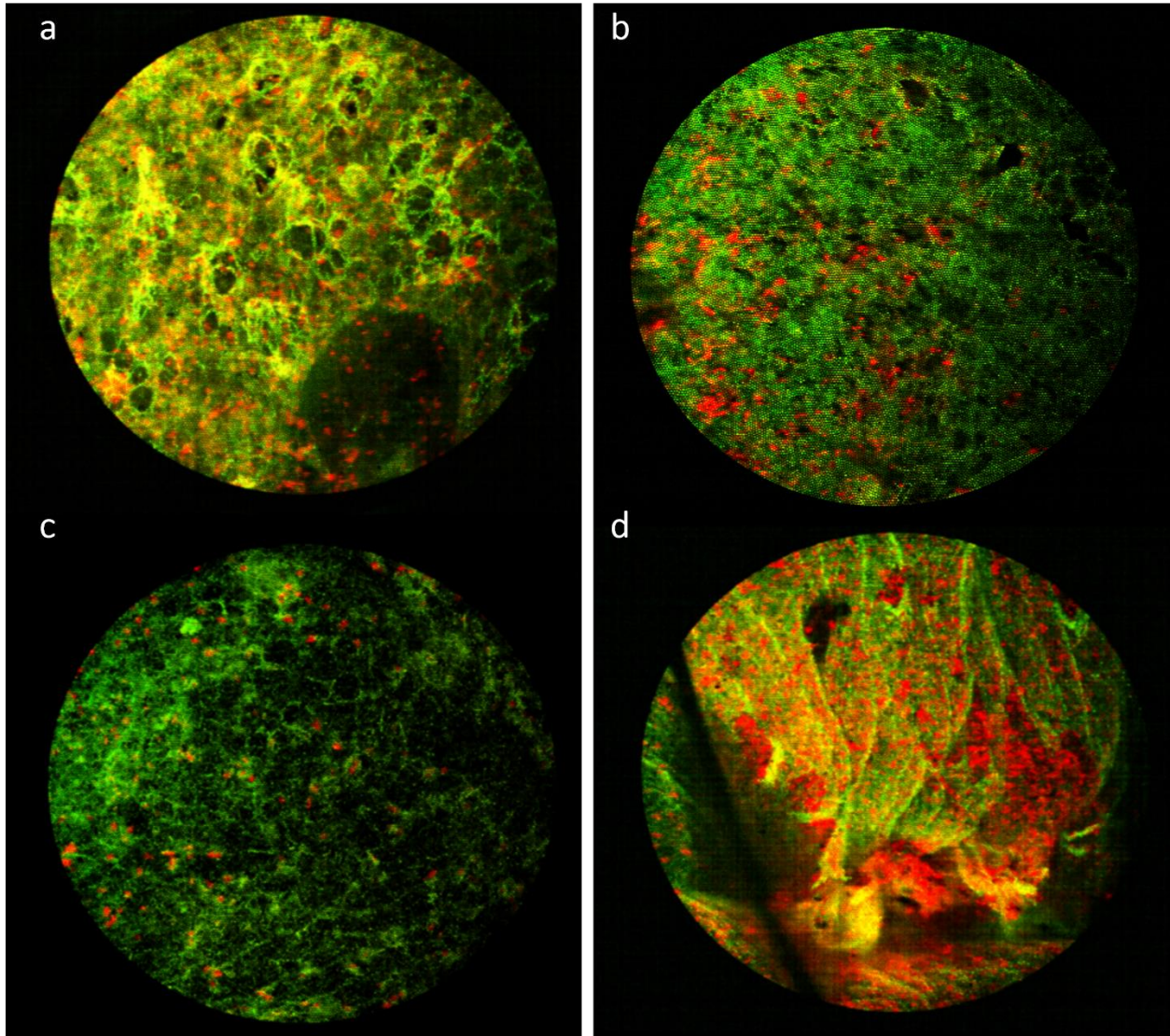


Fig. 6-4. Images collected from the mouse tissue stained by phloxine B and mitoxantrone.

As shown in Fig. 6-4a, 6-4b, and 6-4c, phloxine B (green signal) is very good at staining the connective tissue surrounding alveoli. The staining for these three example images was topically administered to a cut surface of mouse lung. The tissue sample used in Fig. 6-4d is from a mouse lung that was perfused with phloxine B and mitoxantrone delivered into the pulmonary artery shortly after the animal was euthanized. The image in Fig. 6-4d was obtained after we inserted the fiber bundle probe into the stained mouse lung. In this case we can see a bit of trauma caused by insertion of the probe. However, we notice that the staining effect of mitoxantrone is

somewhat strange in this Fig. 6-4d and does not look like the staining of individual cells. Rather it looks like the mitoxantrone is pooling after insertion of the probe possibly because the dye distribution is primarily in the vasculature before that vasculature is disrupted by the probe.

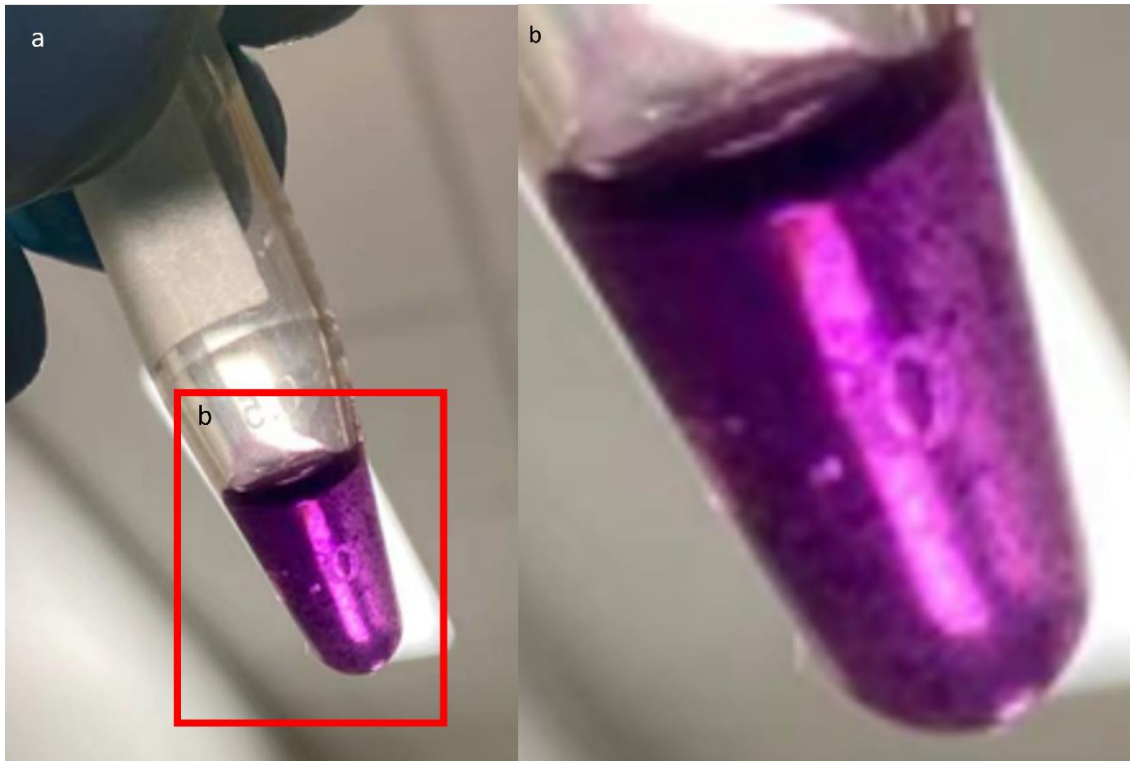


Fig. 6-5. Solution of mitoxantrone and phloxine B were found to precipitate.

A significant finding with this dye combination was that when made as a solution of the two dyes at 100 μ M each we found that a solid, purple-colored substance precipitated out the solution in about 10 mins, as shown in Fig. 6-5.

6.2.3. Fluorescein and Mitoxantrone

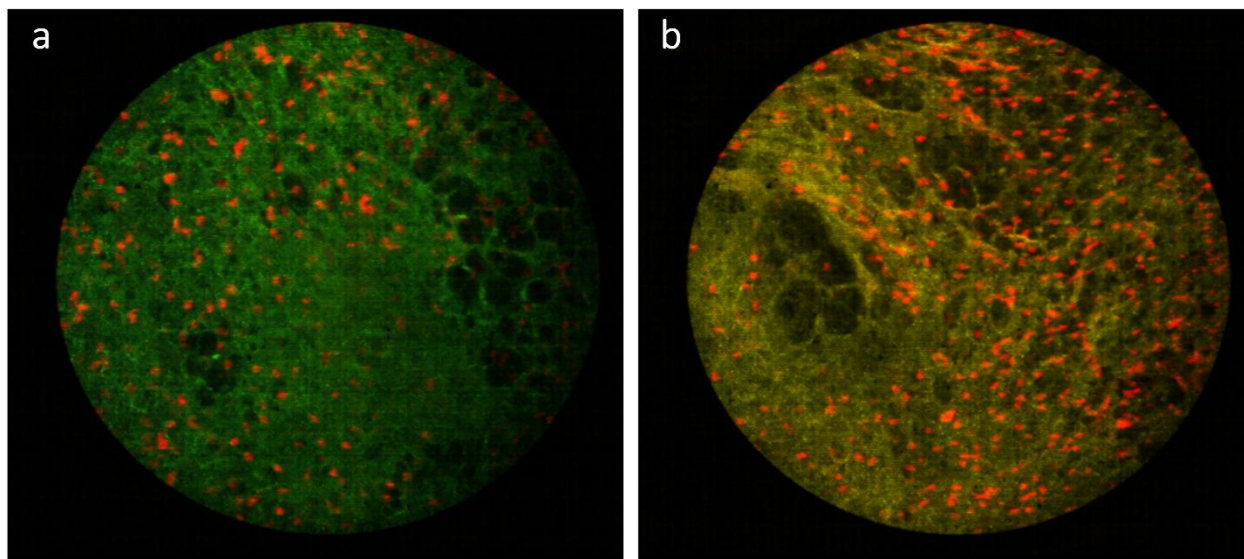


Fig. 6-6. Images collected from the mouse tissue stained by fluorescein and mitoxantrone.

Initially, we thought the precipitation might be due to a chemical reaction between phloxine B and mitoxantrone, so we tried the combination of fluorescein and mitoxantrone to see if this pair led to a similar problem of precipitation. As shown in Fig. 6-6a and Fig. 6-6b, the combination of fluorescein and mitoxantrone produces images that appear to show a mitoxantrone staining pattern consistent with nuclear staining, but we were concerned that this staining pattern could also be due to precipitated mitoxantrone.

To gain more information, we mixed acridine orange, a very effective dye for staining the nuclei, with mitoxantrone and applied the mixture topically to mouse lung samples to see how they stained. The results are shown in Fig. 6-7, where the staining of mitoxantrone (red) and AO (green) are clearly not co-localized, which means that mitoxantrone is not staining the nucleus as we had thought. We also learned that mitoxantrone, as a chemotherapy drug, has some negative effects on the human body. Due to these multiple issues, we decided not to continue to investigate mitoxantrone in this research work.

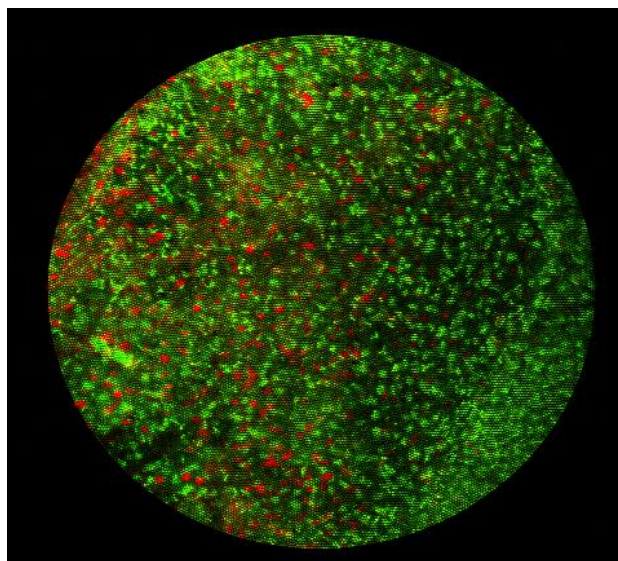


Fig. 6-7. An image collected from the mouse tissue stained by acridine orange and mitoxantrone (without gaussian blur).

6.2.4. Fluorescein and Daunorubicin

Neither mitoxantrone nor methylene blue gave us the desired DNA staining effect, so we tried a combination of daunorubicin and fluorescein. The fluorescence emission wavelength peak of daunorubicin is around 555 nm. Like mitoxantrone, daunorubicin is a chemotherapeutic drug and therefore has potential risks, but the doses of dye we used were very small and within the range of what the body can tolerate. However, the problem with this combination is that the fluorescence excitation and emission wavelengths of the two dyes are very similar, especially fluorescein has a very broad fluorescence emission spectrum, which leads to poor color contrast. The excitation wavelengths of the two are also very similar, which makes it impossible to adjust the fluorescence intensity of the two dyes by adjusting the light source intensity of two lasers.

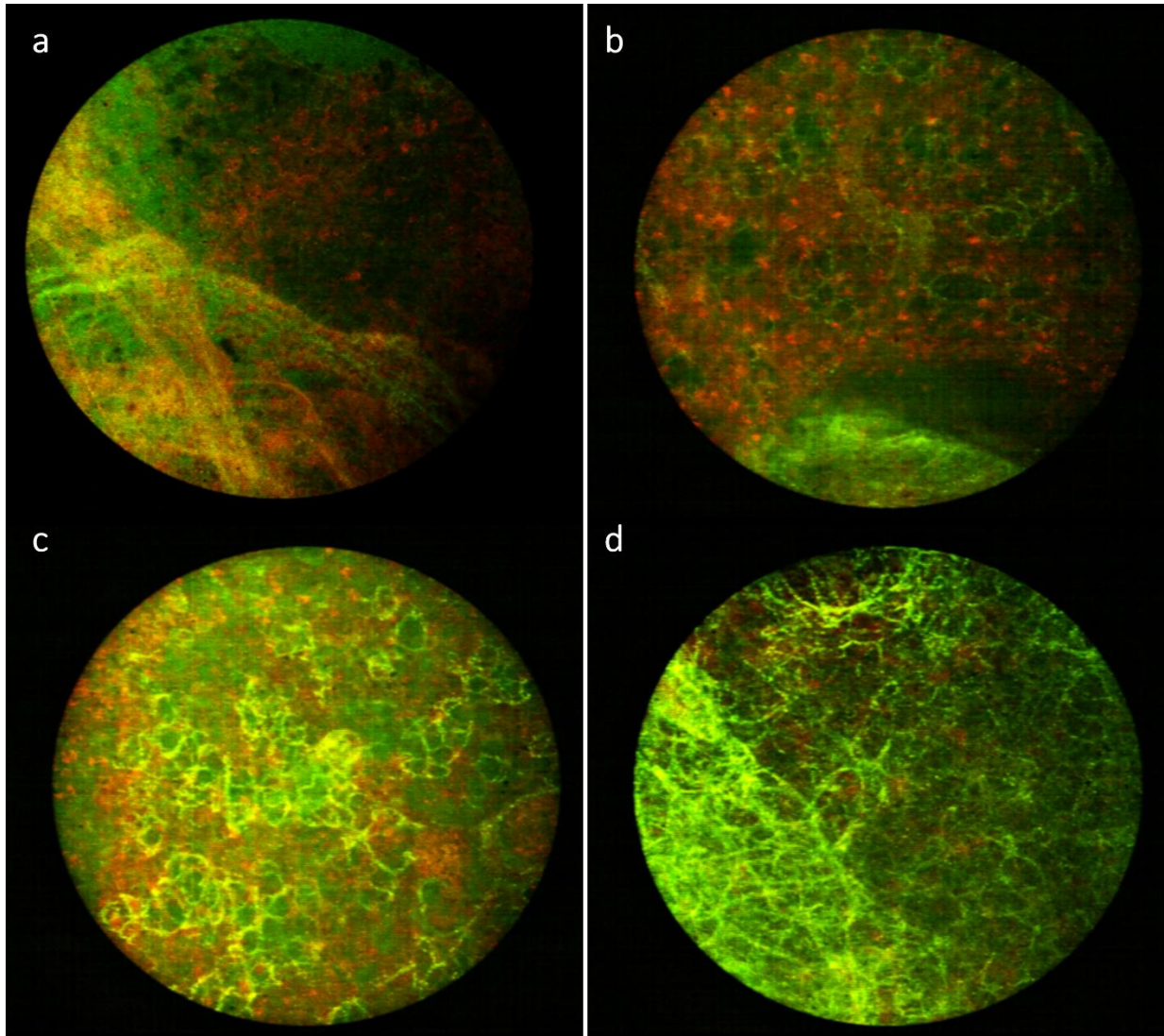


Fig. 6-8. Images collected from the mouse tissue stained by fluorescein and Daunorubicin.

As shown in Fig. 6-8, although fluorescein is very efficient in staining connective tissue, the color contrast between connective tissue and cell nuclei is poor with this combination of dyes due to their highly overlapped wavelengths. The background color problem brought by fluorescein is not improved, and the whole picture is greenish. Daunorubicin, on the other hand, as a DNA dye, although it looks better than mitoxantrone and methylene blue (as shown in Fig. 6-8b), the cell distribution is still too sparse as shown in Fig. 6-8d.

6.2.5. Phloxine B and Proflavine

This dye combination consists of phloxine B and proflavine, where phloxine B is responsible for staining connective tissue and proflavine stains DNA in the cell nucleus. Proflavine has been shown to be very similar to AO, with very rapid staining and high selectivity for staining cell nuclei. Phloxine B has been previously tested and its staining and spectral fluorescence emission properties are satisfactory. However, a disadvantage of this combination is that the fluorescence emission spectra of the two dyes are relatively similar, better than daunorubicin and fluorescein, but still a problem for color contrast. In addition, the excitation wavelengths are also very similar, so we cannot adjust the laser to change the relative fluorescence intensity of the two dyes.

Fig. 6-9 shows images using proflavine for staining the nuclei (green) and phloxine B for staining connective tissue (red). In Fig. 6-9a and Fig. 6-9b the spectral unmixing algorithm was not used, so the color contrast between the two is rather poor. However, proflavine stains cell nuclei more efficiently than any of the previous DNA stains, and phloxine B maintains good staining specificity for connective tissue. After the introduction of the spectral unmixing algorithm, we can see that the color contrast between the two stains increases significantly as shown in Fig. 6-9c and Fig. 6-9d. And by adjusting the relative display intensity of the two dyes, we can see that the color contrast between the two dyes increases significantly and the whole picture looks better.

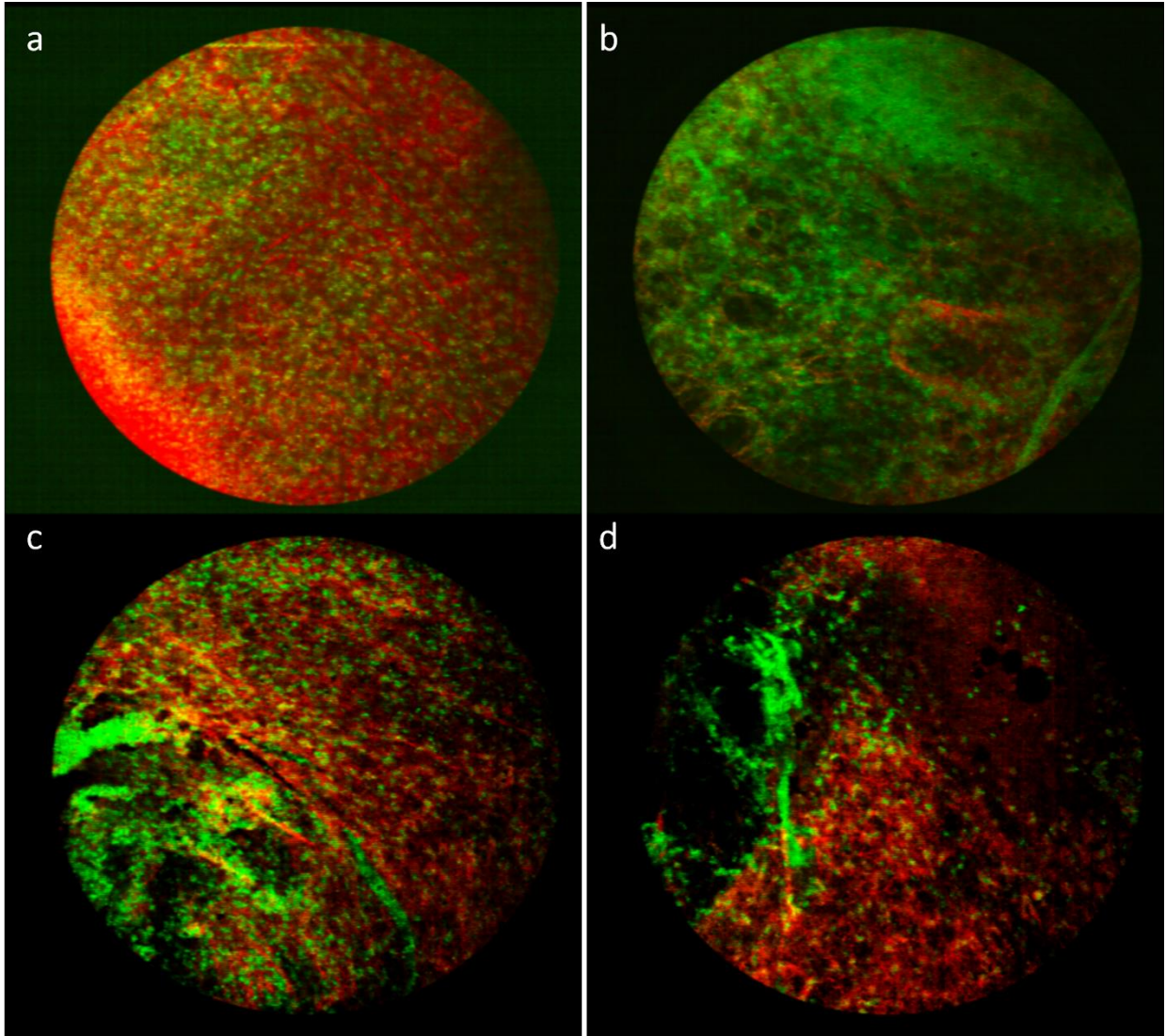


Fig. 6-9. Images collected from the mouse lung tissue stained by proflavine and phloxine B.

6.2.6. Proflavine and Rose Bengal

For the last combination of dyes, we investigated proflavine and rose bengal. The fluorescence spectral excitation and emission properties of rose bengal are very similar to those of phloxine B.

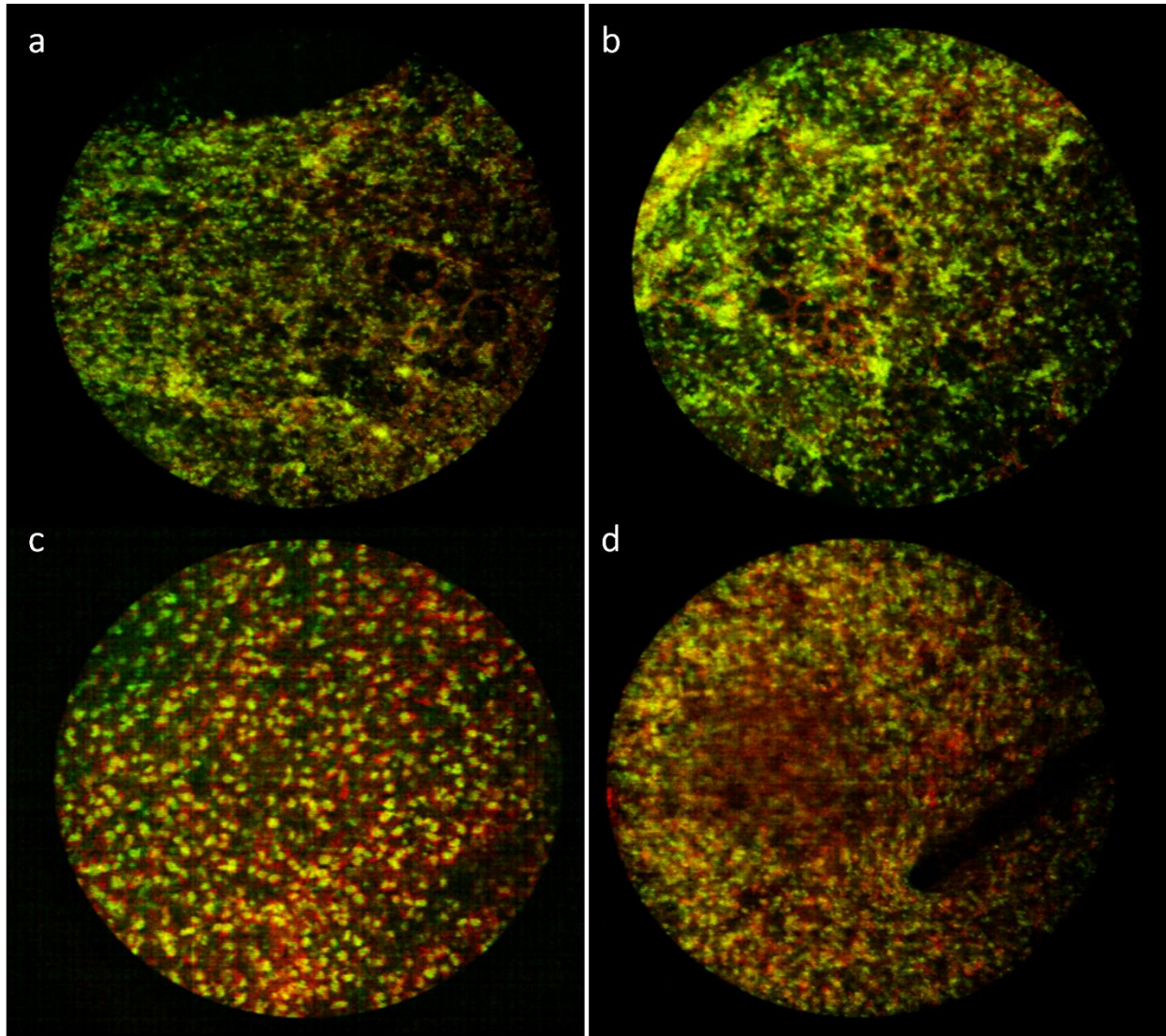


Fig. 6-10. Images collected from the mouse tissue stained by proflavine and rose bengal.

As we can see in Fig. 6-10, the performance of this combination is good. Rose Bengal's staining of the connective tissue is similar to that of phloxine B. We did not use the spectral unmixing algorithm for these four images, but they all turned out very well. We can use the

spectral unmixing algorithm to improve the image quality further. Rose bengal has a potential problem in that it photo bleaches rather quickly compared to phloxine B. However, since imaging is done in a real-time mode after application of the dye, this should not be a big problem. In the end we decided to use a combination of rose Bengal and proflavine for our next set of experiments.

6.3 Rat Open Biopsy Simulation

In previous experiments with mice, we removed the lungs from the animal's body, made a clean cut through the lung tissue, soaked the lung tissue in one of the fluorescent dye combinations described above, and then imaged the tissue with the MSCE instrument. Due to the longer staining time, the staining efficiency of the dye will be higher than in the clinical situation. To simulate the clinical situation and to test the performance of our system, in this round of experiments, instead of removing the lungs from the rats, we open the rat's chest cavity, puncture the lungs with an introducer needle, insert the fiber bundle probe through the needle, and deliver the dye into the lungs, while acquiring real-time images with the MSCE system, as shown in Fig. 6-11. Overall, the staining time for the dye will not be very long and we will be able to collect data that are more similar to the clinical situation.

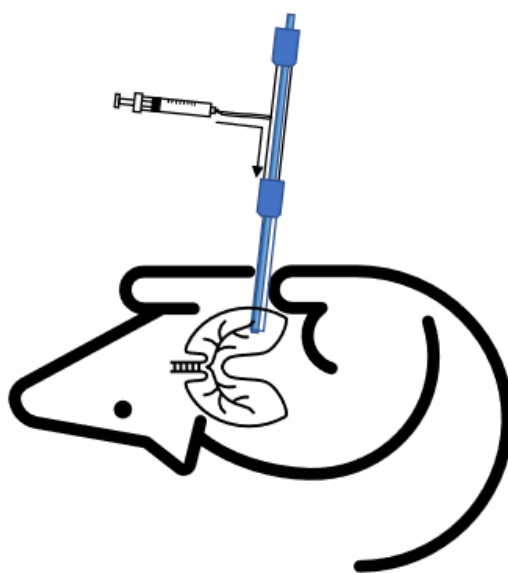


Fig. 6-11. Rat lung biopsy simulation.

6.3.1. Image from Surface of the Rats' Lung

We found an interesting phenomenon in the experiment. The surface structures of the lungs of rats are different than the internal structure. The epithelial surface of the lung is more cellular and the cells are more evenly distributed. The connective tissues on the surface of the lung are also different than lung tissue in the interior of the lung.

Fig. 6-12 shows the surface of the lung of a rat. With use of the spectral unmixing algorithm, we can see that the color contrast between proflavine and rose bengal is sharper, which makes it easier for the observer to distinguish between the two different dyes and the structures they stain. In Fig. 6-12a and Fig. 6-12d we can see cell nuclei more clearly than connective tissues. The different lung surface areas also present very different images, in Fig. 6-12a and Fig. 6-12b we can see that the connective tissue sometimes appears as strips, while in Fig. 6-12c and Fig. 6-12d we can hardly see the connective tissue. In Fig. 6-12c, we can see the black area because the

probe surface does not completely touch the lung, so that part of the sample is at different depths, which also shows the confocal nature of the MSCE system.

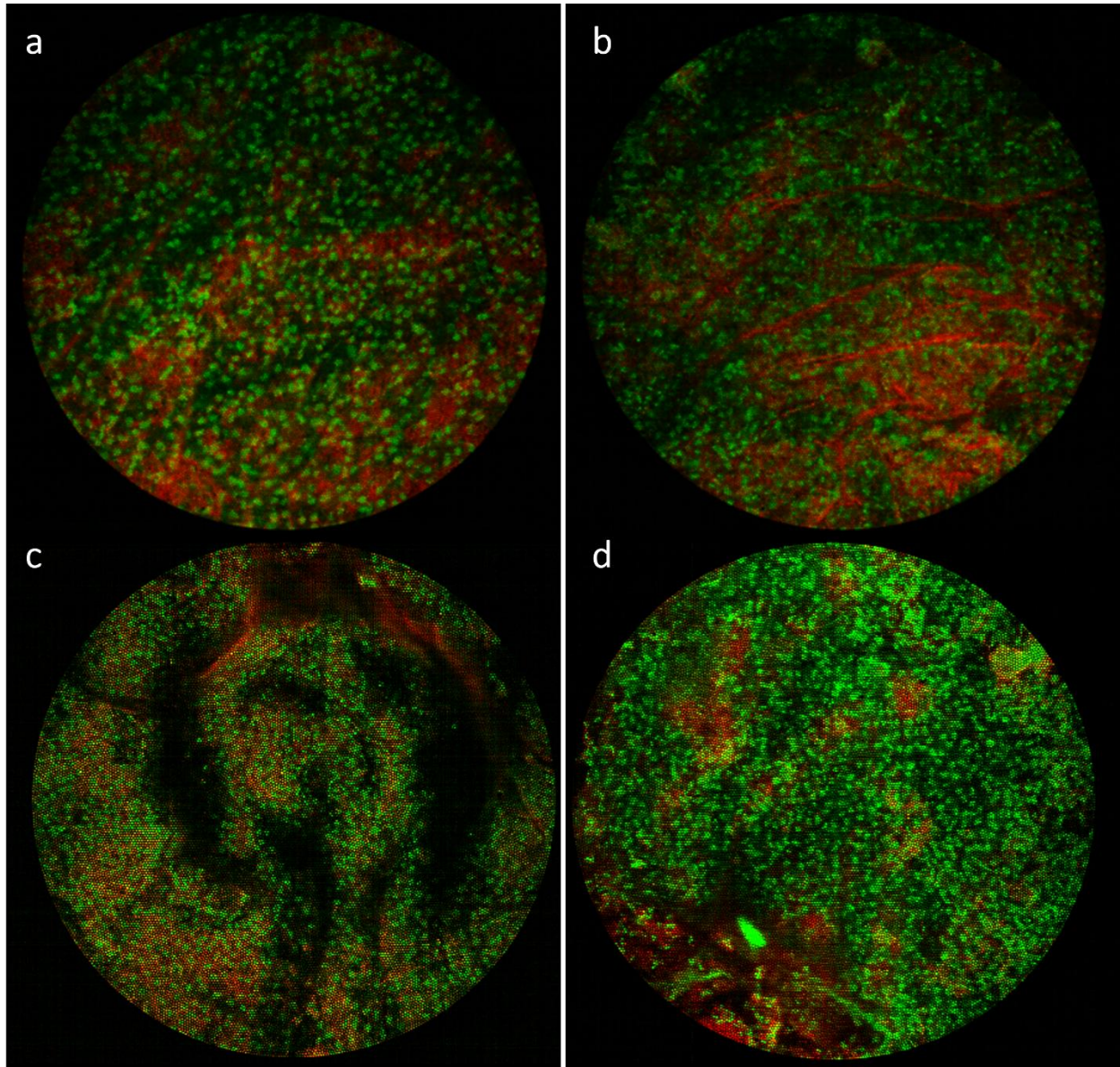


Fig. 6-12. Images of rat lung surface from biopsy simulation. Dye combination: proflavine and rose bengal.

6.3.2. Image from Inside of the Rats' Lung

To image the tissue deeper inside the lung we use the stylet to make a hole in the lung of the rat, after which the stylet is replaced with the MSCE probe, dye is delivered and the images of the inside of the lung are acquired. In practice, it can be difficult for the introducer needle and stylet to make a hole in the surface of the rat's lung because the tissue is so soft. In addition, the anatomy of human lung is different than rat lung, which has multiple thin overlapping lobes. Even if the introducer needle is successfully placed, there is not a lot of space for axial movement due to the thin structure of rat lung.

Nevertheless, we managed to acquire some images of the interior of the rat lung, as shown in Fig. 6-13. The staining combination of proflavine and rose bengal works well for visualizing the normal alveoli as dark structures surrounded by some connective tissue and with a more sparse distribution of cells nuclei.

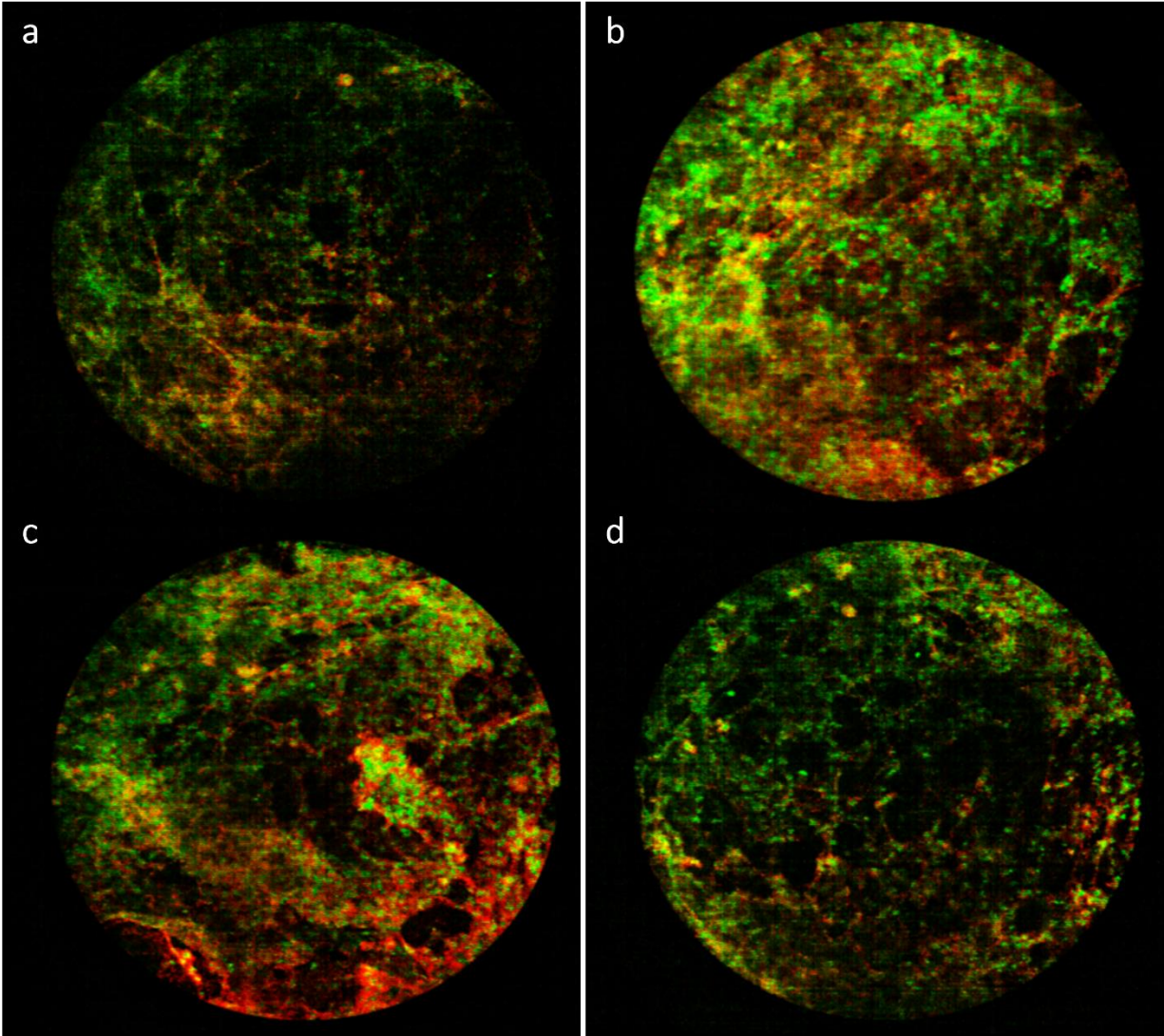


Fig. 6-13. Images inside rat's lung from biopsy simulation. Dye: proflavine and rose bengal.

In the next section, we will use the images of the rat samples collected in this section as a standard for healthy tissue to be referenced to human samples. It is worth pointing out that although the alveoli of rats are smaller than those of humans, the cell size of rats, which are also mammals, is nearly the same as that of humans so that we can use the healthy lung samples from rats as a reference for what normal human lung samples would look like. We can look for the differences that occur with lung disease in human subjects.

6.3.3. Videos

One of the major capabilities of the MSCE system is the ability to observe the lung's interior structure in real-time. However, there is no way to show videos, so I have taken two still frame images from two videos, one from the surface of the lung and the other as the probe enters the interior of the lung. These still frame images are shown in Fig. 6-14. Links to videos from which these frames were taken can be found in the supplemental material.

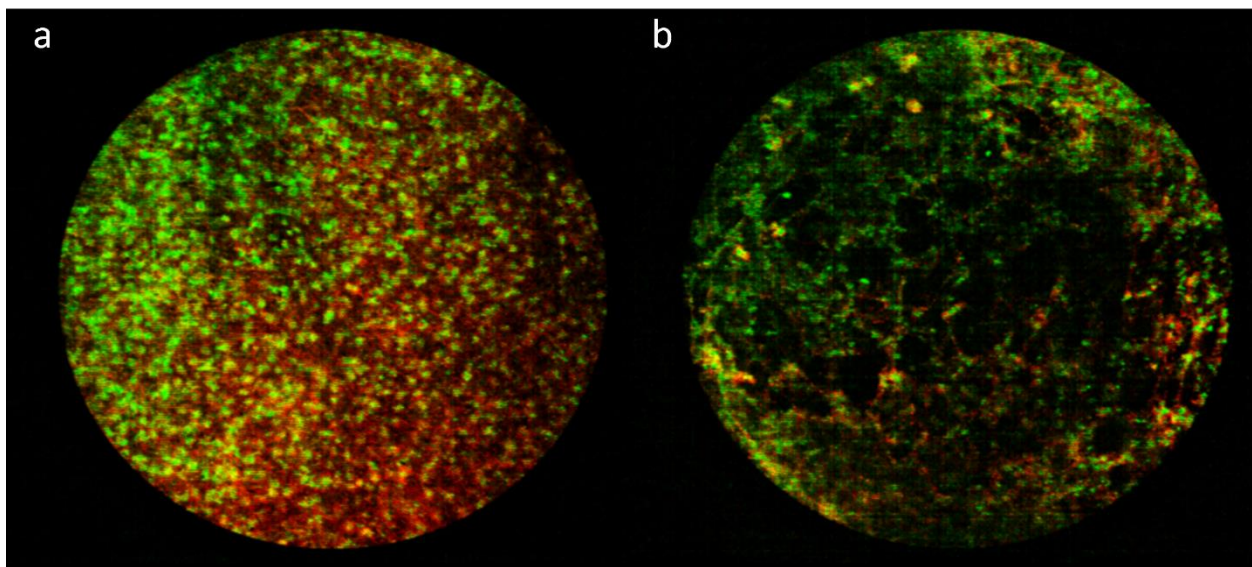


Fig. 6-14. Still frames from videos. a: from the surface of the rat lung, and b: from the interior as the probe enters the lung.

6.4 Ex-vivo Human Lung Tissue

In the middle and late stages of the project, we obtained clinical human ex vivo lung samples through a collaboration with Dr. Gregory Woodhead. These samples were taken from patients who were undergoing percutaneous lung biopsy of suspicious nodules. The protocol of obtaining human tissue was approved by the University of Arizona Institutional Review Board and patients were consented on the day of their biopsy procedure.

Dr. Woodhead would inform us that biopsy tissue would be available at a particular time and call us when it was ready to be picked up at the Banner University Medical Center. A few core samples would be delivered in a vile of phosphate buffered saline. The core biopsy samples were typically about 0.5 – 0.8mm in diameter (depending on the gauge of the biopsy needle being used) and 3-15 mm in length. Tissue samples were stained with a 1:1 combination of 200 μ M proflavine and 200 μ M rose bengal for a time of approximately 1-2 min, after which the tissue was rinsed in saline and placed on the frosted surface of a standard glass slide. The slide was placed on an x,y,z stage and positioned such that the tissue was directly under the distal end of the fiber bundle probe. Some of these biopsy needles used were thinner gauge than the ones we plan to use, so some extracted lung tissue samples did, in some cases, not fully occupy the full field of view of MSCE. We encountered some operational difficulties when looking at ex vivo human lung samples: because the ex vivo samples were much smaller than the mouse or rat lung tissue samples we had previously looked at, there was a high risk of distorting the samples as the probe touched and moved over the sample. Also, because some samples are already diseased, they are very fragile and can sometimes be torn apart.

After imaging the samples with the MSCE instrument, samples were placed inside Surgipath bio-wrap paper and then into tissue cassettes. The cassettes were placed in formalin for 45 to 60 minutes, and then in 70% ethanol. Afterwards, the samples were delivered to Tissue Acquisition and Molecular Analysis Resource for standard H&E processing. In this section, we compare the samples after conventional H&E processing with images obtained on the MSCE instrument.

We divided the abnormal human ex vivo samples into three main categories: necrotic, inflamed, and cancerous tissue. Since the samples we collected were from suspicious lung

nodules, all ex vivo human lung samples are abnormal. I will show the images we collected from each type of sample in turn.

6.4.1. Necrotic Lung Tissue

Necrosis, also known as cellular necrosis, refers to one type of permanent cell death. Necrosis is generally induced by physical, chemical, and biological factors and can be from external or internal sources. There are many external causes of necrosis; for the lungs, smoking can lead to necrosis of lung tissue, while some other inflammatory conditions may be followed by residual necrotic cells.

Because necrotic cells are inactive, some dyes do not stain the cells and connective tissue well, so we often do not see the lung tissue and cell nuclei well in necrotic tissues.

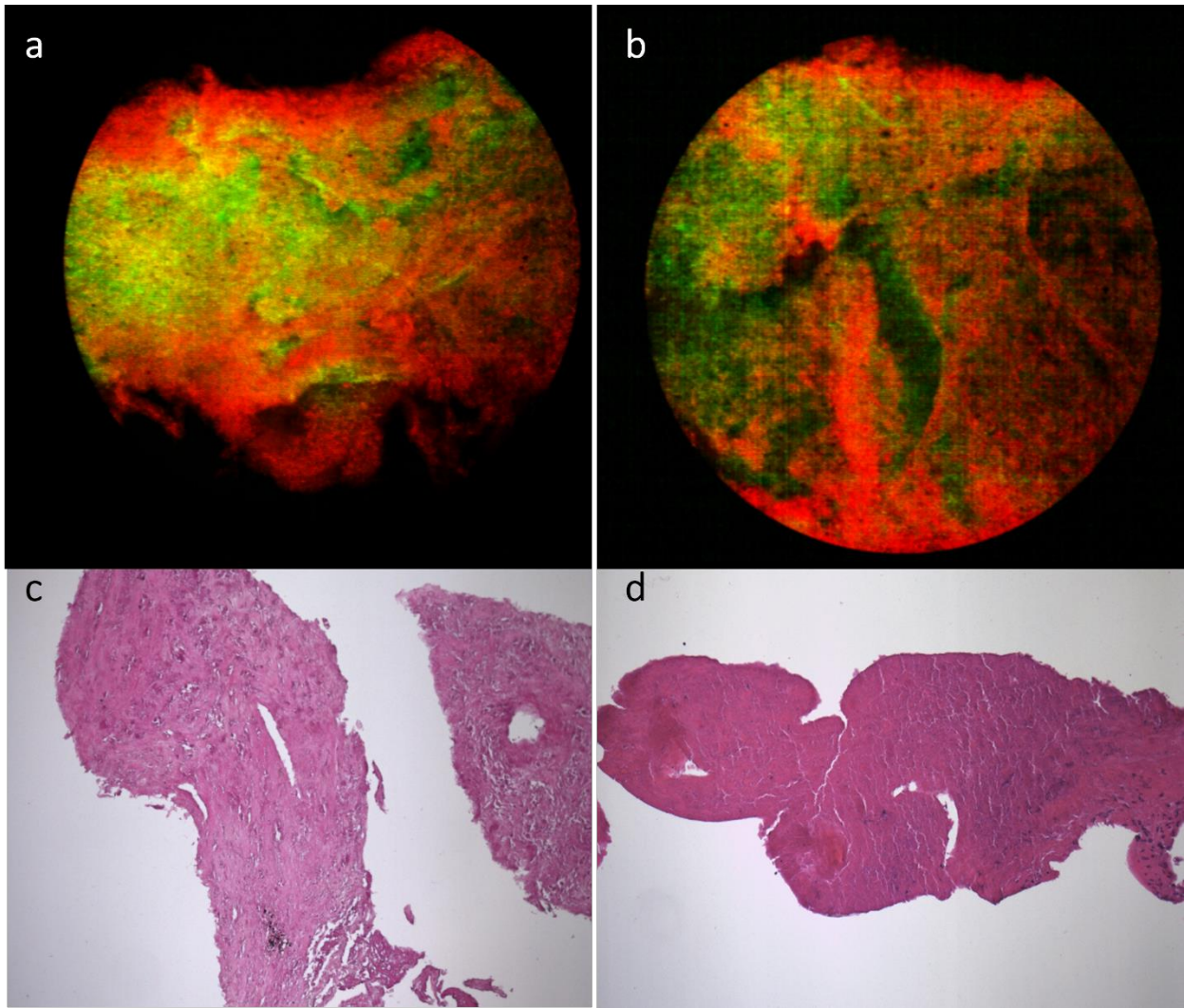


Fig. 6-15. Ex-vivo human necrotic tissue from lung needle biopsy.

The first set of images Fig. 6-15 are from necrotic tissue. Fig. 6-15a and Fig. 6-15b are from the MSCE system, where the dyes used are proflavine and rose bengal. Proflavine stains the DNA and in normal tissue, structurally shows cell nuclei, which we display in green. Rose bengal stains proteins and structurally shows extracellular connective tissue, which we display in red. Fig. 6-15c and Fig. 6-15d are images from the H&E-stained histology samples of the corresponding tissues in Fig. 6-15a and Fig. 6-15b, respectively. We can see that in necrotic samples, most of the organized cellular and nuclear structure has been lost, so the proflavine

nuclear stain more or less uniformly stains the remaining broadly distributed pieces of nuclear material. Therefore, in MSCE observation, we cannot clearly see the green nuclei, while the green nuclei dye is evenly distributed in the sample. Similarly, the red dye does not adhere well to the connective tissue. This makes the whole picture look more like a soupy mixture of molecular material with little correlation to normal lung structures. Due to the different permeability of the two dyes, proflavine appears to be distributed more in the central part of the core while rose bengal is distributed more on the outside of the core. In the H&E images in Fig. 6-15c, and Fig. 6-15d, we can hardly find any nuclei, the whole picture shows a uniform lavender color. We don't see any alveoli or organized connective tissue structure.

The images obtained by H&E and our MSCE system have essentially the same result, which suggests that the MSCE can be used to identify necrotic tissue.

6.4.2. Inflammatory Tissue

The images in Fig. 6-16 are from samples that have significant inflammation. Again, the dyes used are proflavine and rose bengal. Fig. 6-16a and Fig. 6-16b are from the MSCE system, where proflavine stains the nuclei and marks the cell distribution, which we show in green, and rose bengal stains the connective tissue and marks the tissue structure, which we show in red. Fig. 6-16c and Fig. 6-16d are from the H&E histology samples, which correspond to Fig. 6-16a and Fig. 6-16b, respectively. We can see that, unlike the previous necrotic samples, in the inflammatory samples both the nuclei and the connective tissue were successfully stained. We can observe thicker red connective tissue, which indicates that this part of the tissue may be more fibrotic, and may represent inflammation in this area. In the H&E image of this sample, we can see that the nuclei are successfully stained, showing a dark purple color in the image, and the

lung stroma shows a light pink color. And the arrows mark some pink areas, which represent inflammation and fibrosis. Again, we failed to find healthy alveoli in these samples.

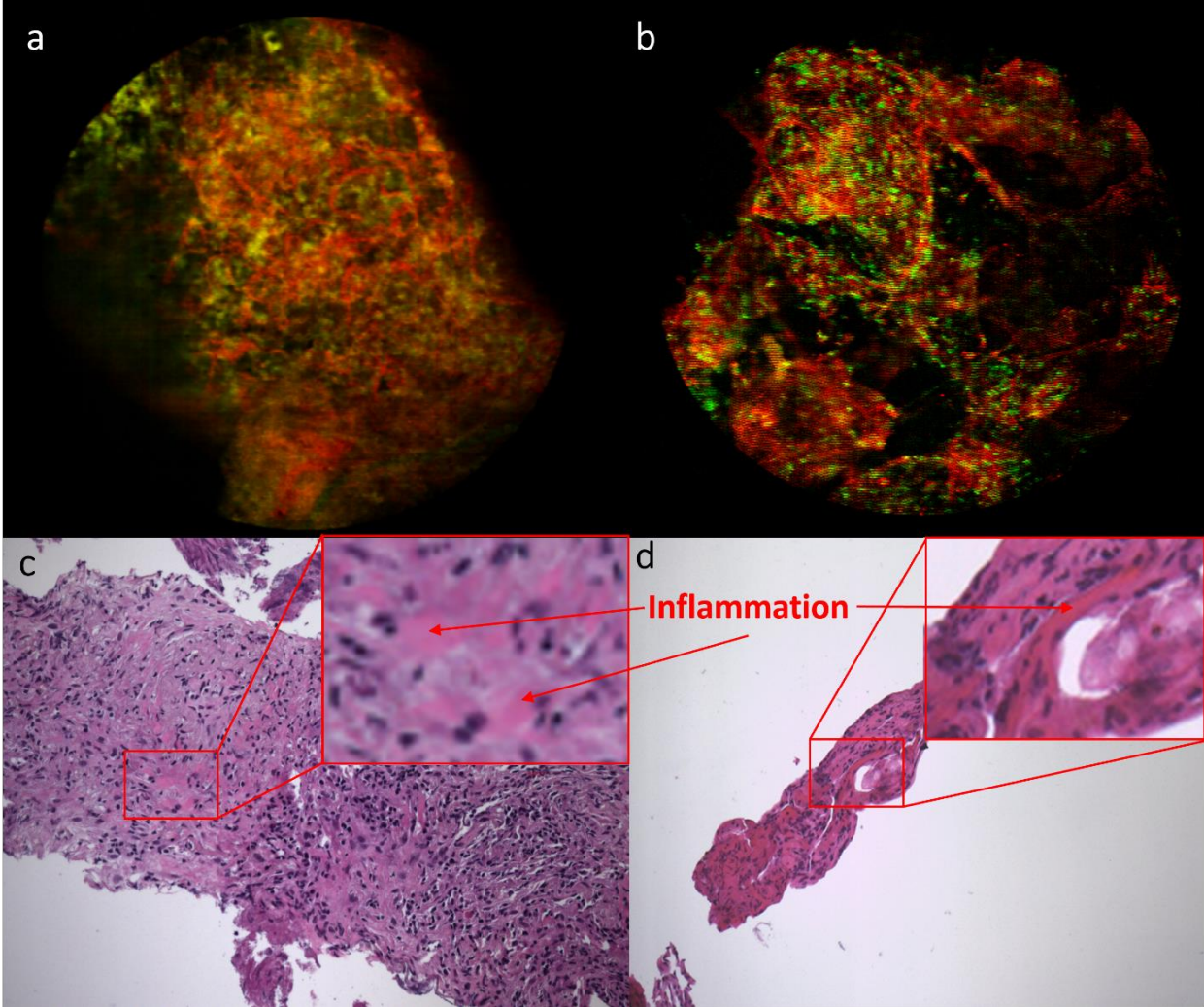


Fig. 6-16. Ex-vivo human inflammatory tissue from lung needle biopsy.

The images obtained by H&E and our MSCE system have similar results, which suggests that the MSCE instrument can be used to observe an inflammatory tissue response.

6.4.3. Cancerous tissue

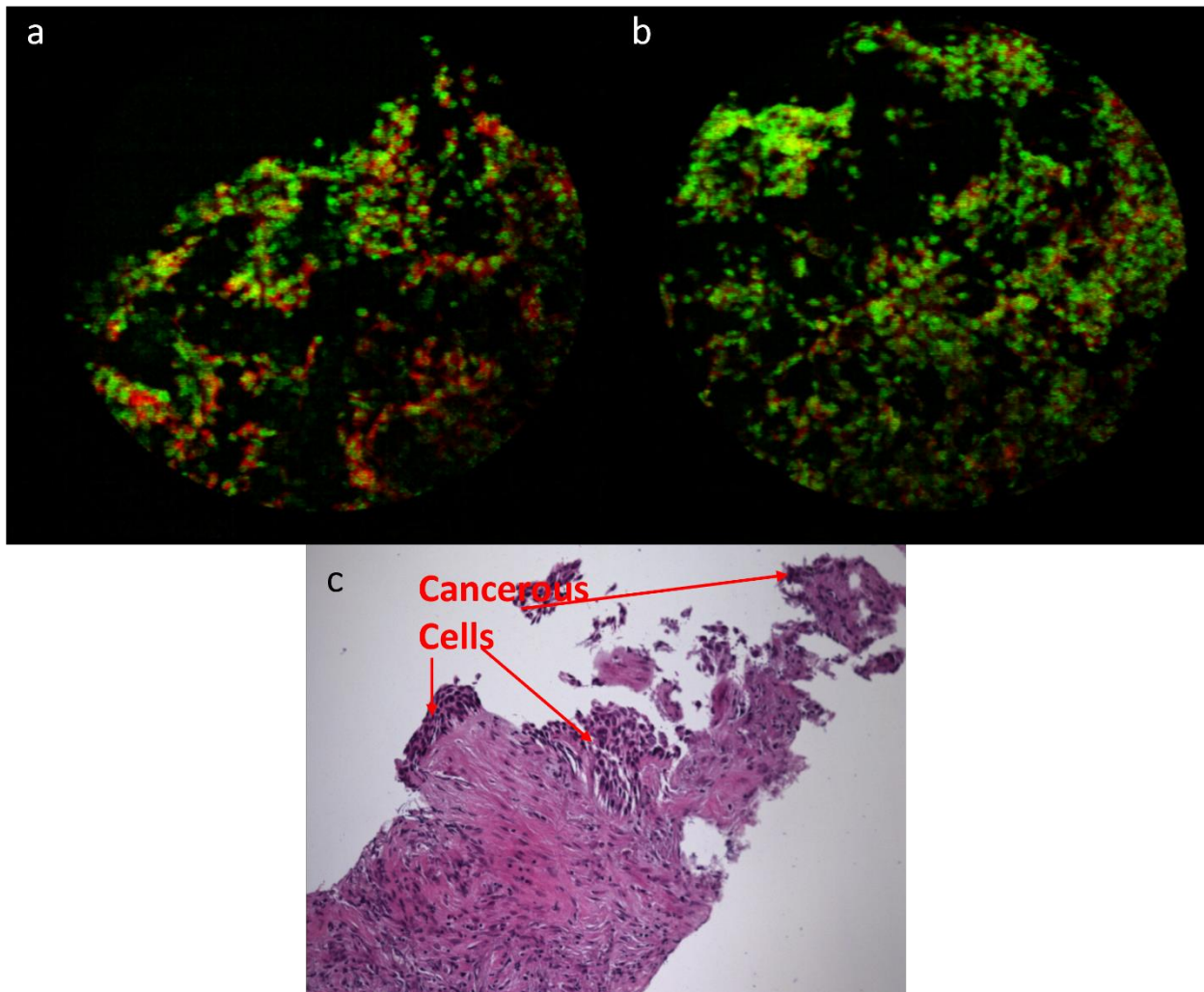


Fig. 6-17. Ex-vivo human cancerous tissue from lung needle biopsy.

The images in the third set (Fig. 6-17) are taken from a sample with cancerous cells. Again, the dyes used here are proflavine (green) and rose bengal (red). Fig. 6-17a and Fig. 6-17b are images obtained with the MSCE system, where proflavine stains the nucleus and marks the cell distribution, and rose bengal stains the connective tissue and marks the tissue structure. Fig. 6-17c is the corresponding H&E-stained samples. In Fig. 6-17a and Fig. 6-17b, we can see that the nuclei in this section are larger and denser than in the healthy tissue. In addition, the red connective tissue in the cancerous part also looks disrupted. In the experimental manipulation,

we found that the cancerous part was indeed very fragile, and some external contact could cause the cancerous part to detach from the sample. In the H&E histology image, we also found dense large cancerous cells in the corner of the sample as indicated by the arrows. Not surprisingly, we were also unable to find healthy alveoli in this sample.

Therefore, the images obtained by H&E and our MSCE system have the same similar results, which suggests that the MSCE system can be used to observe and identify cancerous tissues.

6.4.4. Videos

Again, we have acquired several videos with the MSCE system that demonstrate the real-time imaging capability.

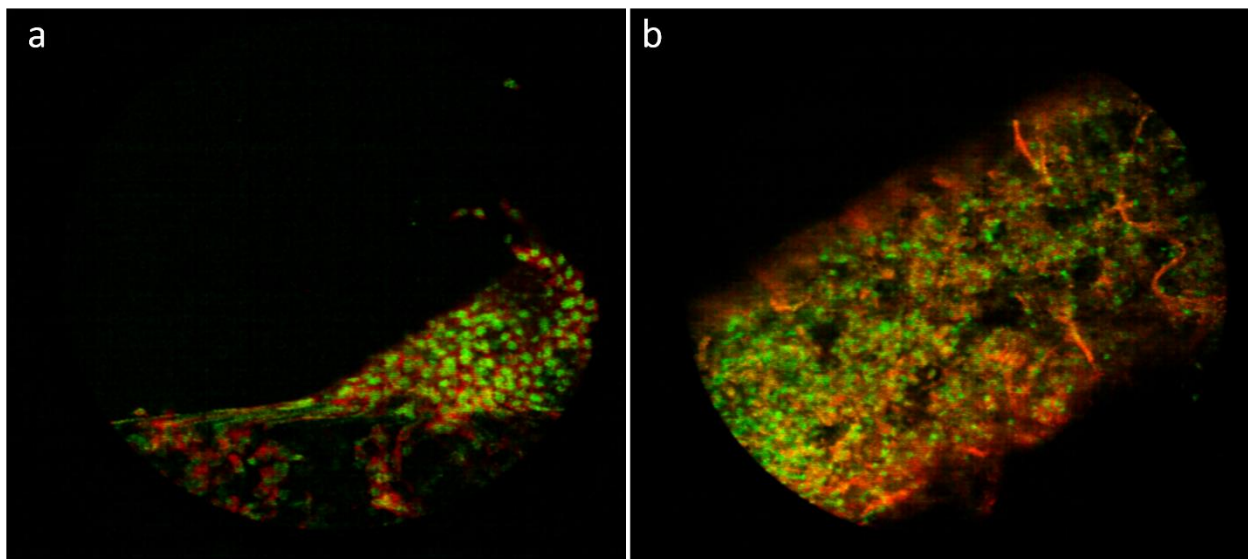


Fig. 6-18. Still frame images from a video of a: cancerous ex-vivo human lung tissue; b: inflammatory ex-vivo human lung tissue. Dye applied: proflavine (DNA-binding, green) and rose bengal (connective tissue binding, red).

Fig. 6-18 shows two frames from two different videos ex vivo human lung tissue (see supplementary material). This sample was taken from a high gauge biopsy needle, so the core size is smaller than the FOV of the MSCE. In Fig. 6-18a, we can clearly see the change in the image as the probe approaches the cancerous tissue from the outside, and we can see that there

are some normal cells below this frame, followed by the cancerous cells. In Fig. 6-18b, as the probe moves slowly along the sample, we can clearly see the changes that occur as the sample imaged moves from cells to fibrosis. These two videos demonstrate the MSCE's ability to provide real-time images of tissue at the distal tip of the fiber bundle probe and suggest that the MSCE system may be able to identify cancerous tissue in a clinical setting and to help clinicians make a diagnosis and select the best location core biopsy sampling.

6.5 Summary

This chapter shows some of the images we acquired with the MSCE instrument.

In an experiment looking at stained paper, we tested the MSCE system's ability to image objects with different fluorescent wavelengths. We could clearly distinguish the areas marked by different markers and the overlapping areas. Then we used the system to look at self-fluorescent business cards, and this time we used the CIE mapping function to display the colors, and the results showed that the MSCE system has the ability to display the actual colors. Therefore, I believe that the system has sufficient color resolution and imaging capability to perform more extensive clinical validation studies.

We can see from the mouse images that proflavine and rose Bengal are a good combination of dyes to use, and although they have similar excitation and fluorescence wavelengths, we can still clearly distinguish them in our experiments with the help of the spectral unmixing algorithm.

We likewise tested the staining effect of other stains on mouse lung section samples. Among the nuclear dyes, mitoxantrone, daunorubicin, and methylene blue have drawbacks: Mitoxantrone reacts with other dyes and does not accurately label nuclei, both Mitoxantrone and Daunorubicin are chemotherapeutic drugs with potential risks to humans; Daunorubicin is too

similar to Fluorescein in its fluorescence wavelength. Methylene blue was not chosen because of its slow staining speed and low fluorescence intensity.

In contrast, fluorescein and phloxine B, which are connective tissue stains, also have some problems. Fluorescein stains more than connective tissue and its fluorescence excitation wavelength is similar to the autofluorescence excitation wavelength of optical fiber⁴⁴, which will lead to excessive image noise. Since we need to use proflavine as a nucleus stain, the fluorescence band of Phloxine B overlaps with proflavine more than rose Bengal, so we finally chose rose bengal as our connective tissue stain.

We simulated the clinical situation of topical staining using a euthanized rat model. We successfully observed the lung surface and lung interior of rats with our MSCE system and clearly observed lung structures such as alveoli. Our dye delivery system also successfully stained the target objects with satisfactory image results. Therefore, I believe that the MSCE system has sufficient capability to be used in clinical trials and that our rat images can be used as a reference sample for comparison with human samples.

In the process of observing *ex vivo* human lung samples, we found that these lesions could be classified into three main categories: necrotic, inflammatory, and cancerous tissues. We successfully observed different types of samples with the MSCE instrument. In necrotic tissue, we could not clearly observe the nuclei and cell distribution, and the nuclei and connective tissue stains were more uniformly distributed throughout the object. In inflammatory tissue, we saw the nuclei and their distribution, and we also saw thick, fibrous connective tissue, which is one of the hallmarks of inflammation. In the cancerous tissues we can find aberrant, dense populations of cells with large nuclei, which is one of the hallmarks of lung cancer. By comparing the H&E results, I believe that the MSCE system can provide images of the target nodules in clinical trials

and help physicians in selecting appropriate tissue for percutaneous core needle biopsies of the lung.

7 Conclusion and Future Work

This dissertation describes how we designed and tested the MSCE system. The system relays the image of the needle tip of a lung biopsy through a fiber optic bundle to a line scan confocal microscope to obtain cellular level images. Then, by inserting a dispersive element, the system was able to successfully implement its multispectral imaging functionality. A dye delivery system was developed allowing for topical delivery of dye through the introducer needle of a core needle biopsy technique. The MSCE system can help guide the lung biopsy process by providing color images of tissue at the distal end of the fiber probe.

In our experiments, we first experimented with different combinations of stains in mice and finally selected the combination of proflavine and rose bengal as the best option for an FDA-approved dye combination.. We hope that more FDA-approved dyes can be used in this system in the future. In experiments with rats, we successfully observed the lung surface of healthy rats as well as the internal lung tissue in testing the dye-delivery system. In imaging ex-vivo human core biopsy samples, preliminary results with the MSCE system indicate that it can successfully distinguish three types of non-healthy samples: necrotic tissue, inflammatory tissue, and cancerous tissue. This demonstrates the ability of the MSCE system to help distinguish critical structural differences in lung tissue. Interventional radiologists can use these differences to obtain the necessary diagnostic information and extract tissue more accurately during core biopsy procedures. Not only that, but perhaps real-time MSCE imaging can help physicians achieve an accurate diagnosis without extracting tissue. This is more likely to occur in benign disease, as physicians almost always want to sample potentially cancerous tissue even if it is

known to be cancerous. Additional histologic and genetic testing of lung cancer tissue can help predict response to treatment and the patient's overall prognosis.

We may be able to look for other dyes in the future. Since MSCE can provide not only color images but also the spectrum of the object at the same time, in future applications, if we can find stains that are FDA-approved and have a spectrum that varies with pH, then the MSCE may be able to go even further to inform the physician whether a cancerous phantom is present near the probe by the spectrum. This is because the pH tends to be more acidic around cancerous cells that employ anaerobic respiration. Or we can find other stains with coloring characteristics that are not limited to connective tissue and nuclei and can color cancer cells alone.

The current MSCE system is sufficient for real-time imaging at 6 frames/second. However, an optimized data acquisition control program and a sensor with a higher signal-to-noise ratio may be able to increase the frame rate further. In the future, the system control program could be written in C or other more efficient languages so that the image processing could be done by the GPU, which could significantly decrease the computing time between each frame. Moreover, by making it more efficient, we might be able to introduce some exciting image processing programs. For example, a program to reduce dithering, automatically identify and mark suspicious areas, and a program to identify synchronization situations. The tolerance of the scanning mirror is also an essential condition for the frame rate. A scanner with higher tolerance can increase the ratio of the ramp function to improve the system's frame rate. Moreover, we can use a data acquisition system (DAQ) to control the sensor and function generator, dramatically improving the system's stability.

In terms of optical system design, there are still areas where the MSCE can be improved. We can improve the frame rate by changing the scanning method. Currently, we are using a single

line scanning method, but in the future, we can change the system to a dual or even triple line simultaneous scanning method to increase the scanning rate. In terms of lens design, we may be able to make use of the second design described in this dissertation, as this system has better aberration correction due to the use of custom lenses.

The current MSCE system cannot change the dispersion angle. We can replace the prisms with opposite prism sets. When the two prisms are in opposite directions, the system will have no dispersion, and MSCE will change from a multispectral system to a grayscale one. When there is a certain angle between the two prism directions, we can change the dispersion angle of MSCE by controlling this angle. One of the potential problems with the current MSCE is that we do not need 20 channels for some cases because more channels would reduce the signal-to-noise ratio. Furthermore, in some cases, 20 channels are not enough to accurately sample the object's spectrum. Using the above method, we can somewhat adjust the number of channels in the system.

The lateral resolution of the MSCE system is fundamentally limited by the sampling frequency of the fiber bundle. In this paper, we introduce some methods of fiber bundle depixelation and built prototypes to test two of them. They both can effectively improve the resolution of fiber bundle imaging and prevent image distortion caused by the core sampling distribution. The fiber bundle also limits the axial resolution of the MSCE system. However, this cannot be calculated. Therefore, we devised a new method to measure the axial resolution of fiber bundle-based fluorescence systems accurately. Finally, it may take some time for the pathologist or interventional radiologist to become familiar with the staining properties of the fluorescent dyes employed. However, it is encouraging that at least some of the FDA-approved dye combinations appear to provide sufficient contrast and fast enough staining to be helpful in

core lung cancer biopsy procedures. Not only that but the application of proper image processing methods, such as the spectral unmixing algorithm, can go even further to help the user differentiate the dyes and obtain more information from their spectra that is beneficial for diagnosis.

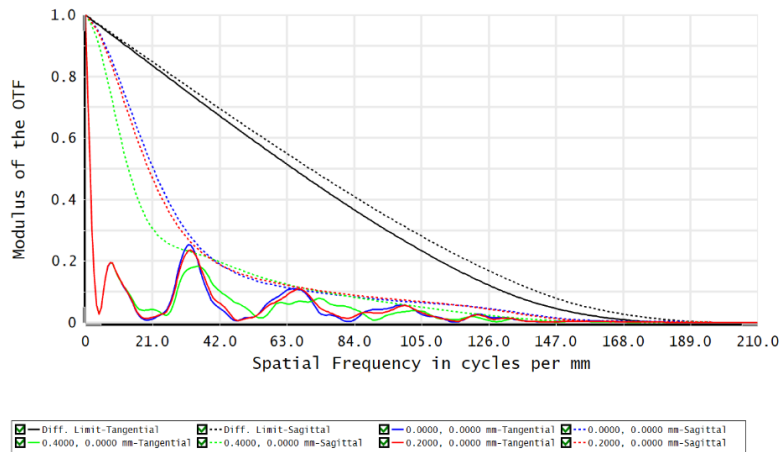
Later, we can evaluate the effectiveness of this system in diagnosing cancer by imaging and diagnosing a large database of human ex-vivo samples to map out the receiver operating characteristic (ROC) curve of this system. In the future, I hope this system can be used in clinical trials to help doctors make effective diagnoses and help more patients get accurate diagnoses and better therapy.

Appendix A: Zemax Design

Lens data for 1st design:

	Surface Type	Element	Radius	Thickness	Material	Co.	Clear Semi-Dia	Chip Zone	Mech Semi-Dia	Conic	TCE x 1E-6	Par 1(unused)	Par 2(unused)	Par 3(unused)		
0	OBJECT	Standard	Infinity	18.00000			0.40000	0.00000	0.40000	0.000...	0.00000					
1	Paraxial			2.00000	1.00,0.0 M		5.81629	-	-	0.00000	0.00000	18.00000	1			
2	Standard		Infinity	5.00000	1.00,0.0 M		5.77185	0.00000	5.77185	0.000...	0.00000					
3	STOP	Standard	Infinity	0.00000			5.66074	0.00000	5.77185	0.000...	0.00000					
4	Standard		Infinity	20.00000			5.66074	0.00000	5.66074	0.000...	0.00000					
5	Coordinate Break			0.00000	-		0.00000	-	-	-	-	0.00000	0.00000	45.00000		
6	Standard		Infinity	0.00000	MIRR...		8.02578	0.00000	8.02578	0.000...	0.00000					
7	Coordinate Break			-59.63647	V		0.00000	-	-	-	-	0.00000	0.00000	45.00000		
8	(aper)	Standard	49794	-50.85000	-7.00000	N-SSK8	12.20000 U	0.50000	12.70000	0.000...	-					
9	(aper)	Standard		40.06000	-3.00000	N-SF56	12.20000 U	0.50000	12.70000	0.000...	-					
10	(aper)	Standard	148.78000	-71.17556	M		12.20000 U	0.50000	12.70000	0.000...	0.00000					
11	Standard		Infinity	-71.17556	P		1.70144	0.00000	1.70144	0.000...	0.00000					
12	(aper)	Standard	-148.78000	P	-3.00000	P	N-SF56	12.00000 U	0.00000	12.00000	0.000...	-				
13	(aper)	Standard	-40.06000	P	-7.00000	P	N-SSK8	12.00000 U	0.00000	12.00000	0.000...	-				
14	(aper)	Standard	50.85000	P	0.00000		12.00000 U	0.00000	12.00000	0.000...	0.00000					
15	(aper)	Standard	Infinity	-40.00000			10.00000 U	0.00000	10.00000	0.000...	0.00000					
16	(tilt/dec)	Standard	Infinity	10.00000		MIRR...	8.05793	0.00000	8.05793	0.000...	0.00000					
17	Coordinate Break	Element Tilt		0.00000			0.00000	-	-	-	-	0.00000	0.00000	-1.33666		
18	(aper)	Standard	Infinity	0.00000		BK7	10.00000 U	0.00000	10.00000	0.000...	-					
19	Coordinate Break	Tiltreturn		5.00000			0.00000	-	-	-	-	0.00000	P	0.00000	P	1.33666
20	Coordinate Break	Element Tilt		0.00000			0.00000	-	-	-	-	0.00000	0.00000	-18.90819		
21	(aper)	Standard	Infinity	0.00000			10.00000 U	0.00000	10.00000	0.000...	0.00000					
22	Coordinate Break	Tiltreturn		16.46592			0.00000	-	-	-	-	0.00000	P	0.00000	P	18.90819
23	Coordinate Break	Element Tilt		0.00000			0.00000	-	-	-	-	0.00000	-2.75505	V	9.74251	
24	(aper)	Standard	49374	61.36000	8.25000	N-BK7	10.00000 U	0.50000	15.00000	0.000...	-					
25	Standard		Infinity	-44.30000	2.80000	N-SF5	5.55220	0.50000	15.00000	0.000...	-					
26	(aper)	Standard	-128.53738	0.00000			14.50000 U	0.50000	15.00000	0.000...	0.00000					
27	Standard		Infinity	94.55492	V		5.53620	0.00000	5.53620	0.000...	0.00000					
28	IMAGE	Standard	Infinity	-			2.80000 U	0.00000	2.80000	0.000...	0.00000					

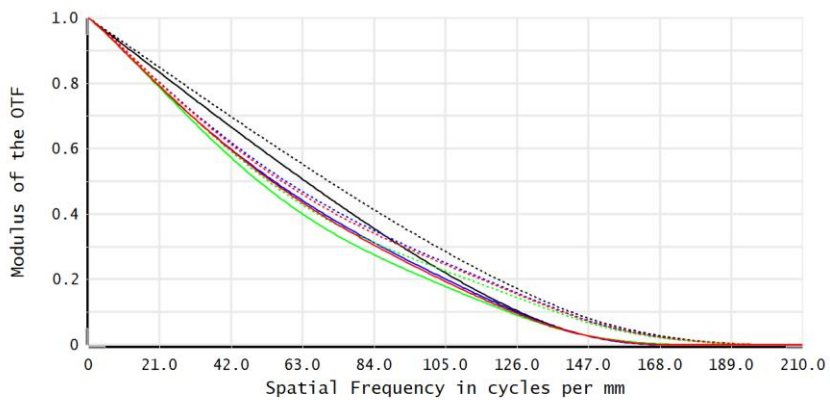
MTF for the 1st design



Lens data for 2nd design

Surface Type	Comment	Radius	Thickness	Material	Co.	Clear Semi-Dia	Chip Zone	Mech Semi-Dia	Conic	TCE x 1E-6	Par 1 (unused)	Par 2 (unused)
0	OBJECT	Standard	Infinity	18.00000			0.40000	0.00000	0.40000	0.00000		
1	Paraxial		2.00000	1.00,0.0 M		5.81629	-	-	0.00000	0.00000	18.00000	1
2	Standard		Infinity	5.00000	1.00,0.0 M	5.77185	0.00000	5.77185	0.00000	0.00000		
3	STOP	Standard		Infinity	0.00000	5.66074	0.00000	5.77185	0.00000	0.00000		
4	Standard		Infinity	20.00000		5.66074	0.00000	5.66074	0.00000	0.00000		
5	Coordinate Break		0.00000		-	0.00000	-	-	-	-	0.00000	0.00000
6	Standard		Infinity	0.00000	MIRR...	8.02578	0.00000	8.02578	0.00000	0.00000		
7	Coordinate Break		-74.70768		-	0.00000	-	-	-	-	0.00000	0.00000
8	Standard		Infinity	-2.88000		7.76535	0.00000	7.76535	0.00000	0.00000		
9	Standard		Infinity	-1.00000		7.82935	0.00000	7.82935	0.00000	0.00000		
10	(aper)	Standard	49794	-50.85000	-7.00000	N-SSK8	12.20000 U	0.50000	12.70000	0.00000		
11	(aper)	Standard		40.06000	-3.00000	N-SF56	12.20000 U	0.50000	12.70000	0.00000		
12	(aper)	Standard		148.78000	-5.00000		12.20000 U	0.50000	12.70000	0.00000		
13	Standard		Infinity	-27.63169 V		7.09895	0.00000	7.09895	0.00000	0.00000		
14	(aper)	Standard		42.34994 V	-3.00000	S-NPH1 S	12.00000 U	0.00000	12.00000	0.00000		
15	(aper)	Standard		53.44132 V	-45.31529 V		12.00000 U	0.00000	12.00000	0.00000		
16	(aper)	Standard		Infinity	-45.31529 P		2.04820	-	-	0.00000	0.00000	
17	(aper)	Standard		-53.44132 P	-3.00000 P	S-NPH1 P	12.00000 U	0.00000	12.00000	0.00000		
18	(aper)	Standard		-42.34994 P	-27.63169 P		12.00000 U	0.00000	12.00000	0.00000		
19	Standard		Infinity	-5.00000 P		7.10188	0.00000	7.10188	0.00000	0.00000		
20	(aper)	Standard		-148.78000 P	-3.00000 P	N-SF56	12.00000 U	0.00000	12.00000	0.00000		
21	(aper)	Standard		-40.06000 P	-7.00000 P	N-SSK8	12.00000 U	0.00000	12.00000	0.00000		
22	(aper)	Standard		50.85000 P	-1.00000 P		12.00000 U	0.00000	12.00000	0.00000	0.00000	
23	(aper)	Standard		Infinity P	-2.88000 P	P	10.00000 U	0.00000	10.00000	0.00000	0.00000	
24	(aper)	Standard		Infinity P	-40.00000		10.00000 U	0.00000	10.00000	0.00000	0.00000	
25	tilt/dec)	Standard		Infinity	10.00000	MIRR...	8.10647	0.00000	8.10647	0.00000	0.00000	
26	Coordinate Break	Element Tilt		0.00000		0.00000	-	-	-	-	0.00000	0.00000
27	(aper)	Standard		Infinity	0.00000	1.52,0.0 M	10.00000 U	0.00000	10.00000	0.00000	0.00000	
28	Coordinate Break	Element Tilt:return		5.00000		0.00000	-	-	-	-	0.00000 P	0.00000 P
29	Coordinate Break	Element Tilt		0.00000		0.00000	-	-	-	-	0.00000	0.00000
30	(aper)	Standard		Infinity	0.00000		10.00000 U	0.00000	10.00000	0.00000	0.00000	
31	Coordinate Break	Element Tilt:return		59.65985		0.00000	-	-	-	-	0.00000 P	0.00000 P
32	Coordinate Break	Element Tilt		0.00000		0.00000	-	-	-	-	0.00000	-9.72466
33	(aper)	Standard	49374	61.36000	8.25000	N-BK7	10.00000 U	0.50000	15.00000	0.00000		
34	Standard			-44.30000	2.80000	N-SF5	5.90649	0.50000	15.00000	0.00000		
35	(aper)	Standard		-128.53738	0.00000		14.50000 U	0.50000	15.00000	0.00000	0.00000	
36	Standard		Infinity	94.58568		5.88623	0.00000	5.88623	0.00000	0.00000		
37	IMAGE	Standard		Infinity	-	2.80000 U	0.00000	2.80000	0.00000	0.00000		

MTF:



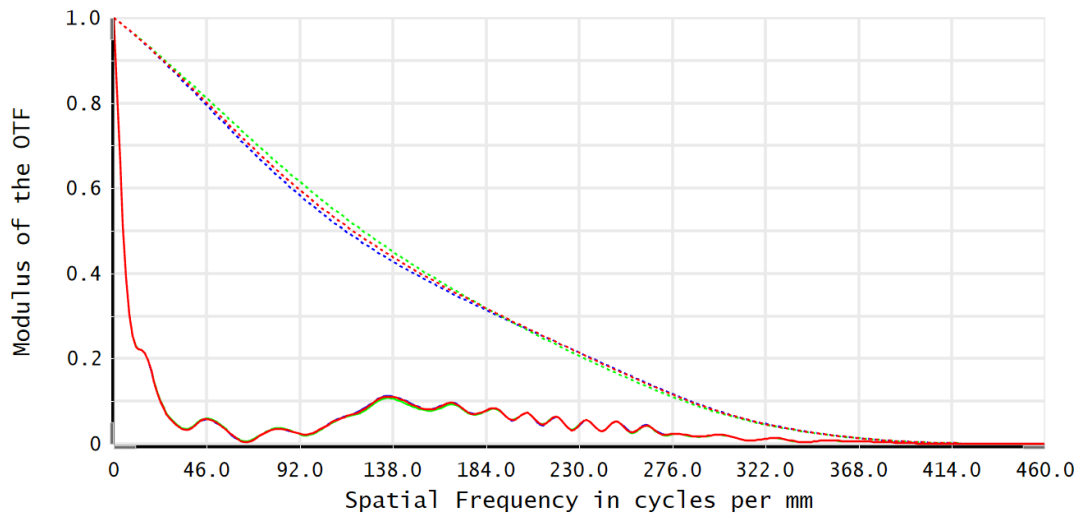
Diff. Limit-Tangential
 Diff. Limit-Sagittal
 0.0000, 0.0000 mm-Tangential
 0.0000, 0.0000 mm-Sagittal
 0.4000, 0.0000 mm-Tangential
 0.4000, 0.0000 mm-Sagittal
 0.2000, 0.0000 mm-Tangential
 0.2000, 0.0000 mm-Sagittal

Polychromatic Diffraction MTF	
49374 Achromatic Lens 5/11/2022 Data for 0.5500 to 0.7500 μm. Surface: Image	Zemax Zemax OpticStudio 18.1
Legend items refer to Field positions	fitted 2 lens.zmx Configuration 1 of 1

Lens data for 3rd design:

Surface Type	Comment	Radius	Thickness	Material	Co.	Clear Semi-Dia	Chip Zone	Mech Semi-Dia	Conic	TCE x 1E-6	Par 1(unused)	Par 2(unused)
0	OBJECT	Standard	Infinity	18.00000		0.40000	0.00000	0.40000	0.000...	0.00000		
1	Paraxial		13.00000	1.00,0.0 M		6.06074	-	-	0.00000	0.00000	18.00000	1
2	Standard	Infinity	5.00000			5.77185	0.00000	5.77185	0.000...	0.00000		
3	STOP	Standard	Infinity	0.00000		5.66074	0.00000	5.66074	0.000...	0.00000		
4	Standard	Infinity	20.00000			5.66074	0.00000	5.66074	0.000...	0.00000		
5	Coordinate Break		0.00000	-		0.00000	-	-	-	-	0.00000	0.00000
6	Standard	Infinity	0.00000	MIRR...		8.04591	0.00000	8.04591	0.000...	0.00000		
7	Coordinate Break		-30.00000	-		0.00000	-	-	-	-	0.00000	0.00000
8	Coordinate Break		0.00000	-		0.00000	-	-	-	-	0.00000	0.00000
9	Standard	Infinity	0.00000	MIRR...		8.19261	0.00000	8.19261	0.000...	0.00000		
10	Coordinate Break		77.66204	-		0.00000	-	-	-	-	0.00000	0.00000
11	(aper) Black Box Lens	TTL100-A FORW...	<29.21463>			13.00000 U	-	-	-	0.00000		
12	Standard	Infinity	64.07012 V			5.84618	0.00000	5.84618	0.000...	0.00000		
13	Standard	Infinity	64.07012 P			2.22971	0.00000	2.22971	0.000...	0.00000		
14	(aper) Black Box Lens	TTL100-A REVER...	<29.21463>			13.00000 U	-	-	-	0.00000		
15	Standard	Infinity	72.66204 V			8.51194	0.00000	8.51194	0.000...	0.00000		
16	(tilt/dec) Standard	Infinity	-15.00000	MIRR...		8.23443	0.00000	8.23443	0.000...	0.00000		
17	Coordinate Break	Element Tilt	-0.00000	-		0.00000	-	-	-	-	0.00000	0.00000
18	Standard	Infinity	-0.00000	N-BK7		6.56220	0.00000	6.56220	0.000...	-		
19	Coordinate Break	Element Tilt:return	-5.00000	-		0.00000	-	-	-	-	0.00000 P	0.00000 P
20	Coordinate Break	Element Tilt	-0.00000	-		0.00000	-	-	-	-	0.00000	0.00000
21	(aper) Standard	Infinity	-0.00000			10.00000 U	0.00000	10.00000	0.000...	0.00000		
22	Coordinate Break	Element Tilt:return	-35.00000	-		0.00000	-	-	-	-	0.00000 P	0.00000 P
23	Coordinate Break	Element Tilt	-0.00000	-		0.00000	-	-	-	-	0.00000	3.90994 V
24	Paraxial		-50.00308			5.80370	-	-	-	0.00000	50.00000	1
25	IMAGE	Standard	Infinity	-		1.64691	0.00000	1.64691	0.000...	0.00000		

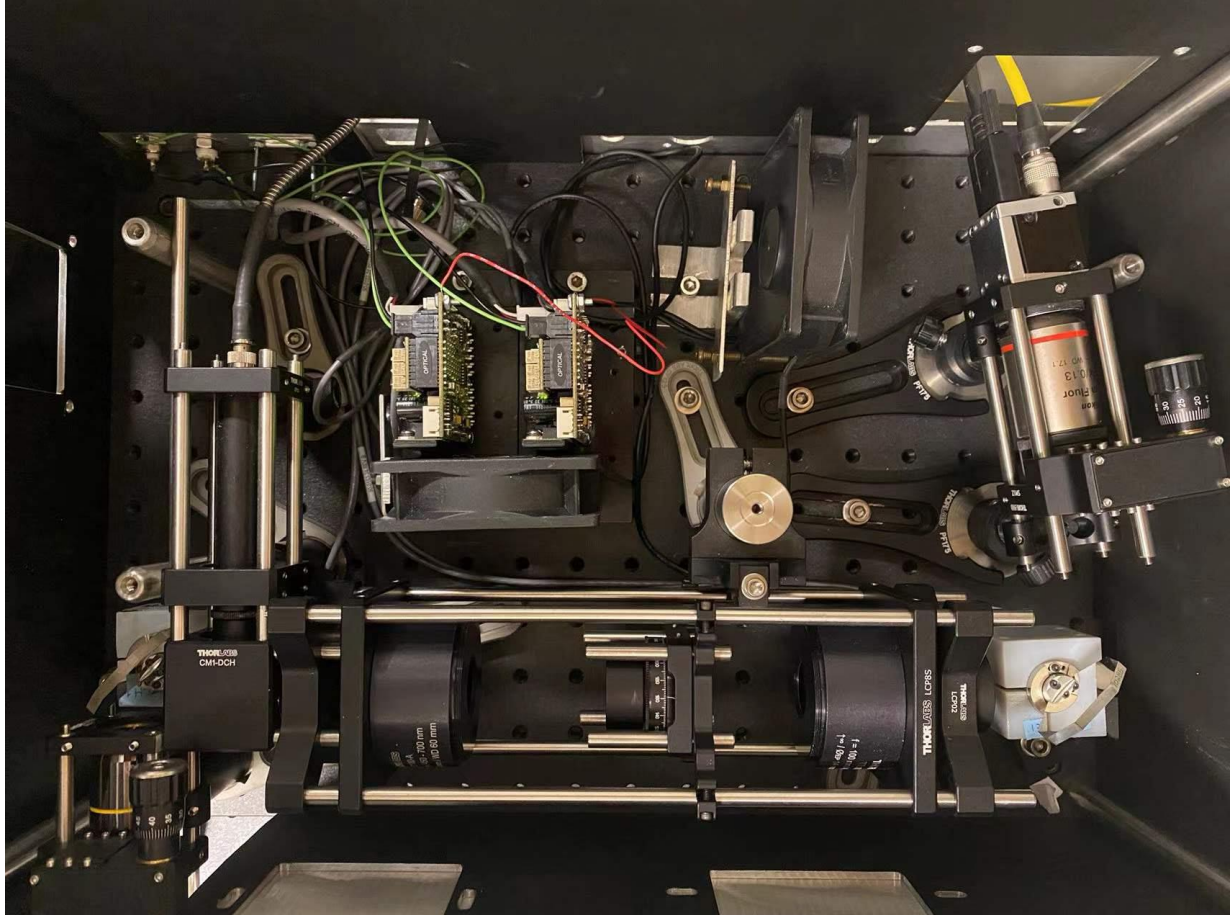
MTF:



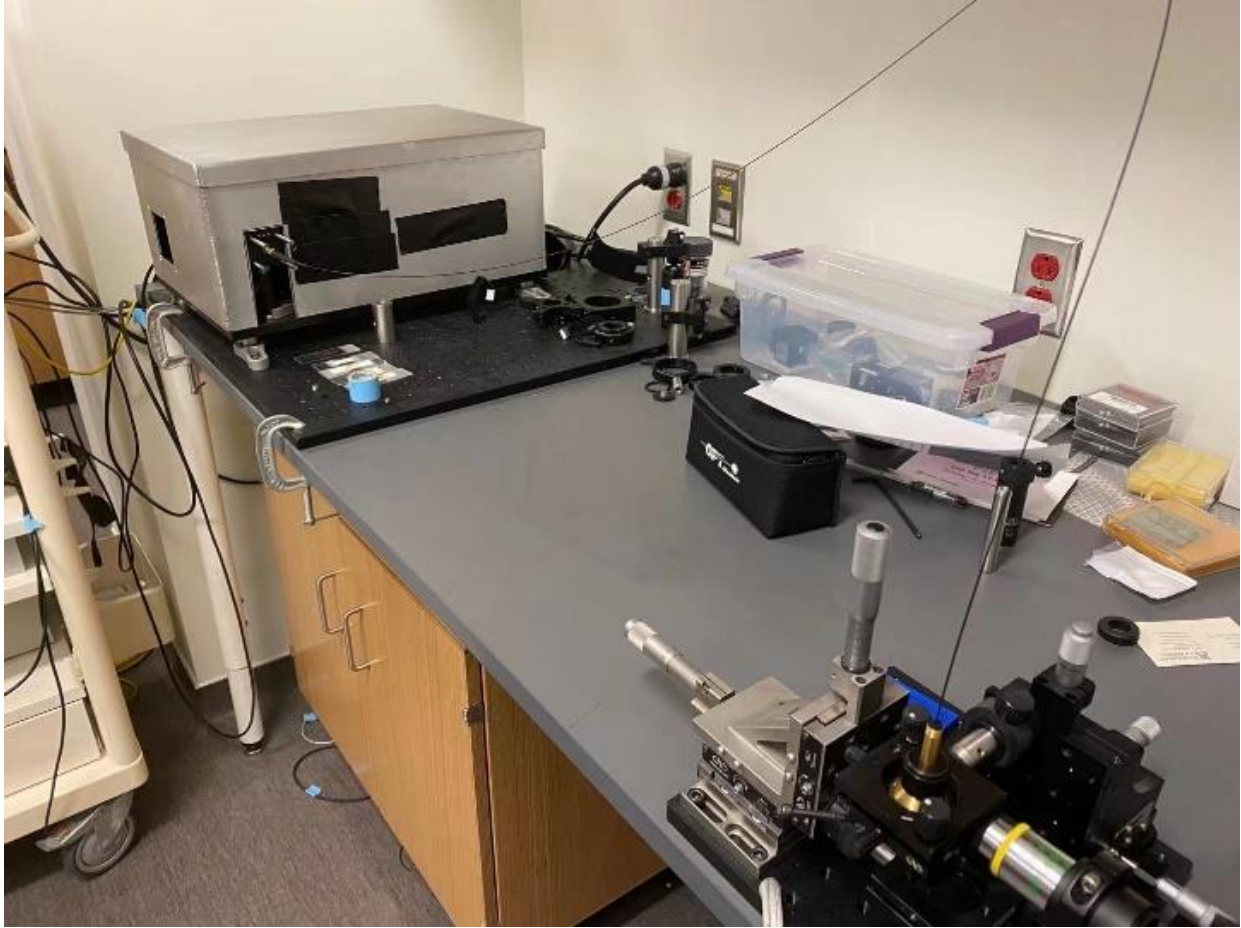
- 0.0000, 0.0000 mm-Tangential
- - - 0.0000, 0.0000 mm-Sagittal
- 0.4000, 0.0000 mm-Tangential
- - - 0.4000, 0.0000 mm-Sagittal
- 0.2000, 0.0000 mm-Tangential
- - - 0.2000, 0.0000 mm-Sagittal

Polychromatic Diffraction MTF	
49374 Achromatic Lens 5/11/2022 Data for 0.5000 to 0.7500 μm . Surface: Image Legend items refer to Field positions	Zemax Zemax OpticStudio 18.1 spectrometer with tube lens paraxial at end 2.zmx Configuration 1 of 1

Appendix B: System Setup



Photographs of real MSCE system (inside)



Photographs of real MSCE system (outside)

Reference

1. Siegel RL, Miller KD, Jemal A. Cancer statistics, 2019. *CA Cancer J Clin* 2019;69:7-34.
2. U.S. National Institute Of Health, National Cancer Institute. SEER Cancer Statistics Review, 1975–2015.
3. Centers For Disease Control And Prevention. National Center For Health Statistics. CDC WONDER On-Line Database, Compiled from Compressed Mortality File 1999-2016 Series 20 No. 2V, 2017.
4. Amin MB, Edge SB, Greene FL, Byrd DR, Brookland RK, Washington MK, Gershenwald JE, Compton CC, Hess KR, Sullivan DC, Jessup JM, Brierley JD, Gaspar LE, Shilsky RL, Balch CM, Winchester DP, Asare EA, Madera M, Gress DM, Meyer Vega LR. American Joint Committee on Cancer (AJCC) Cancer Staging Manual, 8th Edition. Chicago: Springer Nature, Springer International Publishing AG, 2018. Print.
5. National Lung Screening Trial Research Team, Aberle DR, Adams AM, Berg CD, Black WC, Clapp JD, Fagerstrom RM, Gareen IF, Gatsonis C, Marcus PM, Sicks JD. Reduced lung-cancer mortality with low-dose computed tomographic screening, *N Engl J Med*. 2011;Aug 4:365(5):395-409.
6. Reyes N, Onadeko OO, Luraschi-Monjagatta MD, Knox KS, Rennels MA, Walsh TK, Ampel NM. Positron Emission Tomography in the Evaluation of Pulmonary Nodules Among Patients Living in a Coccidioidal Endemic Region, *Lung*. 2014;192:589-593.
7. Zhang HF, Zeng XT, Xing F, Fan N, Liao MY. The diagnostic accuracy of CT-guided percutaneous core needle biopsy and fine needle aspiration in pulmonary lesions: a meta-analysis, *Clin Radiol*. 2016;Jan;71(1):e1-10.
8. J. B. Pawley, Ed., *Handbook of biological confocal microscopy*, 3rd ed. New York, NY: Springer, 2006.
9. B. Valeur and M. N. Berberan-Santos, “A Brief History of Fluorescence and Phosphorescence before the Emergence of Quantum Theory,” *J. Chem. Educ.*, vol. 88, no. 6, pp. 731–738, Jun. 2011, doi: 10.1021/ed100182h.
10. A. Jablonski, “Efficiency of Anti-Stokes Fluorescence in Dyes,” *Nature*, vol. 131, no. 3319, pp. 839–840, Jun. 1933, doi: 10.1038/131839b0.
11. L. Vincze, “Confocal X-ray Fluorescence Imaging and XRF Tomography for Three-Dimensional Trace Element Microanalysis,” *MAM*, vol. 11, no. S02, Aug. 2005, doi: 10.1017/S1431927605503167.
12. Ocak S, Duplaquet F, Jamart J, Pirard L, Weynand B, Delos M, Eucher P, Rondelet B, Dupont M, Delaunois L, Sibille Y, Dahlqvist C. Diagnostic Accuracy and Safety of CT-Guided Percutaneous Transthoracic Needle Biopsies: 14-Gauge versus 22-Gauge Needles, *J Vasc Interv Radiol*. 2016;May27(5):674-681.
13. Heerink WJ, de Bock GH, Groen HJ, Vliegenthart R, Oudkerk M. Complication rates of CT-guided transthoracic lung biopsy: meta-analysis, *Eur Radiol*. 2017;Jan;27(1):138-148.
14. Dalag L, Fergus JK, Zangan SM. Lung and Abdominal Biopsies in the Age of Precision Medicine, *Semin Intervent Radiol*. 2019;Aug;36(3):255-263.
15. Thiberville L, Moreno-Swiric S, Vercauteren T, Peltier E, Cave’ C, Bourg Heckly G. In Vivo Imaging of the Bronchial Wall Microstructure Using Fibered Confocal Fluorescence Microscopy, *Am J Respir Care Med*. 2007;175:22-31.

16. Thiberville L, Salaun M, Lachkar S, Dominique S, Moreno-Swirc S, Vever-Bizet C, Bourg Heckly G. Human in vivo fluorescence microimaging of the alveolar ducts and sacs during bronchoscopy, *Eu Respir J.* 2009;33:974-985.
17. Hassan T, Piton N, Lachkar S, Salaun M, Thiberville L. A Novel Method for In Vivo Imaging of Solitary Lung Nodules Using Navigational Bronchoscopy and Confocal Laser Microendoscopy, *Lung.* 2015;193:773-778.
18. Krstajic N, Akram AR, Choudhary TR, McDonald N, Tanner MG, Pedretti E, Dalgarno PA, Scholefield E, Girkin JM, Morre A, Bradley M, Dhaliwal K, Two-color widefield fluorescence microendoscopy enables multiplexed molecular imaging in the alveolar space of human lung tissue, *J Biomed Opt.* 2016;21(4):046009.
19. Mills B, Bradley M, Dhaliwal K. Optical imaging of bacterial infections. *Clin Transl Imaging.* 2016;4:163-174.
20. Su Z, Zhong C, Li S, Chen X, Chen Y, Tang C. Needle-based confocal laser endomicroscopy in the diagnosis of peripheral pulmonaru nodule: a preliminary report, *J Thorac Dis.* 2017;9(8):2608-2612.
21. Vanherp L, Poelmans J, Hillen A, Govaerts K, Belderbos S, Buelens T, Lagrou K, Himmelreich U, Vande Velde G. Bronchoscopic fibered confocal fluorescence microscopy for longitudinal in vivo assessment of pulmonary fungal infections in free breathing mice. *Scientific Reports.* 2018;8:3009.
22. Salaun M, Guisier F, Dominique S, Genevois A, Jounieaux V, Bergot E, Thill C, Piton N, Thiberville L. In vivo probe-based confocal laser endomicroscopy in chronic interstitial lung diseases: Specif descriptors and correlation with Chest CT. *Respirology.* 2019;24:783-791.
23. Wijmans L, Yared j, de Bruin DM, Meijer SL, Baas P, Bonta PI, Annema JT. Needle-based confocal laser endomicroscopy for real-time diagnosing and staging of lung cancer, *Eur Respir J.* 2019;53:1801520:1-9.
24. Kramer T, Wijmans L, de Bruin M, van Leeuwen T, Radonic T, Bonta P, Annema JT. Bronchoscopic needle-based confocal laser endomicroscopy (nCLE) as a real-time detection tool for peripheral lung cancer, *Thorax.* 2021 10.1136/thoraxjnl-2021-216885: 1-8.
25. Vanherp L, Poelmans J, Hillen A, Govaerts K, Belderbos S, Buelens T, Lagrou K, Himmelreich U, Vande Velde G. Bronchoscopic fibered confocal fluorescence microscopy for longitudinal in vivo assessment of pulmonary fungal infections in free breathing mice. *Scientific Reports.* 2018;8:3009.
26. Larson MC, Gmitro AF, Utzinger U, Rouse AR, Woodhead GJ, Carlson Q, Hennemeyer CT, Barton JK. Using FDA-approved drugs as off-label fluorescent dyes for optical biopsies: from in silico design to ex vivo proof-of-concept, *Methods Appl Fluoresc.* 2021 Jun4;9(3) doi: 10.1088/2050-6120/ac0619. PMID: 34044380.
27. Udovich JA, Besselsen DG, Gmitro AF. Assessment of acridine orange and SYTO 16 for in vivo imaging of the peritoneal tissues in mice. *J Microsc.* 2009;234(2):124-129.
28. Risi MD, Rouse AR, Chambers SK, Hatch KD, Zheng W, Gmitro AF, "Pilot Clinical Evaluation of a Confocal Microlaparoscope for Ovarian Cancer Detection" *Inter J Gynecol Cancer* 2016;26(2) 248-254.
29. Wishart DS, Feunang YD, Guo AC, Lo EJ, Marcu A, Grant JR, Sajed T, Johnson D, Li C, Sayeeda Z, Assempour N, Iynkkaran I, Liu Y, Maciejewski A, Gale N, Wilson A, Chin L, Cummings R, Le D, Pon A, Knox C, Wilson M. DrugBank 5.0: a major update to the DrugBank database for 2018. *Nucleic Acids Res.* 2017 Nov 8. doi: 10.1093/nar/gkx1037.

30. Ursu O, Holmes J, Knockel J, Bologna CG, Yang JJ, Mathias SL, Nelson SJ, Oprea TI, DrugCentral: online drug compendium, *Nucleic Acids Research*, Volume 45, Issue D1, January 2017, Pages D932–D939, <https://doi.org/10.1093/nar/gkw993>
31. Gmitro, A., Aziz, D, Confocal Microscopy Through a Fiber-Optic Imaging Bundle, *Opt. Lett.* 1993;18: 565-567.
32. Sabharwal YS, Rouse AR, Donaldson L, Hopkins MF, Gmitro AF. Slit-scanning confocal microendoscope for high-resolution in vivo imaging. *Appl Opt.* 1999;38(34):7133-7144.
33. Rouse AR, Gmitro AF. Multispectral imaging with a confocal microendoscope. *Opt Lett.* 2000;25(23):1708-1710.
34. Rouse AR, Kano A, Udovich JA, Kroto SM, Gmitro AF. Design and demonstration of a miniature catheter for a confocal microendoscope. *Appl Opt.* 2004;43(31):5763-5771.
35. Makhlof H, Gmitro AF, Tanbakuchi AA, Udovich JA, Rouse AR. Multispectral confocal microendoscope for in vivo and in situ imaging. *J Biomed Opt.* 2008;13(4):44016.
36. Tanbakuchi AA, Rouse AR, Udovich JA, Hatch KD, Gmitro AF. Clinical confocal microlaparoscope for real-time in vivo optical biopsies. *J Biomed Opt.* 2009;14(4):44030. doi:10.1117/1.3207139
37. Tanbakuchi AA, Udovich JA, Rouse AR, Hatch KD, Gmitro AF. In vivo imaging of ovarian tissue using a novel confocal microlaparoscope. *Am J Obstet Gynecol.* 2010;202(1). doi:ARTN 90.e1DOI 10.1016/j.ajog.2009.07.027
38. Zimmermann T, Rietdorf J, Pepperkok R. Spectral imaging and its applications in live cell microscopy. *FEBS Letters.* 2003;546:87-92.
39. Phung M, Rouse AR, Pangilinan J, Bell RC, Bracamonte ER, Mashi S, Gmitro AF, Lee BR. Investigation of confocal microscopy for differentiation of renal cell carcinoma versus benign tissue. Can an optical biopsy be performed? *Asian J Urology*, <https://doi.org/10.1016/j.ajur.2019.12.008>.
40. "Syringe Needle Gauge Chart". Sigma Aldrich. Retrieved 20 March 2012.
41. "Hypodermic Needle Gauge Chart". Medical Tube Technology, Inc. Retrieved 20 March 2012.
42. "ISO 6009:2016 Hypodermic needles for single use -- Colour coding for identification". International Organization for Standardization. Publication date: 2016-08
43. https://en.wikipedia.org/wiki/Birmingham_gauge#cite_note-7
44. Joshua Anthony Udovich, Nathaniel D. Kirkpatrick, Angelique Kano, Anthony Tanbakuchi, Urs Utzinger, and Arthur F. Gmitro, "Spectral background and transmission characteristics of fiber optic imaging bundles," *Appl. Opt.* 47, 4560-4568 (2008).
45. https://en.wikipedia.org/wiki/CIE_1931_color_space
46. Neil C. Momsen, Andrew R. Rouse, and Arthur F. Gmitro, "Improvement in optical fiber bundle-based imaging using synchronized fiber motion," *Appl. Opt.* 59, G249-G254 (2020)
47. Noah Bedard, Tomasz S. Tkaczyk, "Snapshot spectrally encoded fluorescence imaging through a fiber bundle," *J. Biomed. Opt.* 17(8) 080508 (17 August 2012) <https://doi.org/10.1117/1.JBO.17.8.080508>
48. Sikka P, Bindra VK, Kapoor S, Jain V, Saxena KK. Blue cures blue but be cautious. *J Pharm Bioallied Sci.* 2011;3(4):543-545. doi:10.4103/0975-7406.90112
49. Rasooly R. Expanding the bactericidal action of the food color additive phloxine B to gram-negative bacteria. *FEMS Immunol Med Microbiol.* 2005 Aug 1;45(2):239-44. doi: 10.1016/j.femsim.2005.04.004. PMID: 15949926.

50. Faulds, D., Balfour, J.A., Chrisp, P. et al. Mitoxantrone. *Drugs* 41, 400–449 (1991).
<https://doi.org/10.2165/00003495-199141030-00007>
51. Carlos Renteria, Javier Suárez, Alyssa Licudine, and Stephen A. Boppart, "Depixelation and enhancement of fiber bundle images by bundle rotation," *Appl. Opt.* 59, 536-544 (2020)
52. Dusch E, Dorval T, Vincent N, Wachsmuth M, Genovesio A. Three-dimensional point spread function model for line-scanning confocal microscope with high-aperture objective. *J Microsc.* 2007 Nov;228(Pt 2):132-8. doi: 10.1111/j.1365-2818.2007.01844.x. PMID: 17970913.